EXPERIMENTAL AND COMPUTATIONAL EVALUATION OF GEOMATERIAL INTERACTIONS IN FLEXIBLE PAVEMENTS

A Dissertation
Presented to
The Academic Faculty

by

Sangameshwar S. Hanumasagar

In Partial Fulfillment
of the Requirements for the Degree
Doctor of Philosophy in the
School of Civil and Environmental Engineering

Georgia Institute of Technology
December 2019

EXPERIMENTAL AND COMPUTATIONAL EVALUATION OF GEOMATERIAL INTERACTIONS IN FLEXIBLE PAVEMENTS

Approved by:

Dr. J. David Frost, Advisor
School of Civil and Environmental Engineering
Georgia Institute of Technology

Dr. Mark H. Wayne
Director of Application Technology
Tensar International Corporation

Dr. Susan E. Burns
School of Civil and Environmental Engineering
Georgia Institute of Technology

Dr. S. Sonny Kim
College of Engineering
University of Georgia

Dr. Arun M. Gokhale
School of Materials Science and Engineering
Georgia Institute of Technology

Date Approved: October 10, 2019

ACKNOWLEDGEMENTS

This research was possible due to the support and contributions, directly or indirectly, from many individuals. I share the pride of completing my PhD with all these individuals. First, I would like to thank my adviser, Dr. David Frost, for giving me the opportunity to join his group and be a part of the rich collaborative and enjoyable environment here at Georgia Tech. The diversity in research topics, skills and ideas from peers and mentors as well as the intellectual freedom to explore different academic interests were crucial in shaping my journey as a PhD student. I deeply appreciate the uninhibited access to courses from various departments that allowed me to take classes in various disciplines including geosystems, material science, city planning and computational science.

My friends in the Geosystems group helped me in many ways, be it technical discussions, planning our careers or just random chats to provide a healthy distraction from research. I want to especially thank Dr. Prashanth Vangla and Rodrigo Borela who I worked with during different stages of my PhD. Prashanth's ideas and feedback during the initial testing phase of the newly designed experimental setup, and Rod's expertise in computational modelling and moreover, his willingness to share his ideas and knowledge was crucial in conducting this research study.

Last but not the least; I want to thank my family for always encouraging me to pursue my goals and being a phone call away at all times. I am privileged to have this kind of support, and will strive to use it as a force for positive change in the world.

TABLE OF CONTENTS

LIST OF TABLES

LIST OF FIGURES

SUMMARY

Improving the design and performance of pavement systems has been a topic of extensive research in the past few decades, with the two-fold objective of reducing construction and maintenance costs of roads while extending their duration of serviceability. While geosynthetics have been identified as viable means to stabilize and/or reinforce pavements at lower life-cycle costs and achieve improved performance of the resulting systems, their widespread adoption has been slow owing to several challenges. Some of these challenges arise from a lack of technical understanding about complex mechanisms such as interaction between aggregates and geosynthetics, while some others arise from inherent difficulties associated with pavement testing such as experimental design, specimen size and testing costs.

This research study aimed to address these specific challenges by developing a new bench-scale pavement simulation system that expedites testing by employing downscaled specimens while still preserving mechanisms associated with full-scale operational pavements. Upon validation of functionality and calibrations, the system was then used to conduct a series of rutting tests using different combinations of subgrade stiffness's, geosynthetic inclusions and aggregate mixes under rolling-wheel loads (which represents traffic loads over a pavement). By analyzing the resulting time-series data of surface displacements and subgrade stresses through the course of repeated stress-applications over the specimen, the influence of the subgrade stiffness and geosynthetic benefits over the macro-level pavement performance was clearly quantified. These results reiterate the ability of geosynthetics to mitigate excessive rutting by reducing lateral spreading of

aggregates in the base layer and thereby, reducing stresses transmitted into the subgrade. This effect was especially evident in soft subgrade conditions. Further, a back-calculation procedure for the estimation of the approximate composite modulus of the stabilized pavement was conducted. This could enhance current Mechanistic-Empirical design workflows for geosynthetic-stabilized pavements, where the quantification of geosynthetic role has historically been challenging.

Further, in an attempt to better understand the interlocking mechanisms associated with aggregate-geogrid interaction, which is crucial for ensuring the efficiency of geogrids in the base-course layer of the pavement, a study which focused on this aspect is presented. Two mono-sized aggregate materials of significantly different morphologies were used in conjunction with steel grids and polymer geogrids of four different opening sizes. Rutting tests were conducted for all combinations of aggregates, grids and grid locations, keeping the layer density and loading stress the same. These series of tests yielded valuable insights relating to optimal design parameters to maximize the reduction in surface rutting. This database of experiments on mono-sized spheres and biaxial geogrids was supplemented with results from a suite of Discrete Element Modelling (DEM) simulations to visualize interaction mechanisms at a particle-level, which is possible using such computational techniques.

In summary, this study helps gain a deep understanding of geosynthetic benefits over soft subgrades and geogrid interlocking mechanisms with different types of aggregates in various design configurations. Ultimately, this dissertation presents a compelling case for using geosynthetics in pavements and presents some ideas for enhancing current design guidelines in this respect.

CHAPTER 1. INTRODUCTION

The behavior and modelling of pavement systems has been a subject of interest and relevance to several federal and state governmental agencies as well as research institutions for many decades. Apart from the high economic value to be gained from optimization of pavement designs, pavement systems are also of high interest to researchers owing to the unique combination of technical challenges they pose. Some of the geotechnical challenges include the complex behavior of the multiple geomaterials involved including the heterogeneity and discrete nature of the particles, which makes their interaction difficult to predict, as well as the non-linearity in their properties and performance over time. Therefore, to properly model and design a pavement system, a strong understanding of the fundamental particle-level interactions under different stress conditions, supplemented with knowledge of macro-system performance collected from extensive experimentation is needed. This research study addresses a few of the long-standing questions involving behavior of geosynthetic stabilized flexible pavement and the factors influencing their performance using a combination of novel laboratory and computational techniques.

1.1 Motivation for Research

Geosynthetics offer an economic alternative for pavement stabilization by enhancing the engineering properties of the aggregate base layer. The majority of this study is focused on characterizing the performance of geogrids under various design considerations. It is widely accepted that geogrids help enhance the performance of aggregate systems by lateral confinement of the aggregate particles via mechanical interlocking within the geogrid openings. This results in an increased composite stiffness

of the stabilized base layer (Giroud, 1985, Barksdale, 1989, Webster, 1993, Zornberg, 2011). However, the benefits achieved are heavily dependent on the extent of interlocking between the aggregate particles and geogrid, which in turn is affected by a wide range of aggregate and geogrid related parameters. Some of the most important considerations, that forms the crux of this study, are briefly discussed below.

1.1.1 Factors influencing geogrid-aggregate interaction

Among the multitude of factors that influence aggregate-geogrid interaction, some of the most commonly debated factors include the engineering properties of the aggregate and geogrid materials, location of the geogrid in the base layer and the optimal aperture size of the geogrid relative to the particle sizes in the aggregate material. Most aggregates used in construction are standard high quality material, which makes them expensive. In recent times, there is increasing interest in adopting recycled aggregates and construction debris in pavements, which might not exhibit the same superior morphological or strength characteristics as the virgin material. This introduces the need for performance testing using poor quality aggregate materials. Geogrids are extensible polymers, which are manufactured across a range of geometries, stiffness's and strength properties. As one would expect, different combinations of aggregates and geogrids result in different behavior. Moreover, there are additional design considerations like stiffness of the underlying subgrade soil, choice of geogrid product, location of geogrid in the base layer and number of such geogrid layers. Ultimately, all these factors together determine the performance lifecycle of a pavement system.

To study the effect of each of these parameters individually and in combination, an accurate and efficient testing methodology is required to test composite pavement systems.

1.1.2 Laboratory rutting testing procedure

Rutting tests are conducted to measure the permanent deformations at the surface of a pavement induced by repeated wheel loads. They are typically conducted on full-scale sections to get a realistic assessment of the pavement performance under operating conditions. These tests are time and cost intensive and difficult to execute. On the other hand, laboratory tests have largely focused on measurement of resilient modulus using cyclic triaxial tests or repeated-load plate tests, which is an important parameter in pavement design software. While laboratory experiments are extremely useful for this purpose, the measurement of permanent deformation has been lower priority in most studies, owing to the difficulty in testing multi-layered systems. Additionally, most laboratory experiments use an idealized vertical loading system, which may not exactly replicate mechanisms like lateral spreading under directional wheel motion, which is the case in the field. The laboratory measurement of permanent deformation properties of aggregates has been proven very beneficial owing to its good correlation with aggregate rutting potential in the field (Thompson, 1998, Tao, 2010, Xiao, 2012, Mishra, 2012, Kwon, 2014, 2017). However, there is a need for a standardized laboratory procedure to measure permanent deformations of geogrid-stabilized composite pavement specimens, while also closely simulating field conditions like rotating-wheel loading.

Thus, in order to reliably study the inter-dependence of interplaying factors like grid opening, grid location and particle morphology, a systematic parametric study was

conducted using a laboratory bench-scale rutting procedure. The procedure presents the following key features, (i) easier to prepare consistent homogeneous specimens, which ensure repeatable results, (ii) rapid testing rate, and (iii) low material usage. In addition, the apparatus closely replicates field mechanisms like lateral spreading induced by cyclic wheel-loading.

In summary, there have been several research studies in the past that have done elaborate full-scale pavement and laboratory tests and numerical modelling of pavement systems, which have all added to the rich body of knowledge in the pavement literature. However, constantly evolving testing methods and technological tools presents an opportunity to revisit aspects that can be explained better with a fresh perspective. For example, most of the studies in the past have focused on rutting behavior at the specimen scale, with the goal of quantifying the benefit of the geogrid. This results in the conclusions drawn from the study being limited to the material and methods used in that particular study, limiting generalizations of the findings. In this study, we aim to approach the problem of understanding and modelling the behavior of pavement systems from the perspective of particles involved, which together define the global performance of the system. In summary, this study encompasses both laboratory and computational methods, to visualize the mechanisms at play inside the material in addition to the performance of the composite aggregate-geogrid systems.

1.2 Scope of Thesis

This thesis is organized as follows.

- Chapter II presents a detailed literature review of the relevant work performed previously in the field of geosynthetic-stabilized pavement systems. The technical concepts that have been established, relating to mechanisms of aggregate-geosynthetic interaction, pavement design criteria are summarized. Lastly, a brief description of the discrete element method and the previous body of knowledge pertaining to application of DEM to simulate aggregate behavior is presented.
- Chapter III presents the design, development and operational methodology of the bench scale rutting system developed for experimental testing. This chapter also serves as documentation of the various components of the test equipment and post-processing workflow of raw data to generate rutting and stress curves. A sample rutting test result is shown to give the reader a clear idea of the functionality of the system. Additionally, alternate capabilities of the system like simulation of compaction and slushing processes are described.
- Chapter IV presents an experimental study to assess the effects of subgrade stiffness and geosynthetic stabilization on surface rutting and stress distribution into the subgrade. Three soft subgrade soils from Georgia were selected along with graded aggregate base material and five different geosynthetic products. Several material characterization and rutting tests were conducted to quantify the performance of various combinations of stabilization and subgrade stiffness scenarios.

- Chapter V presents an experimental study to assess the effect of particle shape, grid opening size, location and stiffness on surface rutting. This testing sequence enables a detailed parametric assessment of the above factors, and inform formulation and validation of hypothesis regarding the interaction zone surrounding the grid.
- Chapter VI presents the DEM study to build on the current understanding and add a particle-scale perspective to assess various influencing parameters on aggregate-geogrid interactions. Particular focus is the evolution of lateral spreading of aggregates with and without geogrids, which is more relevant parameter to judge the quality and benefits of aggregate-grid interlocking.
- Lastly, Chapter VII presents the conclusions and recommendations for future work.

CHAPTER 2. LITERATURE REVIEW

Recent decades have witnessed an increasing demand for resilience and performance from road transportation systems, to sustain the increasing economic growth and rapidly evolving global market. This has inadvertently accelerated the distress and deterioration experienced by pavements, subsequently increasing maintenance costs for federal and state transportation agencies. However, the general materials and design methodologies used in the construction of new road infrastructure has not undergone a commensurate rate of improvement as the volume of heavy traffic that rely on them. An example along the lines of the topic of this study is the use geosynthetics in pavements, which in spite of having been around for several decades has not seen widespread adoption. Although several studies have established the benefits of geosynthetics, uncertainties regarding exactly quantifiable performance ratings, applicability across geologic settings and choice of optimal design variables still exist, which have slowed their adoption rate. This chapter summarizes the past studies and applications of geosynthetics, especially geogrids in flexible pavements, and attempts to highlight technical challenges that are yet to be solved to accelerate their adoption.

Using geosynthetic for stabilization of pavements has been widely studied since the 1970's. Their advantages include economical costs, simplicity in construction and quick installation time relative to alternative solutions like soil removal or lime stabilization. The two most commonly used geosynthetics in pavements are geotextiles and geogrids owing to their high stabilizing potential and easy installation. Therefore, the primary focus of this study is the stabilization effects of geotextiles and geogrids in flexible pavement systems.

Before discussing the engineering mechanisms inside the pavement system, a short summary of pavement layered system and common distress modes is presented below.

A cross-section of a typical flexible pavement system is shown in Figure 2-1. It depicts four distinct layers: asphalt, aggregate base course, aggregate subbase (optional) and subgrade layers. The design is such that the stiffness of the layers decreases from top of the pavement to towards the bottom, so that the applied traffic load is effectively redistributed to minimize stress on the underlying weaker layers. The thicknesses of the asphalt and base course layers are based on a design framework, which can either be empirical (calibrated to similar pavements) or a combination of empirical and mechanistic analyses. Typically these thicknesses range between 0.1 m to 0.15 m (4 to 6 inches) of asphalt underlain by 0.2 m to 0.3 m (8 to 12 inches) of unbound coarse aggregate. The optional subbase layer, which generally involves lower quality crushed aggregate, can be placed under the base course for additional subgrade protection or drainage functions.

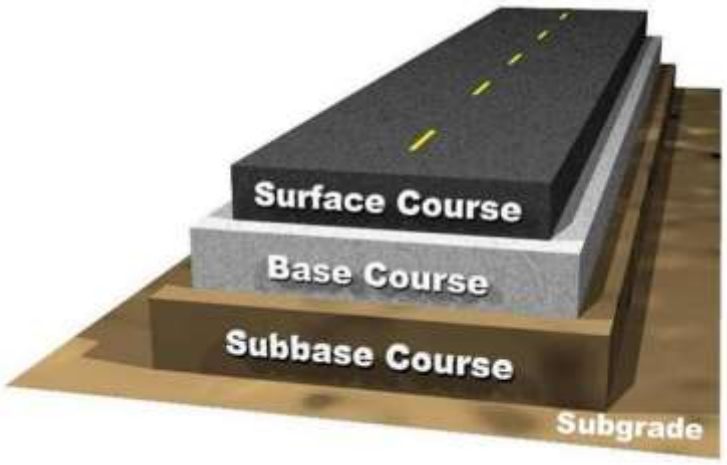

Figure 2-1 - Cross-section of flexible pavement system (Muench, 2006)

2.1 Distress in Pavements

Broadly, pavement failure can be categorized into two modes, structural or functional failure. A structural failure refers to a complete collapse of the pavements structure, requiring complete rebuilding before any further use. On the other hand, a functional failure refers to a condition where the pavement is not completely unusable but significantly damaged and uncomfortable for driving. This can be handled by remediation. Typically, unless the pavement fails under the effects of a natural calamity, the concerned authorities repair pavements when they reach a state of functional failure. There are several indicators of functional failure; and are categorized into distress modes as summarized below.

Some of the most common distress modes in pavements are rutting, load cracking, block/transverse cracking, reflection cracking, raveling, edge distress and patches/potholes. These are caused by a combination of repeated channelized traffic loading, environmental factors like temperature variations or subgrade moisture fluctuations and human-induced factors. Cracking is observed in the asphalt layer, and can be considered a top-down phenomenon, while rutting, which forms the focus of this study, is typically initiated from the underlying weak layers making it a bottom-up phenomenon. Some human induced factors include usage of sub-standard aggregate in construction or lack of preventative maintenance during the operation of the pavement, like sealing cracks and potholes.

Rutting is defined as the progressive accumulation of vertical permanent deformation of the surface of the pavement, under the repeated tire passes from channelized

heavy traffic loading over the pavement. The cumulative surface deformation occurs as a result of vertical deformations across all the layers of the pavement. It is extremely common in both paved and unpaved roads, under regular as well as heavy traffic. Typically, a rut depth of 50 mm to75 mm (2 inches to 3 inches) is deemed to require reparative maintenance, owing to the unpleasant driving experience as well as safety risk arising from surface water accumulation and potential hydroplaning. Figure 2-2 shows an example of significant rutting distress in a pavement.

Figure 2-2 - Rutting distress in a pavement

As mentioned the primary design objective for the layered pavement system is to allow redistribution of applied stresses over a larger area, decreasing the stresses transmitted to relatively weaker subgrade. This is depicted in Figure 2-3, which shows the high intensity of stress at the surface under the wheel, and the reduced intensity of stress over the subgrade. The thicknesses and engineering properties of the surface and base layers is specifically targeted towards these two critical regions. Firstly, the horizontal tensile strain at the bottom of the asphalt layer should be minimized to avoid surface fatigue cracking and rutting. Secondly, the stress transmitted to the subgrade layer must be

reduced, especially in regions with soft soils, to avoid excessive rutting. An insufficient design in these aspects can lead to rutting distress as shown in Figure 2-2. This study largely focuses on the effectiveness of geosynthetic reinforcement in the latter case.

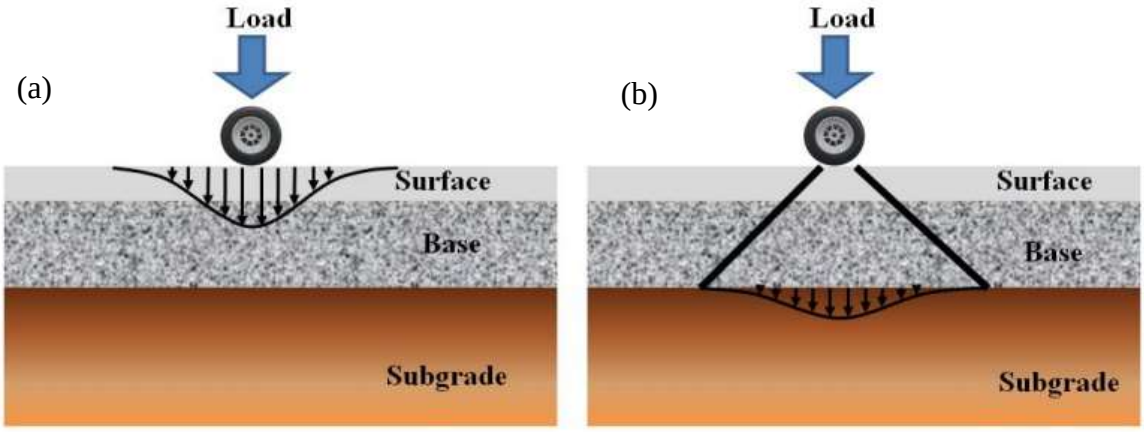

Figure 2-3 - Schematic showing stress distribution at (a) surface and (b) subgrade layer in a flexible pavement (Zornberg, 2010)

2.1.1 Rutting Modes

The accumulation of rutting displacements can be categorized into three mechanisms (Dawson, 1997) as follows. Compaction (Mode 0) involves densification of the aggregate layer, which can be largely avoided in well-compacted pavements. Local shear distortion (Mode 1) within the aggregate is the second category and refers to aggregate displacements and rotation under induced shear stresses from the traffic. This is typical with inadequate shear strength (Brown and Chan, 1996), under channelized trafficking and characterized by a dilative heave near the wheel path. The third category refers to distortion of the macro-pavement structure (Mode 2), including a wider displacement trough of the aggregate layer. Mode 2 rutting is especially common with good

quality aggregates, under channelized trafficking or over soft subgrades. Generally, it is also possible to witness a combination of these three modes of rutting. The three modes are shown schematically in Figure 2-4.

As stated above, rutting can arise from a combination of mechanisms and from aggregate as well as subgrade layers. This is contrary to previous understanding that rutting is limited to vertical displacement in soft subgrades (Giroud and Noiray, 1981). Previous studies have indicated that up to 70 percent of rutting occurring in flexible pavement systems can be attributed to the unbound layers (Little et al, 1994, Pidwerbeski, 1996).

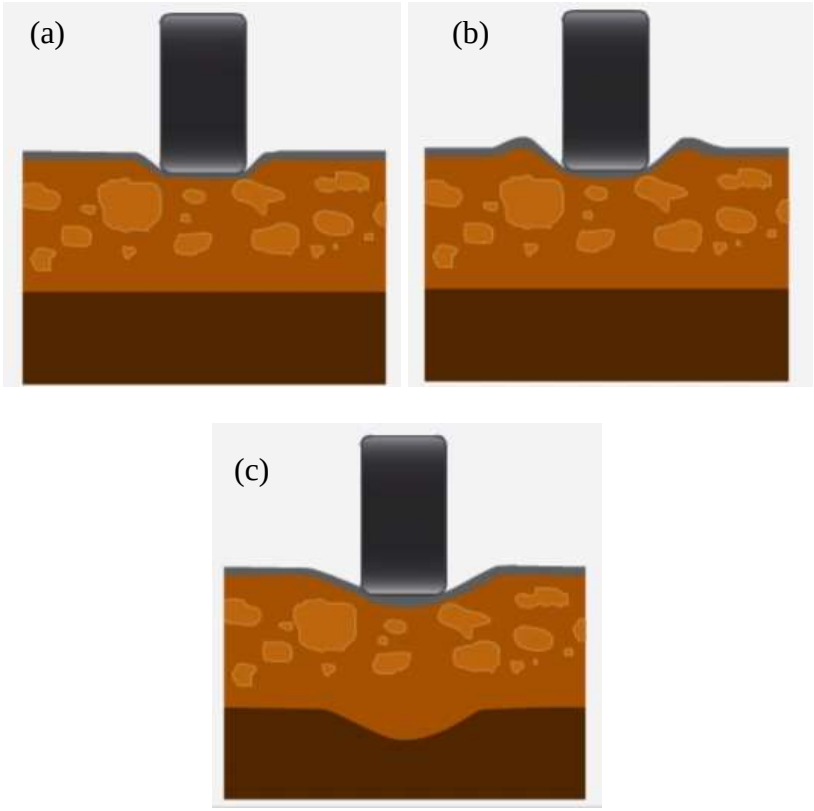

Figure 2-4 - Schematics showing (a) Mode 0, (b) Mode 1 and (c) Mode 2 rutting (Roadex.org)

The ability to predict rutting over the design life of the pavement under expected traffic loads is an important component of pavement design. Typically, the rutting behaviour of a material or pavement system is modelled in relation to the number of loading cycles. Unless under extreme conditions like very soft subgrade, the rutting deformations tend to plateau after several applications of loading, and thus referred to as a self-stabilizing system. The rutting displacement or permanent axial strain has been observed to follow a power law with respect of the number of loading repetitions (N). Two of the more common models are the Tseng and Lytton (1989) and the Monismith (1993) models.

The Tseng and Lytton (1989) is the basis for the permanent deformation model for granular material in the Mechanistic-Empirical Pavement Design Guidelines (MEPDG), which is described later. The mathematical form of the model is presented in Equation 1.

$$\frac{\varepsilon_{1,p}}{\varepsilon_{1,r}} = \left(\frac{\varepsilon_0}{\varepsilon_r}\right) e^{-\left(\frac{\rho}{N}\right)^{\beta}} \quad (1)$$

where, $(\varepsilon_0/\varepsilon_r)$, ρ and β are material parameters, to be determined by fitting values into a test curve, while $\varepsilon_{1,p}$ and $\varepsilon_{1,r}$ are the axial permanent and axial resilient strains respectively.

Monismith (1993) conducted cyclic undrained triaxial tests on silty-clay soils to estimate the subgrade contribution to surface rutting. The Monismith (1993) model estimates the permanent strain as follows.

$$\varepsilon_{1,\mathrm{p}} = AN^b \quad (2)$$

where A and B are coefficients to be determined experimentally for the given material.

2.2 Brief History of Pavement Design Methodologies in the US

The evolution of road design methods in the US since the 1930s is shown in Figure 2-5. The trend shows a gradual shift from heavy emphasis of engineering judgement-based design to an increasing incorporation of mechanistic performance.

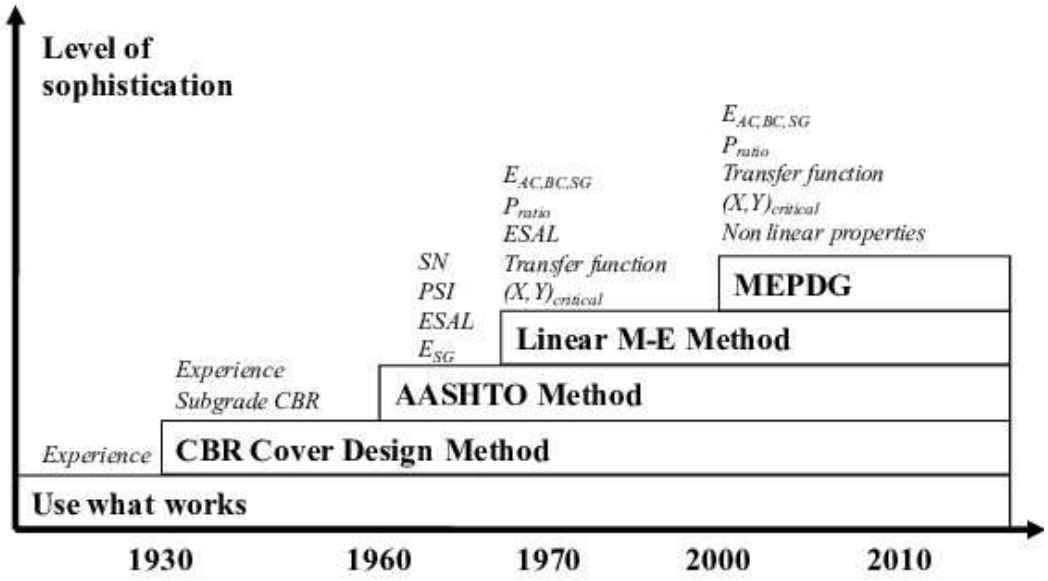

Figure 2-5 - Evolution of pavement design methods (Reck 2009)

2.2.1 AASHTO Method

The American Association of State Highway Officials (AASHTO) Road test in the 1960's was hugely significant in formulating a series of AASHTO design methods. The Road Test comprised of six test loops constructed in Ottawa, Illinois that were subjected to repeated cycles of standard truck loads over an accelerated design-life of 2 years, and

the behavior of the test pavements were monitored. This method considers the pavement as a multi-layered elastic system and the entire pavement system is characterized by structural number parameter (SN). The SN is calculated based on the anticipated traffic loads over the design life of the pavement, referred to as the Equivalent Single-Axle Loads (ESALs) and the design variables like layer thicknesses and moduli.

A set of design equations were developed that were to be used for the design of pavements in the US. However, these equations were specific to the materials and location used for the road tests, parameters were assumed to linearly extrapolate beyond the 2-year testing period and an abstract structural number scale was used to characterize the full pavement system.

2.2.2 NCHRP Mechanistic-Empirical Method

In the 1970s, researchers from South Africa proposed the linear mechanistic-empirical (M-E) deign method. This method attempted to combine aspects of empirical and performance-based mechanistic methods. Since the 1990s, attempts have been made in the US to shift to a similar M-E approach. In 2004, the National Cooperative Highway Research Program (NCHRP) published the Mechanistic-empirical pavement design guidelines (MEPDG). The MEPDG proposes using existing mechanistic-based models and databases and also account for site-specific inputs of traffic, climate, subgrade and existing pavement conditions. The procedure involves iterative calculations using user-generated input values for pavement design parameters and site conditions, and modifying the parameters until convergence. A flowchart for the various components in the ME method is presented in Figure 2-6. While a few state departments of transportation (DOT) have

transitioned to the MEPDG system, it is a complex procedure requiring several user inputs, which have to be determined regionally. Georgia DOT (GDOT) is in the process of this transition, as the current Georgia design manual is based on the 1972 AASHTO Guide.

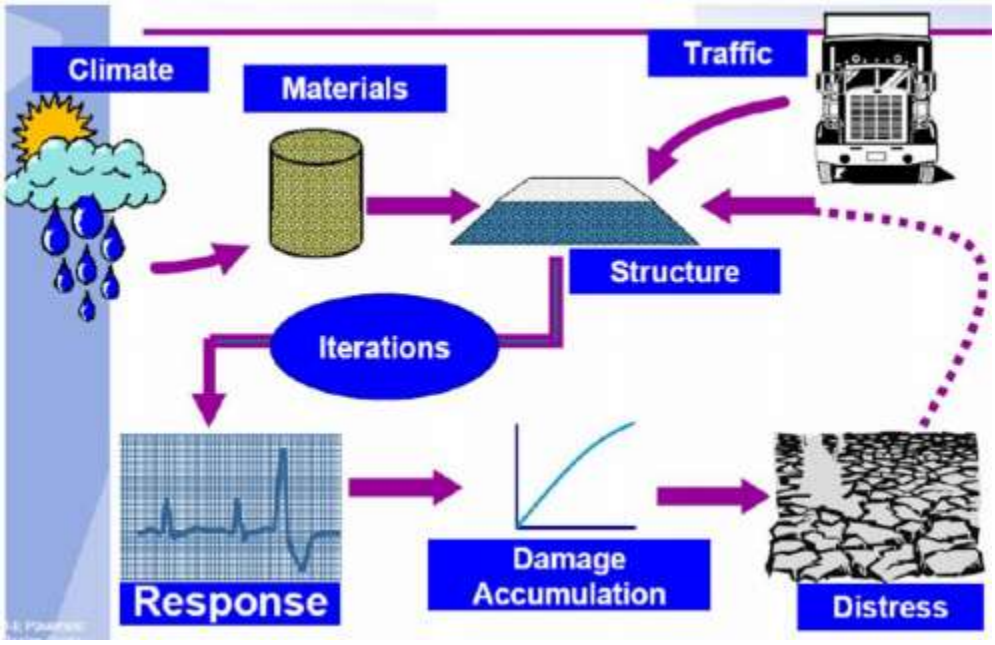

Figure 2-6 - Flowchart for M-E Design (NCHRP, 2004)

The primary mechanistic parameters in the M-E method are the Poisson's ratio (υ) and the resilient modulus (M_R) for each layer and the layer thicknesses. The Poisson's ratio (ratio of lateral to axial strains exhibited in response to axial loading) typically ranges from 0.15 to 0.5 for pavement materials. The M_R is defined as shown in Equation 3, and is a measure of the material stiffness under cyclic loading.

$$M_R = \frac{\sigma_d}{\varepsilon_r} \tag{3}$$

where, σ_d is the cyclic deviator stress and ε_r is the elastic recoverable strain in the material. The difference between the resilient modulus and Young's modulus is depicted in Figure 2-7 below.

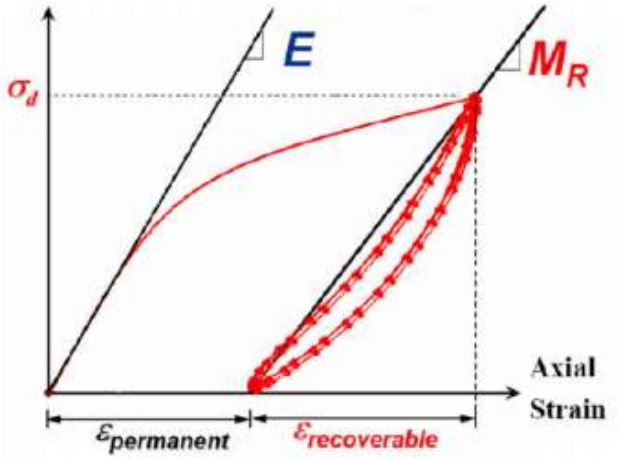

Figure 2-7 - Comparison of Resilient Modulus, M_R, and Modulus of Elasticity, E

Upon obtaining the afore-mentioned mechanistic parameters, the potential stresses and displacements in a pavement can be estimated using empirical models obtained from field observations. These empirical models are based on data obtained from extensive field monitoring of pavements across the country under the Long Term Pavement Performance (LTTP) program.

In summary, the M-E method allows for more accurate field behavior estimation by virtue of incorporating test-case specific information in addition to field-tested empirical models. The downside is the need for several variables as input into the models and specialized testing required for determination of the resilient modulus. As in the AASHTO method, the M-E method also relies on correlations based on material properties for

estimating field behavior. However, it has been shown to be more appropriate for estimating field behavior (Al-Quadi, 2006).

2.3 Typical Usage of Geosynthetics in Pavements

Geosynthetics are used in roadways for stabilization or reinforcing, separation from the subgrade layer, filtration, lateral drainage etc. In most literature, the term reinforcement is used more commonly than stabilization. However, stabilization is as common if not more, than reinforcement. Reinforcement refers to the strength addition from the geogrid or geotextile. On the other hand, stabilization is the strength retention through locking particles in place. The focus of this document is stabilization effect of geosynthetics. The stabilization and separation functions are the most common. As shown in Figure 2-8, the geosynthetics distribute the applied vertical load over a larger area, thereby decreasing the stress transmitted into the subgrade. For this reason, the geosynthetic is generally placed at the interface of the base layer and subgrade, while also benefiting from the convenience for construction standpoint. While both, geogrids and geotextiles can be used to achieve the required load distribution from the base layer to subgrade, they differ slightly in terms of their primary modes of interaction with the base layer aggregates.

Another important additional benefit, especially with geotextiles is the separation effect between the subgrade and the base layer. Intrusion of fines is common with changes in water table elevation/pore water pressure in the subgrade over time. Loss of aggregate layer during compaction and pre-stabilization of the roadway is also very common in soft subgrades. Both these actions are detrimental to the durability of the pavement. In such cases, a geotextile can be extremely beneficial, as illustrated in Figure 2-9.

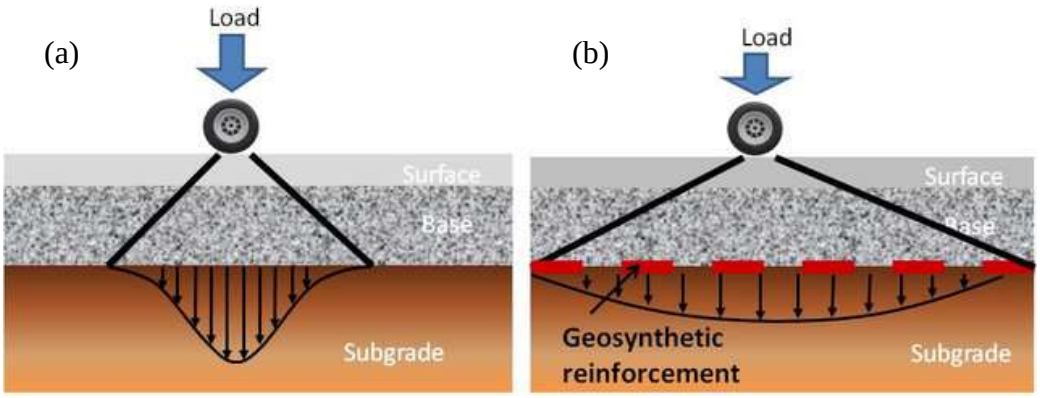

Figure 2-8 - Distribution of surface stress at subgrade level in (a) unstabilized and (b) stabilized flexible pavements (Zornberg, 2010)

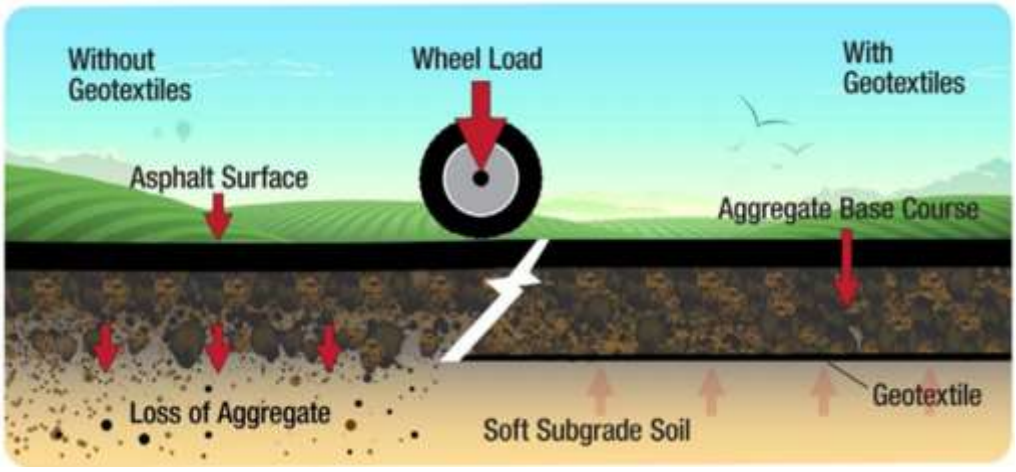

Figure 2-9 - Separation Effect of Geotextile between Subgrade & Base Course (Lacina, 2011)

The following section briefly describes the modes of interaction between geosynthetics and the pavement systems.

2.4 Mechanisms of Geosynthetic Interaction in Pavements

Previous studies have shown that geosynthetics interact with pavement layers in three main mechanisms, (a) lateral restraint, (b) increased bearing capacity, and (c) tensioned membrane effect (Giroud and Noiray, 1981; Giroud et al., 1985; Perkins and Ismeik, 1997; Holtz et al., 1998). These mechanisms are illustrated in Figure 2-10, and briefly discussed in the following sections.

2.4.1 Lateral Restraint

The most important mechanism of interaction is by lateral restraint (Figure 2-10a); where the aggregate particles are restrained from lateral spreading under the cyclic traffic loads. Since the particles are confined, improved force chains can develop through particle contacts causing the effective base layer stiffness to increase. In the case of geogrid stabilization, lateral confinement is induced by the interlocking effect of aggregate particles within the geogrid apertures (Giroud, 1985; Milligan and Love, 1985; Barksdale, 1989; Webster, 1993; Giroud and Han, 2004; Zornberg, 2011; Archer, 2012). Meanwhile, geotextiles rely on mobilization of shear resistance through interface friction with the aggregate particles (Giroud and Noiray, 1981; Zornberg, 2011). In both cases, the tensile stiffness plays an important role in transferring some portion of the vertical load to the horizontal direction through the geosynthetic ribs or fibers. Geotextiles have an added benefit of being excellent at preventing contamination of the base layer by effectively separating it from the subgrade. Geogrids also enable this, albeit to a lesser degree, by developing a stiff interlocked layer, which prevents the intermixing of materials.

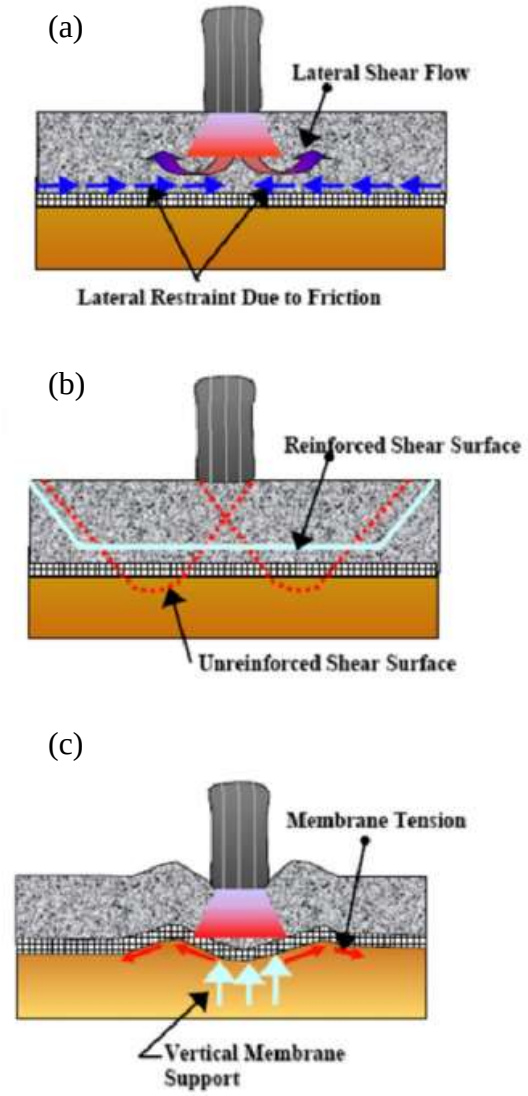

Figure 2-10 - Mechanisms of interaction between geosynthetic and pavement system (Holtz et al., 1998)

2.4.2 Increased Bearing Capacity

Geosynthetics restrict the bearing capacity failure surface to within the base layer with a much higher capacity than the original failure surface which extends into the subgrade (Figure 2-10b). The effect is more evident in unpaved roads with very soft

subgrade regions. Previous studies have quantified the allowable stresses on subgrade soil, depending on the type of geosynthetic present in the interlayer (Giroud and Noiray, 1981; Giroud and Han, 2004). An unstabilized pavement can withstand a stress of $3.14c_u$, where c_u is the undrained shear strength of the soil, while inclusion of geogrids and geotextiles increase this capacity to $5.71c_u$ and $5.14c_u$, respectively. This difference between the cases with geotextiles and geogrids is attributed to the difference in stress orientation at the base/subgrade interface, which in turn results from the difference between geotextile/granular material interface friction and geogrid/ granular material interlocking.

2.4.3 Tensioned Membrane Effect

In regions with very soft subgrade which are prone to excessive rutting, the pavement deforms under the wheel path as shown in Figure 2-10c. As a result, the geosynthetic develops tension forces across the rut forming a tensioned membrane. The vertical component of the tension counteracts the tire load, thereby reducing the net downward vertical force on the subgrade. However, this effect is mobilized only after excessive rutting has occurred and in regions where the CBR is below 3.0 (Barskdale, 1989).

Among the three mechanisms mentioned above, the lateral restraint is significantly more dominant than the other two. The main benefit of this mechanism is that very little deformation is required for lateral restraint to mobilize and hence contributes the most through the operation of the pavement. For this reason, the composite layer comprising the aggregate and geogrid is commonly referred to as the Mechanically-stabilized layer (MSL). The lateral restraint action is schematically shown in Figure 2-11 (Tensar Corp, 2010). The

particles immediately surrounding the geogrid are tightly interlocked with the geogrid apertures restricting their lateral motion, referred to as the fully-confined zone in Figure 2-11. Particles further away experience decreasing geogrid-induced confinement.

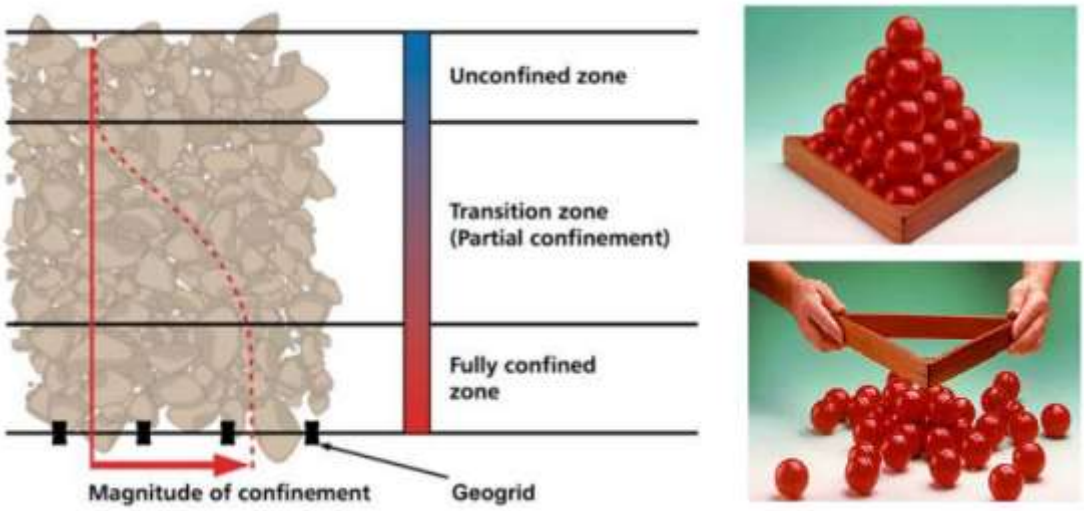

Figure 2-11 - Lateral restraint of particles via interlocking with geogrid apertures (Tensar Corp, 2010)

2.5 Geosynthetic-stabilized Pavement Design

Incorporating geosynthtics into traditional pavement design frameworks like the AASHTO method has been complicated. In the past, the effect of geosynthtics has been incorporated indirectly in two ways. Geosynthetics allow for reduced thickness of base layer for the same design life-span, or a greater life-span for the same layer thicknesses. These two aspects have traditionally been quantified using the Base Course Reduction (BCR) or the Traffic Benefit Ratio (TBR). The BCR is defined as the percent reduction in the base-course thickness with a geosynthetic material in relation to the base-course thickness in the unstabilized pavement, to reach the same state of distress. It has been

incorporated into the AASHTO method, where it is referred to as the layer coefficient parameter. The TBR is the ratio of the number of load cycles on a stabilized section to reach a given rut depth and the number of load cycles on an unstabilized section to reach the same rut depth (Berg et al, 2000). To incorporate the TBR in the AASHTO method, the total anticipated ESALs over the design life of the pavement is multiplied by the TBR.

The majority of studies in the past have quantified the effect of geosynthetics in terms of TBR or BCR. A study by Anderson and Killeavy (1989) conducted field tests and observed that a geotextile-stabilized 350 mm thick base course layer performed the same as 450 mm-thick layer. Webster (1993) showed that a section with a geogrid only needed a 150-mm thick base layer to perform similar to a 250 mm-thick base layer. These two examples exhibit a BCR of 22 and 40% respectively. Similarly, the TBR values range from 1.5 and 10 for geotextiles and between 1.5 and 70 for geogrids (Shukla, 2002) depending on the stage in pavement life-span. The chart in Figure 2-12 illustrates the benefit of geogrids measured in terms of TBR.

The TBR and BCR represent an indirect technique to account for the presence of a geosynthetic in design. Additionally, there have been other guidelines that are specifically aimed at geosynthetic-pavement design (Giroud et al., 1985; Haas et al., 1988; Tingle and Webster, 2003; Giroud and Han, 2004). Haas et al., 1988 proposed to modify the AASHTO method to incorporate geogrid effects by setting the structural number of the reinforced granular layer equal to the ratio of thicknesses of unreinforced and reinforced layers. Tingle and Webster, 2003 present the methodology for geotextile-reinforced unpaved road design developed by the Army Corps of Engineers. The ultimate bearing capacity of subgrade was determined as the product of the undrained shear strength (correlated with CBR) and the

bearing capacity factor, Nc. The Nc term was back-calculated from full-scale road tests and recommended to be 2.8, 3.6 and 5.8 for unreinforced, geotextile-reinforced, and geogrid-reinforced unpaved roadways, respectively.

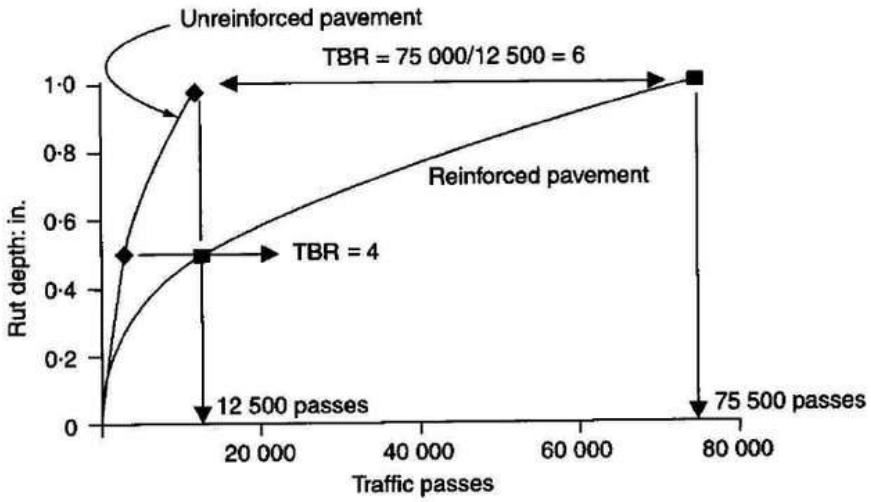

Figure 2-12 - TBR values for a geogrid-stabilized in relation to an unstabilized pavement section (Shukla, 2002)

Giroud and Han (2004) is the most recent method for the design of geosynthetic reinforced unpaved roads, and considers stress distribution at depth, base course resilient modulus, and degradation of material stiffness with repeated loading. This was a revised methodology to the one proposed in 1985 by the same authors. The 1985 method only considered traffic volume, wheel load, tire pressure, subgrade strength, and rut depth. The 2004 method incorporated stress distribution on the subgrade, the shear strength of the base coarse material and its resilient modulus, the interlock mechanism between aggregate and geogrids, and the geosynthetic in-plane stiffness (aperture stability modulus, J) for unpaved road design parameters for the design. The benefits of using geogrids and the quantification

of the aggregate-geogrid interlock are taken into consideration by using the geogrid aperture stability modulus, J, and an Nc value according to the reinforcement type. For unreinforced unpaved roads, the Nc value is equal to 3.14, while for geotextile and geogrid reinforced unpaved roads is 5.14 and 5.71, respectively.

In summary, incorporation of geosynthetics into empirical design methods cannot be done directly. On the other hand, the M-E approach is complicated in itself, that is based on several factors including material properties, distress modes, climactic variables as well as empirical models. Geosynthetics would add another layer of complexity into the approach. At this time, neither the AASHTO method (1993) nor the MEPDG (2004) include guidelines for geosynthetic-stabilized pavement design. The other geosynthetic-design methods were developed based on locally conducted tests and encounters difficulties when generalized to the multiple geosynthetics available in the market today.

2.6 Assessment of geosynthetic-stabilization of pavements

Several studies have been conducted in the past to study the performance effects of geosynthetics in pavements (Robinson et al., 2017). Full-scale tests and accelerated pavement tests are typically most indicative considering the closeness to real operational pavements, but they are also very expensive and time-consuming to conduct. Laboratory tests offer the benefits of controlled conditions and low costs, but often fall short in replicating the actual behaviour of pavements. Numerical studies are growing in popularity with advancing computing technologies and offer extreme flexibility in modelling specific behaviour. On the downside, it is difficult to validate them and extrapolate their results into the full-scale pavements. Figure 2-13 depicts these aspects in a succinct manner.

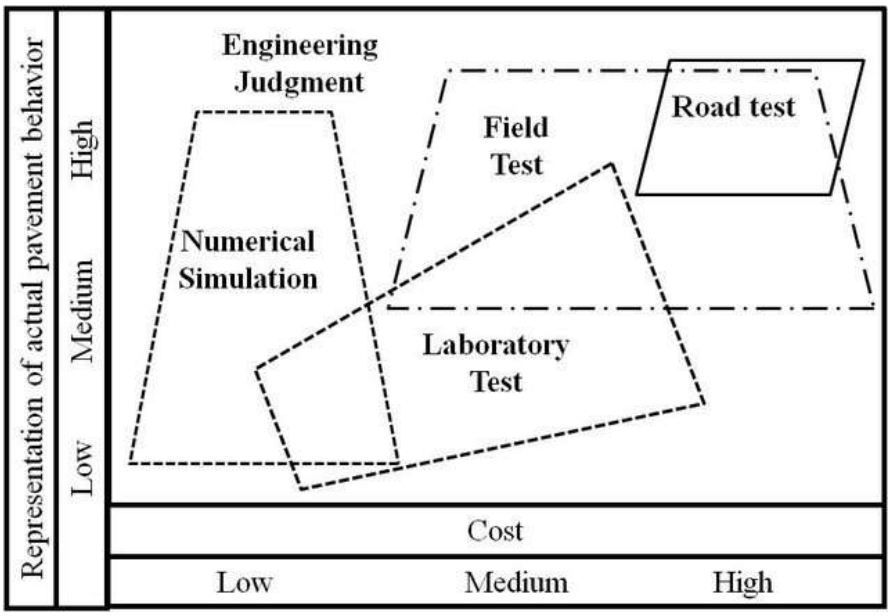

Figure 2-13 - Comparison of various techniques used for pavement performance assessments (Hugo et al, 1991)

The following sub-sections summarize the technical literature available on the specific aspects that are focussed on in the current study, i.e., effect of subgrade stiffness, aggregate size and shape, geogrid properties and placement in the base layer.

2.6.1 Effect of Subgrade Stiffness

Traditionally, the subgrade stiffness has been expressed in terms of the CBR of the subgrade. Soils with high fraction of clay or silts are difficult to compact and very weak under traffic loads, and thus prone to excessive rutting. The GDOT pavement design manual states that "weak subgrades can be stabilized mechanically (by adding granular materials), chemically (by adding chemical admixtures), or with a stabilization expedient (sand-grid, matting, or geosynthetics). Stabilization with chemical admixtures (lime, Portland cement, fly ash, and such) is generally costly but may prove to be economically

feasible, depending on the availability of the chemical stabilization agent in comparison with the availability of granular material" (GDOT Standard Specifications Section 814, 2013). Geosynthetics are ideal in such regions to ensure operability of pavements.

The benefits attained by geosynthetics has been observed to be greatest with very soft subgrades, with CBR values below 3.0 (Barskdale, 1989). In this condition, the subgrade is most susceptible to rutting, caused by the high moisture in the soil which creates a lubricating effect among the particles thereby lowering the bearing capacity. Another full-scale study conducted by Cuelho and Perkins (2009) constructed pavements sections with 11 inch base course over subgrade of CBR 1.8. The greatest benefit was obtained using a woven geotextile, which achieved a BCR of 27%, followed by biaxial geogrid. The New Zealand transportation agency also ran laboratory scale tests using a cyclic loaded-tire and observed that up to 50% reduction in rutting was observed with geogrids at a CBR 2.5, but at greater CBR values the gap in performance decreased (Bagshaw et al., 2015).

Love et al., (1987) studied this problem as a foundation bearing capacity problem and noticed that the inclusion of a geogrid layer distributed the loads on the subgrade/aggregate base layer interface, and reduced the amount of shear stresses applied to the top of the subgrade. This load distribution improvement reduced the amount of deformation of the subgrade, and prevented vertical deformation of the aggregate base layer. These conclusions suggested that the reinforcement impact of geogrids would only be noticeable on weak subgrades, due to the fact that stiff subgrades lack bearing capacity issues, and the load distribution provided by the geogrid is not essential for satisfactorily performance. A geosynthetic layer absorbs the horizontal stresses and some portion of the

vertical stresses, reducing the stress intensity over the subgrade. Thus, from the bearing capacity standpoint. geosynthetic effectively help achieve a higher bearing capacity factor (Nc) of the subgrade soil (Holtz et al., 2008).

The stress distribution of surface traffic loads is very useful in the design of the pavement layers. Before layered system theories were developed, Boussinesq's theory was commonly used to determine the stress, strain, and deflection of pavement systems under a concentrated load condition (Boussinesq, 1885). Here the entire pavement structure was considered to be homogeneous, isotropic and elastic. Vertical stresses under the loads are plotted as a function of depth and radial distance from the axis of loading. Stresses are highest at shallow depths, and asymptotically approach zero at a finite depths, following a semi-bell shape. In reality, flexible pavements are layered systems, and therefore cannot be accurately represented by a homogenous mass accurately. In 1945, Burmister developed solutions for a two and three-layer systems to predict stresses in pavement systems using strain continuity equations (Burmister, 1945). This theory still assumed homogeneity and elasticity for each layer, but the base and subgrade layers could be more accurately represented using different thickness and moduli. The modular ratio, calculated as the ratio of elastic moduli of two layers determined the magnitude of stress transmitted from the top layer to the bottom layer. As the ratio (E_1/E_2) increased, i.e. top layer was greater stiffness compared to bottom layer, the vertical stress transmitted into the bottom layer significantly decreased. Figure 2-14 below shows the chart for vertical stress at depth (z) as a function of applied stress (p), radius of loading area (a) and modular ratio (E_1/E_2). It is apparent from that since the stiffness's of layers in a conventional pavement decrease significantly from asphalt, base course to subgrade, the asphalt layer absorbs most of the surface stress,

and only a fraction is typically transmitted to the subgrade. This also emphasizes the functional importance of the top two layers.

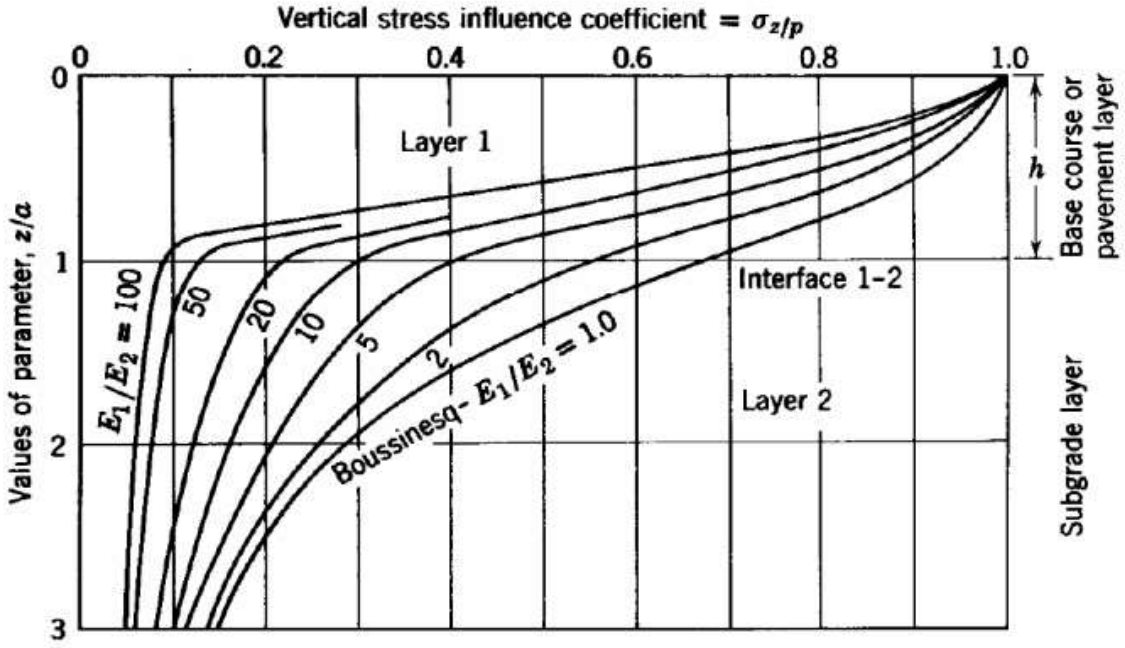

Figure 2-14 - Vertical stress in a two-layer system (Burmister, 1945)

2.6.2 Aggregate Gradation and Morphology

The aggregate material used in the base layer is crucial to be well-graded to form an effective interlocking layer with high stiffness and allow easy drainage. Typically, state agencies define strict specifications for the range of fraction of particles across the various gravel, sand and fines sizes. The GDOT specifications for aggregate gradation is shown in Table 2-1.

Table 2-1 - GDOT specifications for base-course aggregate gradation (GDOT Standard Specifications Section 815, 2013)

Sieve # (in)	Sieve # (mm)	Min fraction	Max fraction
2	50.8	100	100
1.5	38.1	95	100
3/4	19.05	60	90
10	2	25	50
60	0.25	10	35
200	0.075	7	15

Since particle morphological properties define the macroscopic response of the aggregate system under cyclic loading, it is crucial to evaluate the effects of parameters like roundness, roughness and sphericity in pavement systems. It has been shown that particles with greater surface irregularities result in lower permanent deformations (Barksdale et al., 1989). It is also well known that particle angularity increases the shear strength of a granular material, and permanent deformations have been observed to closely correlate to the shear strength of the material (Kwon et al., 2017). Particle angularity has been shown to contribute to strength and stability of aggregate structure through confinement while the surface texture enhances frictional interaction between the particles (Tutumluer et al., 2008). On the other hand, with recent trends towards incorporating marginal recycled materials in the base-layer construction, it is imperative to understand and predict their rutting behavior. By including geogrids in such low-angularity and low-roughness aggregates, the composite shear strength as well as the resistance to permanent deformation has been observed to improve (Kwon et al., 2014). This could help solve the huge scarcity of high-quality aggregates as well as serve as means for usage of recycled materials across the world, thus helping achieve economical construction costs.

This is important especially in studying particle shape effects, since the rotating principal stresses caused by rolling wheels affect rounded particles differently than angular particles (Kim and Tutumluer, 2005).

2.6.3 Effect of Geogrid Location in the Base Course

While geotextiles perform optimally when placed at the base-subgrade interface, where they can also provide separation in addition to stabilization, geogrids pose more options in terms of location that are worth investigating.

Barksdale et al. (1989) conducted large-scale pavement tests to study the performance of geosynthetic stabilization using a 1500-lb moving wheel load. The optimal grid location in aggregate layers comprised of low-quality aggregates is shown to be in the middle of the layer, especially on hard subgrades. On soft subgrades with rutting tendencies, it was recommended to place the grid at or near the bottom, considering the potentially high tensile forces at the bottom of the layer.

Similarly, Webster (1993) assessed the performance of geogrid-reinforced runways to identify the optimal location for geogrid placement using a 30-kip testing cart. The results showed that for runway sections with an allowable surface-rutting equal to 1", geogrid reinforcement allowed them to sustain between 16 and 22 times more traffic than unreinforced runways. The recommended minimum depth of geogrid placement was 6 inches below surface, which includes a 2-inch asphalt concrete layer and 4-inch base layer. The best performance for the 30000-lb tire load (17.25-inch tire width) was however, achieved at a placement depth of 8 inches (2-inch asphalt concrete layer and 6-inch base

layer), as illustrated in Figure 2-15. In addition, a minimum of 4 inches of base layer was recommended over the geogrid to prevent damage during construction.

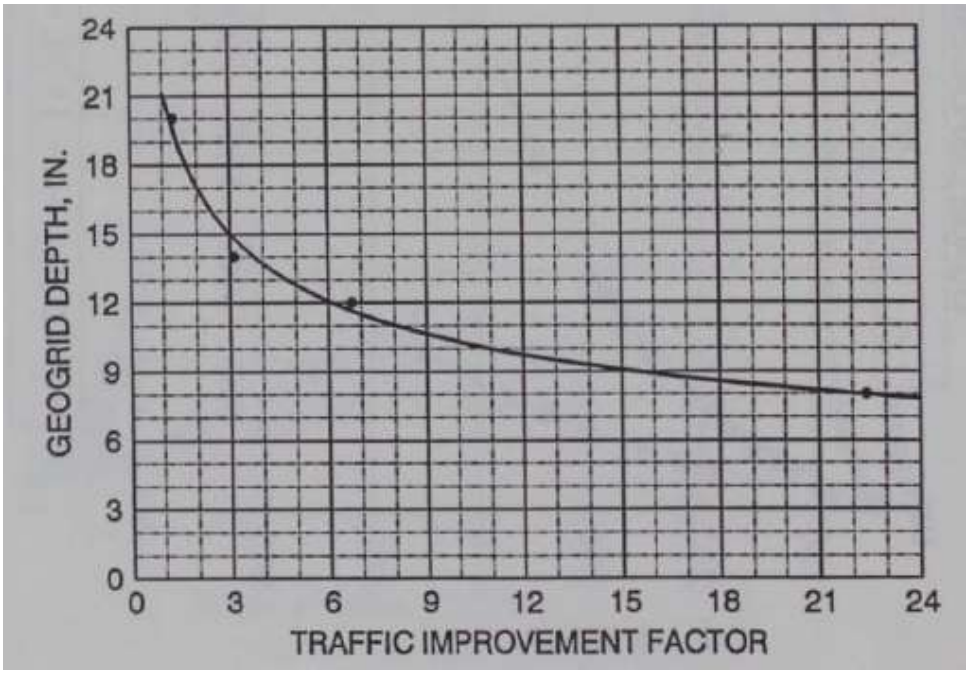

Figure 2-15 - Geogrid placement depth versus traffic improvement factor (Webster, 1993)

Along similar lines, full-scale pavement tests conducted by Al-Qadi et al. (2008) have shown that the most effective location in thin base layers is at the bottom of the base layer, while for a thicker aggregate layer, a single geogrid layer in the upper third of the base layer is optimal. These tests were conducted on eighteen low-volume pavement sections on a subgrade at CBR 4% using an accelerated loading facility. The study found that geogrids were very effective in limiting horizontal shear deformations of the aggregate layer. A photograph of one of the trenched-sections for the control case is presented in

Figure 2-16. The photo shows the rut developed at the surface after testing. This study also observed that geogrid-stabilized specimens showed lesser intermixing with the subgrade.

Figure 2-16 - Post-test specimen trench showing rutting for the control case (Al-Qadi et al., 2008)

Luo et al. (2017) performed large-scale testing on flexible pavements using an 8 feet diameter by 6 feet high circular steel tank. Again, the benefits from geogrids were observed to be greatest when placed at the center for thick aggregate base layers exceeding 10 inches thickness, and at the bottom (interface of subgrade and base course) for thinner base course layers, ranging between 6-10 inches. Abu-Farsakh (2016) made similar recommendations based on laboratory repeated-load testing and FEM analysis.

Perkins et al. (1999) conducted large-scale laboratory test study investigating reinforced geogrid pavements in a large concrete box using a cyclic normal 40kN-load. The test results demonstrated significant improvement in pavement rutting performance over soft clay subgrade prepared at CBR of 1.5. At a CBR of 20, little to no improvement was observed from the geosynthetics. Among geogrids, the stiffer geogrid was observed to perform better, keeping all other variables the same. Moreover, the influence of geogrid location was evaluated at both the subgrade-base interface and 100 mm up in the 300 mm thick base layer. It was found that the geogrid placed higher up in the base performed significantly better.

A very recent study by Mahaffay et al. (2019) studied the performance of several geogrids and geotextiles in thicker flexible pavement structures for airport pavement applications. Cyclic plate load tests were conducted 1.8 x 1.8 1.32 m (6 x 6 x 4.3 feet) specimens comprising of 127 mm (5-inch) asphalt, 178 mm (7-inch) base course and 305 mm (12-inch) subbase layers. The subgrade layer was 711 mm (28 inches) in thickness and prepared at a CBR of 3.0. The geosynthetics were placed at two distinct locations, i.e. at the base-subbase and subbase-subgrade interfaces. The results consistently showed that geosynthetics placed closer to the surface, i.e. at the base-subbase interface achieved greater reduction in rutting.

2.6.4 Effect of Aggregate to Geogrid Opening Size Ratio

An optimal grid opening size is of great importance to establish a high degree of interlocking with the aggregate particles and effectively create a composite layer of enhanced stiffness.

It was not until studies conducted by Webster (1993) that aggregate interlocking was accepted to be the main mechanism associated with aggregate-geogrid interaction. For example, one of the previous hypotheses was local reinforcement around the geogrid (Chan et al., 1989). Webster (1993) observed that unstabilized test sections showed significantly greater lateral flow than stabilized specimens did after full-scale traffic loading tests, which was attributed to aggregate interlocking in the geogrid apertures. This mechanism was further demonstrated by Hufenus et al. (2006), using a full-scale road test using a geogrid placed over a geotextile at the aggregate-subgrade interface. The performance of this section was significantly diminished compared to just a geogrid stabilizer, showing the importance of aggregates to be able to interlock in the apertures.

Brown et al. (2007), conducted repeated-load normal loading setup (referred to as the Composite Element Test) using 50-mm (2-inch) gravel ballast and a range of geogrids with varying opening sizes targeted for railway applications. The interlocking between the aggregates and geogrid was maximum with geogrid of opening sizes between 60-80 mm (2.4 – 3.15 inches). In other words, geogrids with rib length between 1.2-1.6 times the mean particle dimeter performed best. These results are shown in Figure 2-17.

The FHWA guidelines as well as the guidelines recommend the use of geogrids with opening ranging between D_{50} and $2.D_{85}$ of the graded-aggregate material (FHWA, Technical Specification, MRTS58 Subgrade Reinforcement using Pavement Geosynthetics).

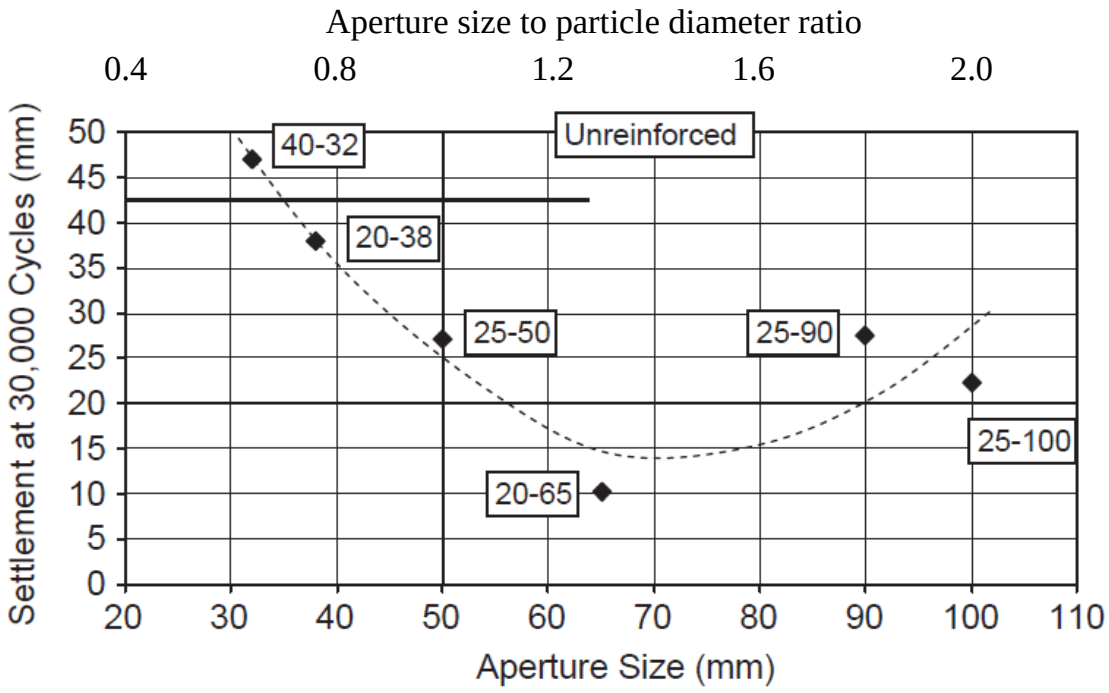

Figure 2-17 - Influence of geogrid aperture size on surface settlement (Brown et al., 2007)

Indraratna (2013) conducted large-scale direct shear tests using 35-mm railway ballast and geogrids of opening size ranging between 21 mm to 88 mm. The greatest interface shear strength, and therefore interlocking, was observed with geogrids with opening sizes between $1.15D_{50}$ to $1.3D_{50}$. The authors also identified the range for any appreciable interlocking to be $0.9D_{50}$ to $2.5D_{50}$. Indraratna (2013) also studied lateral displacement of 35-mm ballast particles in a cubic-triaxial setup (800 x 600 x 600 mm) with moveable walls. Geogrids and nonwoven geotextiles were placed at the bottom of the 300 mm-thick ballast layer, and the geogrids outperformed geotextiles on account of the benefits of mechanical interlocking. The study found that geogrid place at 65 mm above

sub-ballast layer showed the least spreading, indicating best geogrid-aggregate interlocking.

2.6.5 Effect of Geogrid Stiffness

Geogrids stiffness is another variable that has been studied in the past as an influencing variable. Geogrids with high tensile modulus, dissipate greater lateral forces thereby reducing vertical stresses over the subgrade (Perkins, 1999, Brown et al, 2007, Qian et al., 2011, Abu-Farsakh, 2009). The extent of this benefit is not clear, especially in relation to benefits of interlocking. There are also concerns that stiff geogrids could inhibit compaction, leaving large voids surrounding itself, which would obstruct strong particle contacts.

Table 2-2 presents a succinct summary presented in Han et al. (2011) (which was modified from Webster, 1992) on the influence of various geogrid variables like rib thickness and shape, stiffness, aperture size and shape and rigidity, junction strength and grid stability on overall performance of the pavement.

Identifying the best design parameters for geogrid location, opening size and stiffness is very difficult to isolate from other interplaying variables like inter-aggregate interactions, experimental biases and shortcomings, and also difficult to generalize to other fully-graded aggregate materials. This is even harder to study using laboratory experiments. As a result, there is uncertainty over the reasoning for certain combinations to perform better than others.

Table 2-2 - Influence of various geogrid properties on pavement performance (Han et al., 2011)

Geogrid Item	Property	Test Standard	Judgment
Rib	Thickness	ASTM D1777	Thicker is better.
Rib	Stiffness	ASTM D6637	Stiffer is better. Need test to measure stiffness.
Rib	Shape	NA	Square or rectangular are better than rounded or curved shapes.
Aperture	Size	NA	Related to base aggregate size. Optimum size not known. .75 to 1.5 in. probably good target range.
Aperture	Shape	NA	Round or square is better.
Aperture	Rigidity	ASTM D6637	Stiffer is better.
Junction	Strength	(GRI – GG2)	Need some minimum strength. All geogrids tested were adequate.
Grid	Secant Modulus	ASTM D4595	Need minimum secant modulus value. Optimum not known.
Grid	Stability	ASTM WK24635	The "Grid Aperture Stability by In-Plane Rotation" test developed by Dr. Thomas Kinney shows good potential for traffic performance relationships. A minimum secant aperture stability modulus as a specified torque may be a good index test requirement.

2.7 Previous Discrete Element Modelling (DEM) Studies

In the past two decades, increased computational power has allowed development of advanced modelling techniques to study several real-world materials and their behavior. Discrete Element Modelling (DEM) has extensively been used to model granular material

in many different study areas, including pavements and been very successful in its implementation. Part of the reason for its success is the ability to gather information from each individual particle, which is a significant advantage over laboratory experiments.

McDowell et al. (2006) conducted a comprehensive study using the 3D DEM technique to assess ballast-geogrid interaction using pullout tests, with and without geogrids. The particles were modelled as spheres as well as cubic clumps, and their interaction with geogrids was studied at various confining pressures. The geogrids were modelled as a series of small spheres connected by contact and parallel bonds. The average normal contact force and shear contact force at the end of the tests showed high concentration around the geogrid, which was attributed to ballast interlocking. In this study, the optimal geogrid aperture size to particle diameter ratio was found to be 1.4, in agreement with previously mentioned experimental studies. In a later study by Ferellec and McDowell (2012), particles were modelled as clumps of 55-spheres and observed even higher contact forces, potentially indicating greater interlocking. Qian et al. (2011) also studied the optimal ratio for geogrid opening size to particle diameter, by simulating plate load tests conducted by Brown et al. (2007) and observed similar results of about 1.625.

Chen et al. (2012) focused on understanding the force distribution on different aggregate gradations and finding the larger particles in the aggregate carried the most forces. Clumps were modeled using the approach from Lu and McDowell (2007) and their size ranged from 0.075 mm to 16 mm. A box test, based on McDowell (2005) was simulated using PFC 3D, to generate a specimen of dimensions 700 x 300 x 450 mm. The authors found that large particles tended to carry the largest contact forces because they had the largest amount of contacts. Improved performance was observed for biaxial geogrid locations

between 100-150 mm above the base, as compared to 50 mm or 200 mm above the base. Addition of a second layer of geogrid showed the greatest increase in performance in terms of surface settlement and resilient modulus. Authors also stated that the reinforcement zone of geogrid-reinforced ballast lies approximately 50 mm above and below the geogrid, based on post-simulation displacement vectors shown in Figure 2-18.

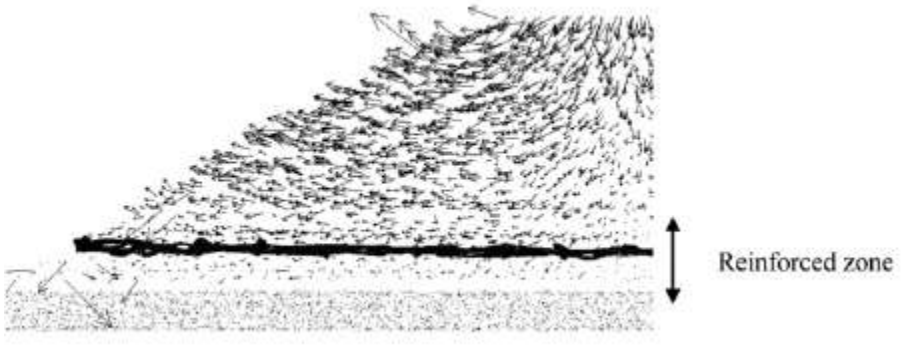

Figure 2-18 - Total displacement vectors in left half of the sample (Chen et al., 2012)

Peralta (2016) conducted an extensive study into modeling of geogrids and their interaction with aggregate mixtures of different morphologies and gradation. The morphologies that were studied included spherical particles and 2- and 3- particle clumps, while the gradation was modelled using binary mixtures of two particle sizes. In total, two binary mixtures were studied, one where the larger diameter particles were 50% of geogrid rib length, and the second with larger particle diameter being 70% of geogrid rib length. Cyclic load tests were simulated using a cylinder repeatedly falling on the aggregate specimen with the geogrid placed at the middle. Simulations showed that the mixture with larger particle being 50% of rib length showed lower rutting, and thus, greater compatibility with the geogrid. Moreover, the change in porosity in the bottom half of the stabilized

specimens was negligible with the 50% mixture, indicating the geogrid was efficiently distributing applied loads. However, in the case of the 70% binary mixture, the change in porosity was much greater, and even equaled the change in porosity in the upper half of the specimen. This indicates that sufficient interlocking did not develop due to incompatibility in particle-opening sizes.

In summary, while the effect of geosynthetic stabilization on pavement performance is best-assessed using full-scale sections to fully replicate the operational conditions, these procedures are time and cost-intensive to implement. On the other hand, laboratory tests like cyclic triaxial tests and repeated-load plate tests are ideal for measuring design parameters of individual materials like resilient modulus but are not ideal for studying composite aggregate-geosynthetic-subgrade systems. In addition, multiple researchers have observed that the performance of aggregate materials in the field cannot be predicted using resilient modulus tests (Thompson 1998; Xiao et al., 2012; Mishra., 2012; Kwon et al., 2014). Instead, laboratory permanent deformation tests are a better indicator, and can be greatly beneficial to predict field performance of previously untested geogrid-aggregate combinations.

CHAPTER 3. BENCH-SCALE RUTTING TEST SYSTEM

Traditionally, the performance of geosynthetic-stabilization has been evaluated using full-scale test sections subjected to repeated-trafficking by a loaded truck. While, this method provides the most representative information regarding operational performance of the test section, it is cost and time consuming. On the other hand, laboratory tests like cyclic triaxial tests and repeated-load plate tests are widely employed for pavement testing, although these methods are typically used for measuring the material properties like resilient modulus of aggregates and soils. Resilient modulus is an important parameter that represents the long-term ability of the pavement to withstand repeated traffic loading, and also used as an input in the AASHTO MEPDG design framework. However, studies by multiple researchers have shown that the performance of aggregate materials in the field cannot be predicted solely using resilient modulus tests. In this regard, permanent deformation tests or rutting tests can be greatly beneficial to predict full-scale performance of geosynthetic-aggregate combinations (Thompson 1998; Xiao et al., 2012; Mishra., 2012; Kim et al., 2017). Kim et al. (2005) also stated the primary distress mode in unsurfaced pavements is rutting, and added that recent studies have shown that full scale tests with actual traffic loadings have shown increased permanent deformation when compared to plate load tests in the lab.

To accurately estimate permanent deformations in laboratory tests, it is important to replicate field conditions as closely possible including aspects like moving wheel loads and mobilization of geosynthetics' tension effects. Han et al (2011) recognized the following desired characteristics for a laboratory procedure to measure permanent

deformation: (a) be applicable to all types of geosynthetics, (b) geosynthetic must interact with base course material, (c) development of local deformation, (d) repeated loading applied by wheel-tracking motion, and (f) easy, quick and inexpensive. For example, aggregates have been observed to displace in a fishhook pattern under uni-directional wheel loading, where they are pushed forward and laterally outwards from the wheel (Lipomi, 2014). An illustration of this effect is shown in Figure 3-1.

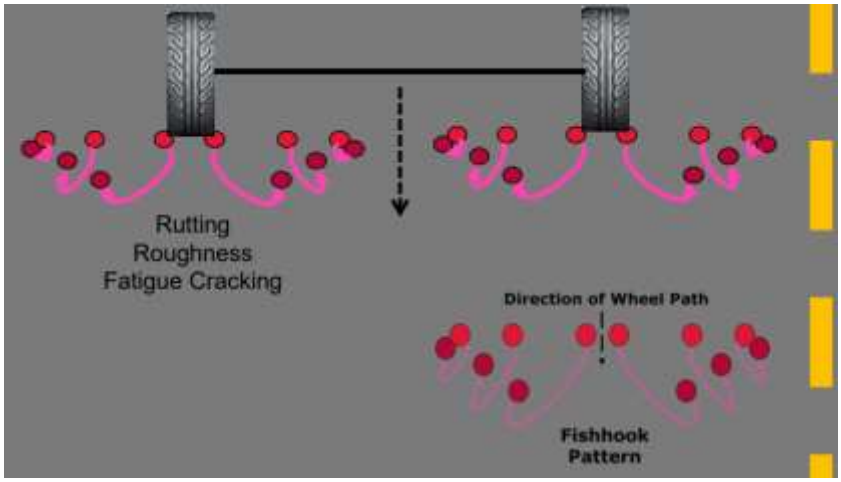

Figure 3-1 - Fishhook pattern of particle movement under moving wheel loads (Tensar, 2015)

Recognizing these needs for a new laboratory procedure, a bench-scale rutting system was designed and developed as part of this research study. The following chapter describes the design and functionality of the apparatus, test procedure and steps taken to validate the test results obtained from the system.

3.1 Bench Scale Testing System

The bench-scale rutting apparatus simulates the behavior of a pavement in response to repeated-wheel loading and facilitates the measurement of permanent deformation and stress variations in the subgrade. Figure 3-2 shows the components of the apparatus.

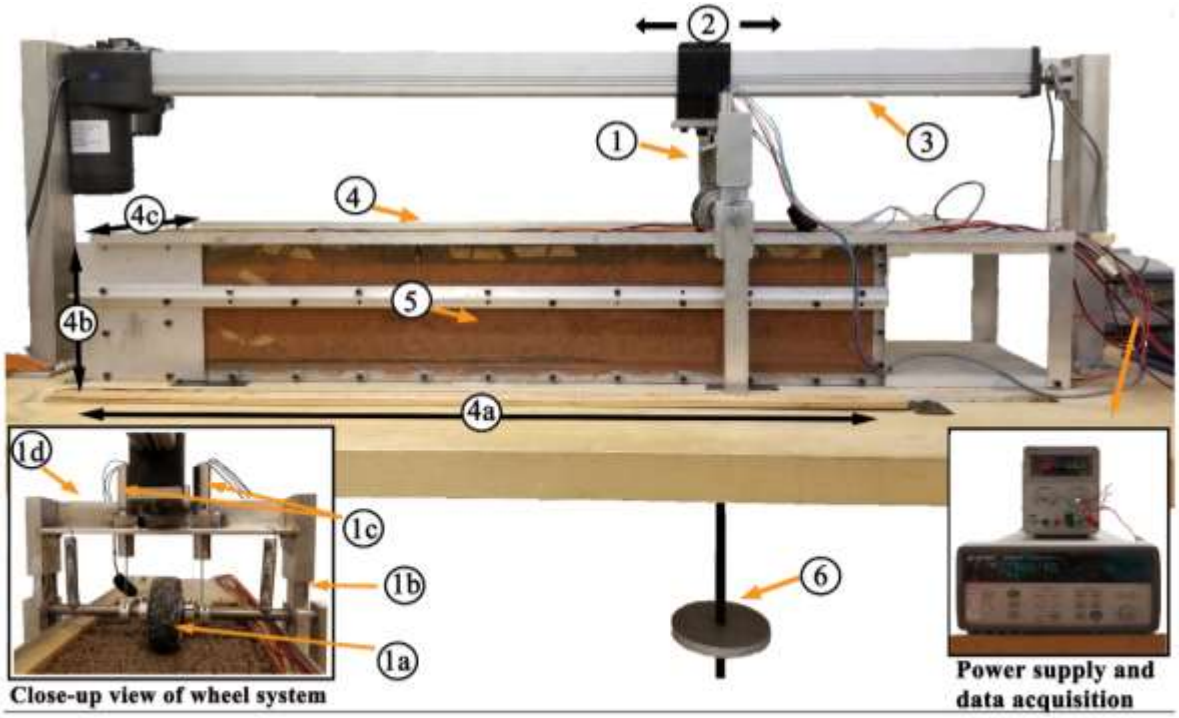

Figure 3-2 - Schematic showing the rutting apparatus

The test assembly comprises of three sub-systems, the specimen chamber, the wheel propagation system and the loading suspension system. Details regarding instrumentation is also presented below.

3.1.1 Specimen Chamber

The specimen chamber, measuring 36 inches (914 mm) × 8 inches (203 mm) × 6 inches (152 mm), houses the test specimen. These dimensions allows for several favorable features like high rates of testing compared to full or large-scale testing, as well as a high degree control over specimen preparation. Further, the full specimen of length 36 inches (914 mm) was sub-divided into three sections of 12 inches (305 mm) each. Each of these sections was tested individually over a length of 8 inches (203 mm). This test-specimen size encompasses a sufficient sample size to study the rutting behavior, along with adequate buffer spacing of 2 inches (51 mm) between the test sections. To confirm the validity of this arrangement and ensure non-interference between test sections, trial tests were conducted with the three-specimen and single-specimen arrangement.

Therefore, each full test specimen prepared enabled three individual tests, which further accelerated the testing rates. An important added benefit is that any error associated with specimen preparation is removed, since each set of tests are conducted on the same full-specimen thus enabling a fair comparison in performance. The front wall of the chamber is a transparent Lexan polycarbonate sheet, while the other walls and bottom plate of the chamber are made of Aluminum. The transparent front wall provides a cross-sectional view of the specimen along the wall.

3.1.2 Wheel Propagation System

The wheel-propagation system is comprised of a micro-controller driven track actuator installed over the chamber, which connects to a 3-inch (76 mm) diameter and 1-inch (25.4 mm) wide wheel. PA-18 linear track actuator of stroke 40 inches (1 m) was

chosen as primary locomotion system. It operates on 12VDC input, maximum load capacity of 150 lbs. (68 kg) and can move at maximum speed of 1.2 inches/s (20.5 m/s). A hall-effect transducer was installed on the module of the actuator to enable position tracking along the stroke length. The actuator was controlled by an Arduino Uno Rev3, These components were obtained from Progressive Automations. A lightweight aluminum-core rubber-tread wheel was purchased from McMaster-Carr to serve as the scaled-down truck-wheel. It measured 3" (diameter), 1-1/4" (width) and 1/2" axle diameter (76 x 32 x 13 mm) with ball bearings. The maximum load capacity of the wheel was 150 lbs. (68 kg).

- The track actuator can controlled be controlled using a micro-controller assembly. The assembly mainly consists of an Arduino board programmed to accept parameters like zero position, start position and end position, which determine the limits of the wheel passes during the test. Owing to the physical limits of the system, these values have to be between 0 and 36 inches (914 mm).
- The speed of the wheel can be set to be a value between 0 and 255, where 255 represents around 1.2 inch/s (20.5 m/s). The time delay at the end of a pass and before the next pass begins can also be set as a time value in milliseconds.
- The Arduino system is fitted with a Hall-effect sensor on the Arduino enables a continuous output of the position and the velocity of the wheel at a pre-defined frequency of 524 micro-second during the test as well. The number of cycles is displayed on an LCD readout panel.

3.1.3 Load Suspension System

Lastly, the wheel is loaded using the dead-load suspension system mounted to the ends of the axle. The wheel and axle assemble is capable to accommodate undulations in the surface of the specimen, without exerting any normal load on the track actuator, which is critical.

3.1.4 Instrumentation

The instrumentation used in the test procedure included linear variable differential transformers (LVDTs) to continuously monitor rutting deformations at the surface as well as pressure sensors to record vertical stresses experienced in the subgrade. The LVDT's were mounted on the wheel frame and the LVDT measuring needle rested on the axle so that any vertical movement of the wheel, which would cause axle movement, would in turn translate into voltage variations sensed by the LVDT. One LVDT were mounted on each side of the wheel so that any tilt in the axle due to uneven specimen surface led to downward and upward displacements being recorded on each side of the wheel, which was then averaged to obtain the true wheel settlements. The make and model of the LVDTs was Trans-Tek Model 0245-00000 with a stroke of +/-2" (51 mm) and a non-linearity of less than 0.5%. Subgrade stresses were measured using A201 Tekscan flexible force sensors of a sensing area of 0.81 in^2 (523 mm^2), corresponding to a diameter of 1 inch (25.4 mm), and a FlexiForce Quickstart Board connection module to interface with the data logger. An input DC-power supply of 6V was used for the quick-start board. These sensors were typically placed under the wheel path at two locations, at the base layer-subgrade interface and at a depth of 1-inch below the top of subgrade.

Finally, these sensors were connected to an Agilent 34970A data acquisition unit, and controlled using the computer. The Agilent Benchlink software was used to view the data in real-time during the test.

3.2 Specimen Preparation

The base and subgrade layer thicknesses for the specimen was chosen by applying a scaling factor to the dimensions of a full-sized pavement section. Typically, field pavement sections are constructed with an 8-12 inch (203-305 mm) thick base layer and the width of a full-size truck wheel ranges between 10 to 12-inch (Figure 3-3a). Following the downscaling step, this proportion was preserved by using experimental specimens with a 1-inch thick base layer along with the 1-inch wide loading wheel. This is depicted schematically in Figure 3-3b. The subgrade layer was typically about 5 inches (127 mm), and represented a continuum media as the bottom boundary to the applied surface loads.

The soil and aggregate materials required for the tests were prepared beforehand by processing and mixing with the desired amount of water. Multiple water content readings were recorded before and after each test to document accurate testing conditions. Once the materials showed equilibrated and desired moistures, the test specimen was prepared as follows.

Specimens were constructed layer-wise in lifts of 1-inch thickness, summing to 4 lifts for the subgrade and 2 lifts for the AB layer. Each lift was compacted to the desired density (based on target CBR value) using a wooden plate measuring 8 x 8 inches and a 12-inch 5.5-lb Proctor hammer. The wooden plate served to uniformly distribute the impact force of the hammer to the full-width of the specimen. A constant compaction energy was

used for each lift of the subgrade layer, by sequentially applying a fixed number of hammer drops along the specimen. Stress sensors were placed at select locations in the subgrade during this stage.

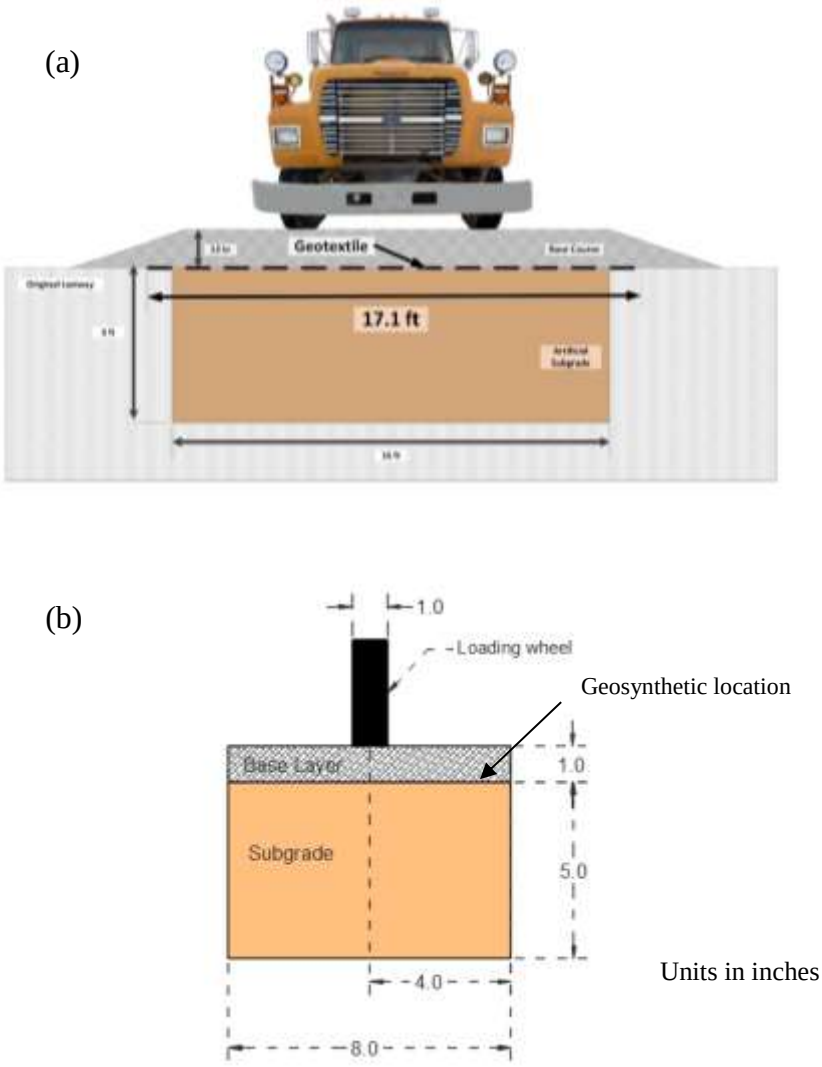

Figure 3-3 - Schematics showing (a) cross-sections of full-scale (after BSI et al., 2014) and (b) bench-scale specimens

The target CBR values for the subgrade ranged between 1.0 and 15.0, while the GAB was compacted at optimum water content to 95% of its maximum dry density

representing a CBR greater than 20. The geosynthetic material, measuring 12 x 8 inches (305 x 203 mm) was placed at the interface between the two layers. Upon completion of the specimen preparation, it was allowed to equilibrate for a duration of 12 hours before the loading stage was started. Photographs of various testing stages including sample preparation, loading and exhumation of geosynthetics are shown in Figure 3-4.

Figure 3-4 - Various Bench Scale Testing Stages: (a) placement of geosynthetic over subgrade, (b) wheel loading cycles in progress and (c) exhumed aggregate layer upon completion of test

3.3 Typical Test Procedure

Once the specimen has been prepared and ready to be tested, the track actuator is mounted over the chamber, wheel frame is bolted to the actuator and the microcontroller assembly is connected to the computer. The dead loads to be applied under the wheel is chosen based on the desired constant stress of 27.6 psi (190 kPa) and the contact area of the wheel with the specimen. This contact area was estimated to be 0.81 inch^2 (522 mm^2), corresponding to a circular diameter of 1.02 inches. The track actuator is then programmed to cycle between two user-defined points along the length of the specimen at a constant speed, typically set to 1.2 inch/s (30.5 mm/s). The data-logger session and the actuator are activated to begin the loading cycles. The specimens were individually tested for a minimum of 250 loading cycles, sometimes up to 500 cycles. A loading cycle is defined as the sequence of wheel passes from the start of the test section to the end and back, covering a total distance of 16 inches per specimen. Typically, the rutting curves showed little change in vertical deformations after 250 loading cycles, indicating stabilization of the layered system. No user intervention is required during the test, until the target number of loading cycle is reached.

3.4 Data Processing

The microcontroller records the wheel position along the 8-inch (203 mm) length of the specimen, which is shown in Figure 3-5 for the first few scan readings. The dashed vertical lines represents the segmentation of this data into cycles, where the wheel changes direction and cycles back and forth along the specimen. The LVDT data produced during the test is presented in Figure 3-6. Figure 3-6 (a) shows the LVDT readings for the first

few cycles and Figure 3-6 (b) shows the LVDT readings for the entire test. In order to simplify this data and extract an average rut depth versus loading cycle plot, the full dataset is processed using a custom-algorithm. This algorithm segments the dataset into cycles based on the associated wheel position data. Using this data, the maximum rut-depth along the length of the specimen is identified for each cycle. Since the specimens were carefully prepared in the laboratory, uniform rut depths were observed along the test-section. Some tests showed marginally greater rut depths at the end-points of the test-sections, owing to the abrupt stopping of the wheel before changing direction. Therefore, measurements made at the left and right 1-inch extremes of the test section were not used in the analysis.

Figure 3-7 (a) shows a typical pressure sensor response collected during a test, with the spikes representing the load exerted by the passing wheel over the specimen surface. Figure 3-7 (b) shows the collected data over the entire test. As before, the maximum pressure per cycle is picked and plotted for further analysis.

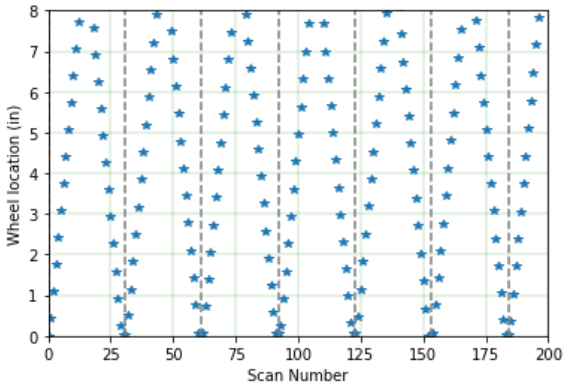

Figure 3-5 - Wheel position readings showing bi-directional cyclic nature and segmentation into cycles

(a)

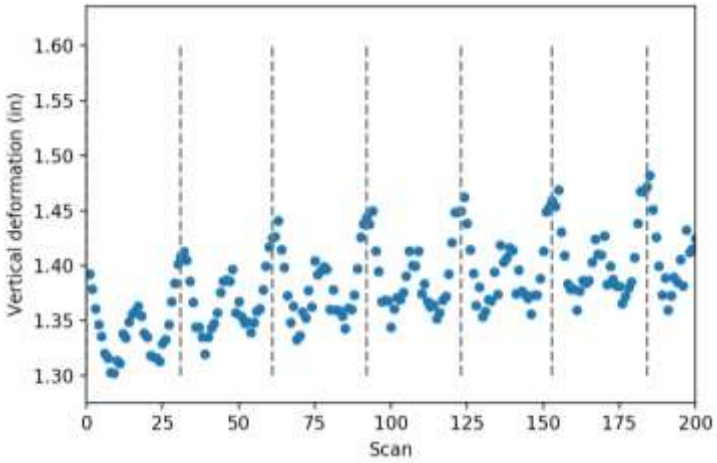

(b)

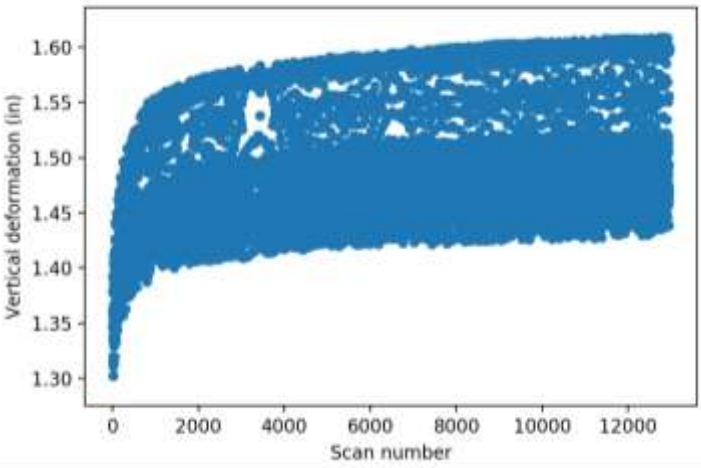

Figure 3-6 - Plot showing typical LVDT readings collected (a) for the first few cycles and (b) for the entire test

(a)

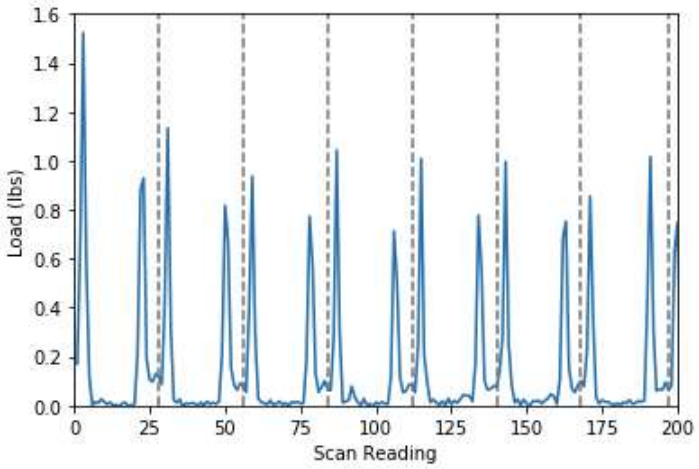

(b)

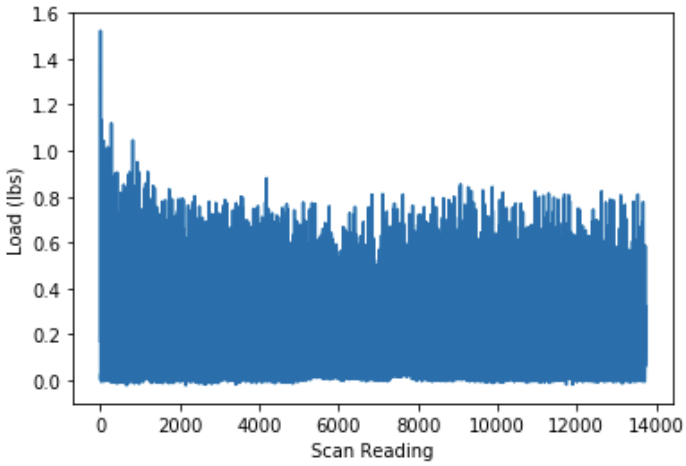

Figure 3-7 - Plot showing typical pressure sensor readings collected (a) for the first few cycles and (b) for the entire test

3.5 Alternative Modes for Experimental Simulation

Apart from the rutting mode described earlier in this chapter and used extensively throughout this study, additional capabilities to perform experimental simulations of other pavement processes was implemented during the design of the bench scale apparatus.

These included the ability to simulate the “slushing” process for inverted base pavements as described below.

3.5.1 Laboratory Investigation of Slushing Technique

The slushing process is applied to the unbound aggregate base layer (UAB) of inverted base pavements, represented by the GAB layer in Figure 3-8, which also schematically presents the differences between a conventional flexible pavement and an inverted base pavement structure.

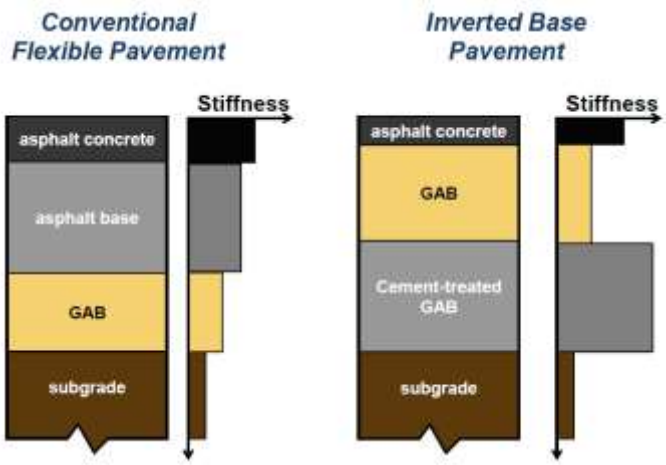

Figure 3-8 - Comparison between conventional and inverted base pavement systems [Papadopoulos, 2014]

Since the UAB layer in an inverted base pavement plays a greater structural role in load-distribution, it is critical to achieve the right composition of particles and minimize voids. Slushing helps achieve this by retroactively removing excess fine particles from an already-placed UAB layer, as opposed to traditionally adopted repeated rolling which leads to particle crushing and could be detrimental to the integrity of the pavement in the long

term (Figure 3-9). The seepage action of water through the compacted UAB layer is critical to the slushing process, as explained below.

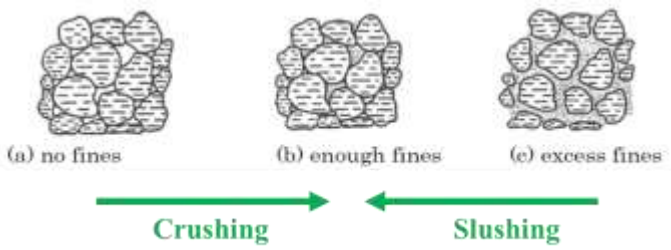

Figure 3-9 - Crushing versus Slushing action in achieving maximum density

This technique involves the following steps during compaction of the unbound aggregate base layer:

- A cement-treated base layer is compacted to ensure a stiff, low-permeability layer to support the overlying UAB layer.
- UAB layer is placed and compacted until it exhibits no (or very little) movement under the weight of a heavy roller.
- The next stage is the slushing process which involves multiple passes by a water truck, a heavy smooth-drum roller and a pneumatic rubber-tired roller, in that sequence. This combination allows the water to seep into the UAB layer and immediately being expelled back to the surface under the action of the following two rollers, while eliminating any excess air pockets and fine particles. Visually, this is observed as air bubbles and fine sediments at the surface indicating the slushing process is underway. This expelled water is removed from the pavement.

- At the end of the slushing stage, indicated by expulsion of clear water at the surface, the UAB layer should contain lesser percentage of voids than pre-slushing and an optimum ratio of coarse to fine particles, thus ensuring higher stiffness and durability.

The cleaned surface is allowed to dry completely and then dry-rolled before applying the tack-coat for asphalt placement.

3.5.1.1 Method:

The 'Slushing' setup was designed as shown in the schematic below (Figure 3-10) and incorporated the following features:

- Two sets of rollers of to each act as steel and rubber-tired wheels. Varying stiffness was captured by using rubber sleeves of different hardness (90A Urethane for harder roller and 60A Vinyl for softer roller)
- Roller weight to be controlled using dead weights hanging independently off rollers
- One directional compaction, capability to retract rollers to origin while elevated from the soil surface to prevent reversal of rolling stresses
- Ability to be speed-controlled and position controlled (micro-controller driven)
- Instrumented to measure and record horizontal load, speed and number of cycles
- Water sprinkler system to spray water at a controlled rate as desired

Figures 3-11 and 3-12 show some additional schematics and photos of the device.

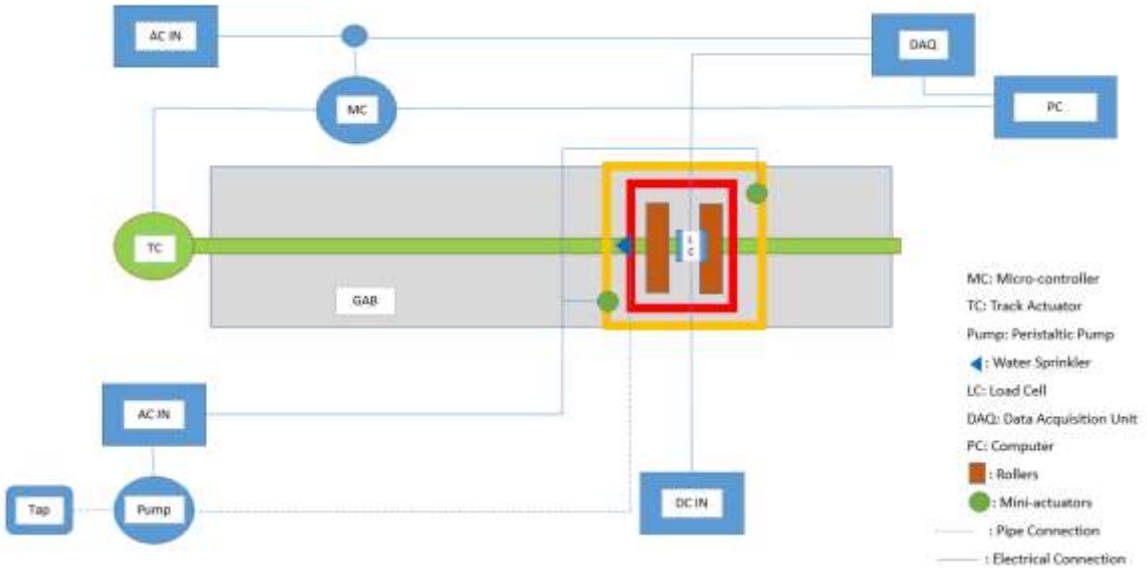

Figure 3-10 - Schematic showing various components involved in testing process

3.5.1.2 Test Parameters:

The gradation of GAB material was modified so as to remove the coarser particles greater than ¾ inches (to scale for reduction in the laboratory roller size as well as make any subsequent core-sampling easier).

GAB was manually compacted during the initial placement stage in four lifts of one-inch thickness. The gab material is mixed to optimum water content (6.5%) prior to placement. This test was run in the following stages, with gradually increasing rolling stress to prevent soil 'bowing':

- Stage I: Surface Preparation: Low stress passes (20 lbs on each roller) to create even surface

- Stage II: Conventional Compaction-I: Moderate stress (36 and 31 lbs on each roller) passes
- Stage III: Conventional Compaction-II: High stress passes (55 and 40 lbs on each roller)
- Stage IV: Slushing: Similar stresses as above but accompanied by water spraying in one direction

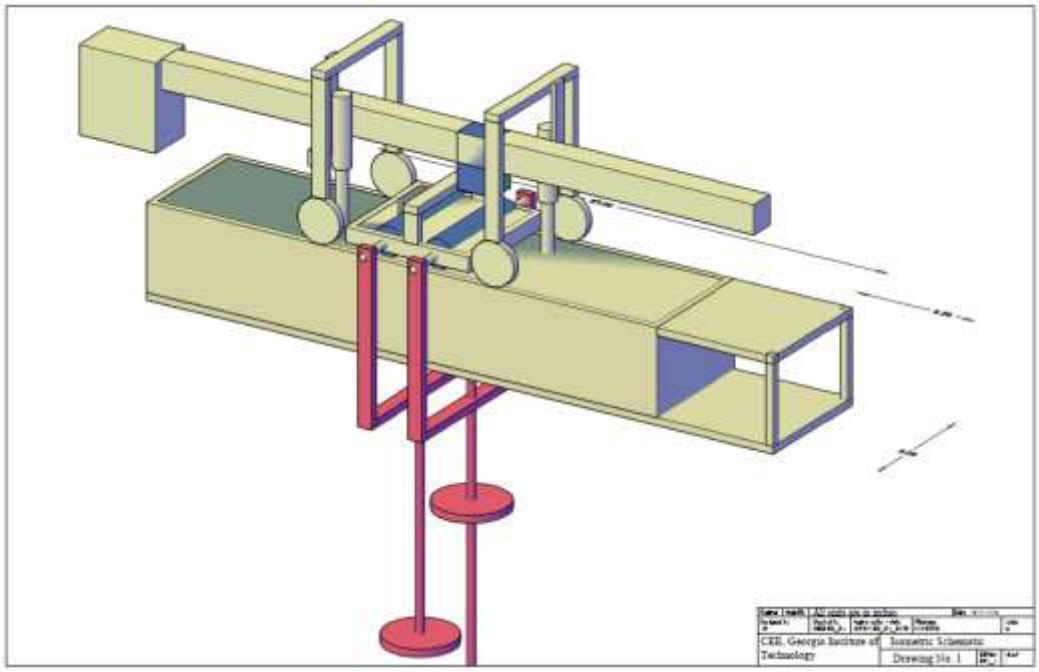

Figure 3-11 - CAD rendering showing concept-design of slushing setup

Figure 3-12 - Photographs of slushing device

3.5.2 Preliminary Simulations

The objective of this section of the study was to primarily develop a working apparatus to simulate slushing and conduct a pilot test to qualitatively observe slushing mechanisms. The following paragraphs present the result from the pilot test.

Figure 3-13 below presents the horizontal load resistance recorded by the load cell while pushing the rollers in the forward direction. Stages I-IV comprised of 1, 5, 5 and 34 passes respectively. The varying vertical stresses on rollers for four stages mentioned above of compaction can be clearly distinguished. The default speed of rolling was set to 0.33

inches/s. Horizontal drag increases upon introduction of water which explains the higher load measurements for Stage IV as seen in Figure 3-13. The orange-colored passes were conducted at higher speeds of 0.44 inches/s and 0.66 inches/s, which is causing the even-higher load readings compared to the previous cycles of Stage IV.

Another interesting observation, which should be closely monitored for future tests is the bell-shaped load curve, with the load reading dropping in the second half of the slushing stage. This is noticed in Stage IV at all three speeds.

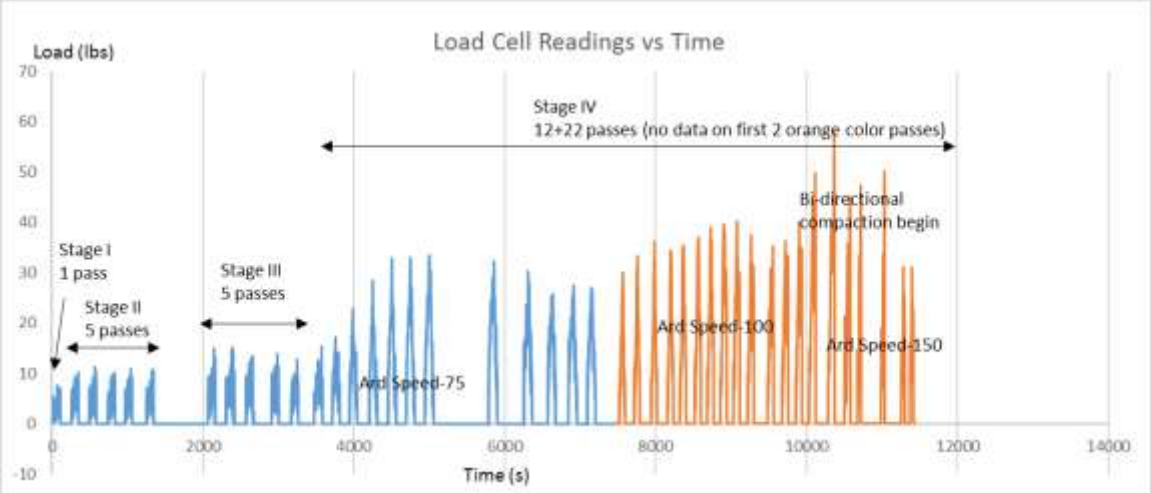

Figure 3-13 - Horizontal load-cell readings for all cycles of compaction

Some photographs from the test are shown below in Figure 3-14. It should be mentioned that while air bubbles and fine particles were ejected across the full surface, the water carrying these ejected particles was subsequently pushed to the side of the box following the roller-passes. Therefore, the photos below indicate greater accumulation of fine particles along the edges of the box, as seen in Figure 3-14 (f), (g) and (h).

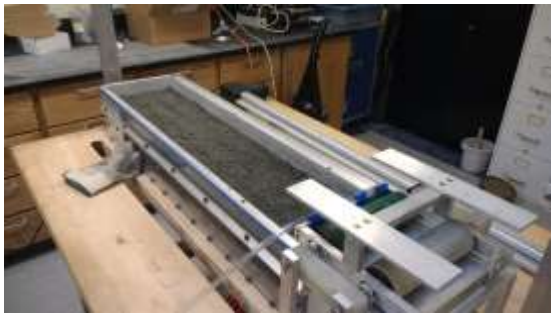

a) GAB placement and compaction

b) Stage I compaction

c) GAB surface pre-slushing

d) Slushing stage underway

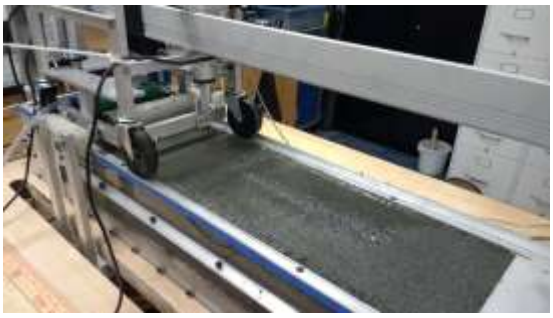

e) Slushing stage in progress

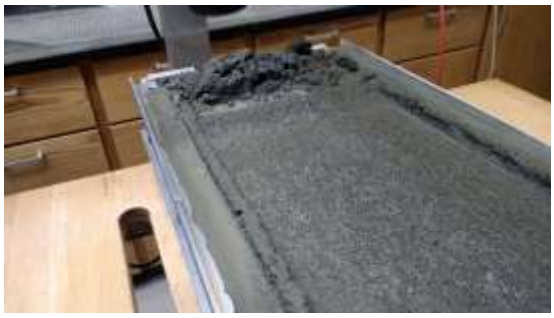

f) Fines being ejected to sides of roller

g) GAB surface after slushing

h) GAB surface after slushing

Figure 3-14 - Photographs from pilot test

Preliminary laboratory simulations of the slushing technique clearly showed the ejection of fine particles at the surface of the aggregate layer along with excess water. This establishes the effectiveness of the laboratory system towards simulating the slushing construction process as followed in the field, while enabling close control over testing conditions and electronic measurements of various metrics to quantify the improvements potentially achievable using this novel technique.

Combining these insights, a base layer that is compacted, within a reasonable range, close to the maximum modified-proctor dry density and optimum water content, followed by implementing the slushing process to further enhance the stiffness of the system would potentially achieve an improvement in resiliency of the system. Moreover, this improvement would be achieved by minimizing void space in the unbound aggregate layer while minimizing crushing of aggregate particles, which is otherwise expected to occur with conventional high-energy low-lubrication compaction techniques.

CHAPTER 4. EFFECT OF SUBGRADE STIFFNESS ON PAVEMENT PERFORMANCE

The research study presented in this chapter was sponsored by the Georgia Department of Transportation to investigate the performance of geosynthetic-reinforced pavements in soft subgrade conditions. The bench-scale rutting system was used to conduct a detailed parametric assessment of the influence of geosynthetics in flexible pavement systems at various subgrade stiffness conditions. This chapter presents the bench-scale testing results, comprising a relative comparison of the behavior of the stabilized pavement specimens compared to the unstabilized specimens, therefore allowing for the quantification of the benefits of geosynthetics.

4.1 Experimental Program

The scope of the bench-scale testing was as follows. Subgrade soils from Coweta Co., Gordon Co. and Hall Co, were identified by GDOT as soft and problematic for pavements in the state and hence, chosen for the testing program. The locations of these soils are shown in Figure 4-1, along with ratings for subgrade conditions used as a design guide by GDOT. Typically, subgrade soils that fall in regions with SSV of 2 or 2.5 are excavated and replaced with better quality granular materials as stated in GDOT standard specifications. Therefore, the Coweta and Hall County soils used in the current testing program are rated with an SSV of 2.5 while the Gordon County soil shows an SSV of 2.0. Sufficient quantities of these soils as well as commercially available graded aggregate base (GAB) material was procured and processed by crushing, drying and remixing to the

desired moisture. With regard to the geosynthetics to be used in the study, Tensar biaxial BX1200 geogrid and Tencate Mirafi HP270 geotextile were initially identified for evaluation. In addition, three more geogrids of smaller aperture sizes were also selected to assess effects of geogrid opening size on rutting behavior as well as any potential scale effects associated with the smaller specimen size. In total, five geosynthetics were used to study their interaction and influence on specimen behavior.

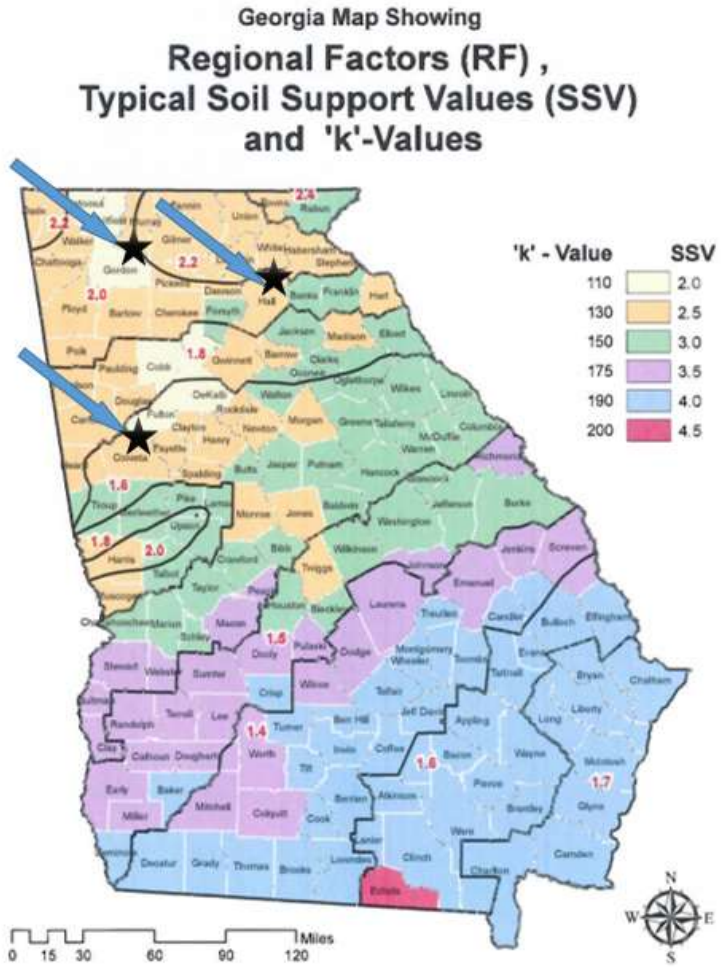

Figure 4-1 - Locations of subgrade soils investigated

Rutting tests were conducted with all three subgrade soils for optimum and higher water content conditions to simulate stiff subgrade (CBR>10) and soft subgrade (CBR<2.5) conditions in the tests. Effects of stabilization was assessed using the unstabilized case as control specimen, and then including the five geosynthetics for the same testing conditions. The geosynthetic was placed at the interface of the base and subgrade layers in all tests. The performance of the pavement specimens were assessed using two performance criteria, namely, surface rutting and stress changes in the subgrade.

4.2 Material Physical Properties

A series of tests were conducted to characterize the geomaterials used in the testing program, to determine properties like gradation, Atterberg limits, Proctor density and CBR values for the soil materials and the tensile properties of the smaller-aperture geogrids. These results are presented below.

4.2.1 Subgrade Soil & GAB

4.2.1.1 Grain Size Distribution and Atterberg Limits

The grain size distribution curves for the three subgrade soils were determined using the moist-sieving process as per ASTM D6913 and ASTM D1140, which are ideal for plastic soils with high fines content. The particle size curves, as shown in Figure 4-2 (a), indicate that the soils are very similar in composition. The GAB material was slightly modified for the bench-scale testing by scalping aggregate particles larger than 3/8-inch (9.5 mm) and compensated with additional particles of size between No.4 sieve-size and 3/8 inch (4.76 and 9.5 mm). The original and modified curves are shown in Figure 4-2 (b).

This was done to ensure minimal boundary effects with lateral walls of the chamber, which measures 8 inches (203 mm) in width.

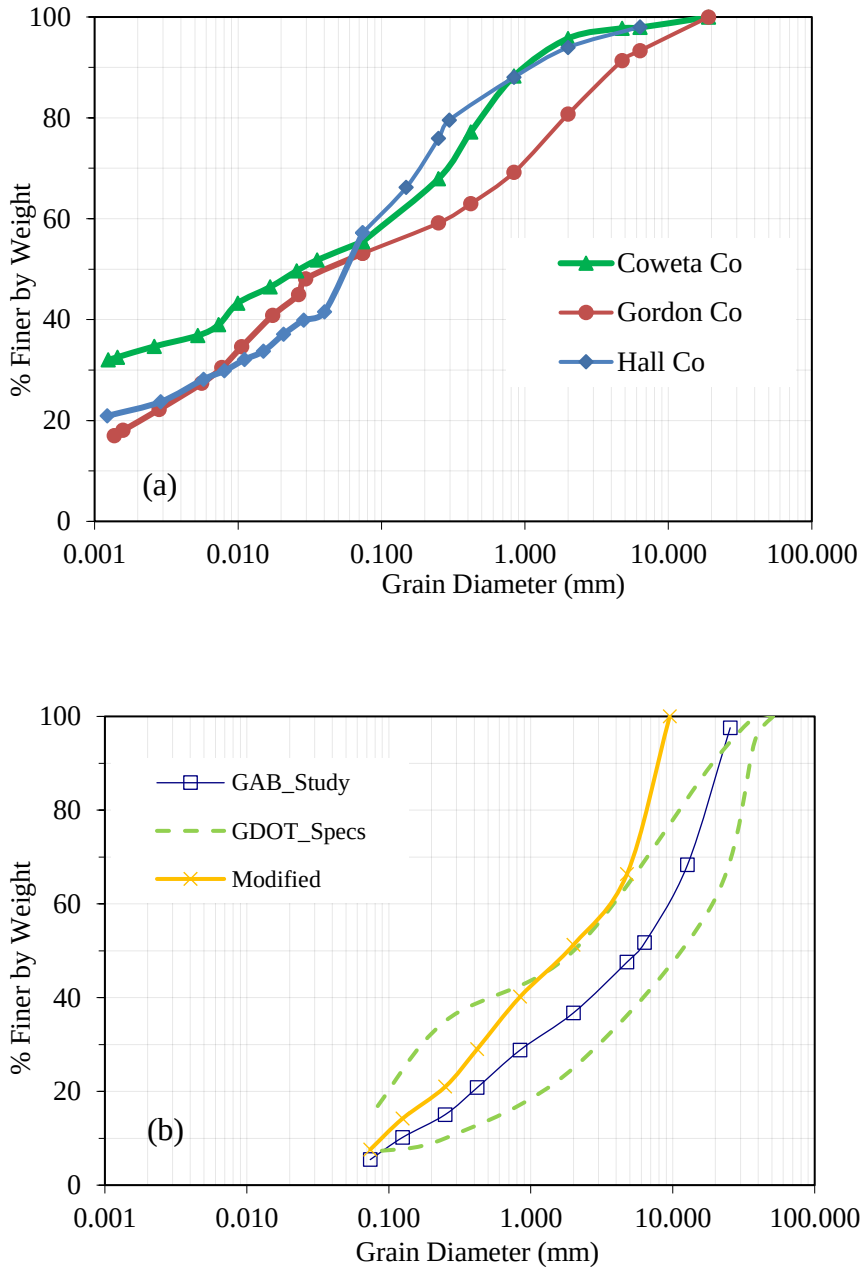

Figure 4-2 - Particle Size Distribution Chart of Materials

The Atterberg limits testing procedure is defined in ASTM D4318-17, the Standard Test Methods for Liquid Limit, Plastic Limit, and Plasticity Index of Soils. These tests were performed on each type of soil among other soil characterization tests and are summarized in Table 4-1.

Table 4-1 - Subgrade and aggregate properties

	Coweta Co	Gordon Co	Hall Co	GAB
USCS Classification	MH	MH	MH	GW
Percentage fines	55.5	53.1	57.2	5.5
Plastic Limit	41.0	41.7	37.4	-
Liquid Limit	63.5	63.4	57.1	-
Plasticity Index	22.5	21.7	19.7	-
Max Dry Density (pcf)	113.0	107.0	114.0	133.5
Optimum Water Content	16.5	17.5	15.0	7.2
CBR @ optimum w.c.	19.4	14.4	17.1	26.3
CBR @ 26% w.c.	4.1	5.5	3.6	-

4.2.2 Geosynthetics

Five geosynthetic products including four geogrids and one geotextile were used in the bench-scale study. In addition to the commercially available Tensar BX1200 geogrid (GG1000) and Tencate Mirafi HP270 geotextile (GT), three additional geogrids of smaller aperture sizes were selected to assess effects of geogrid opening size on rutting behavior. These geogrids are polyethylene grid manufactured by Industrial Netting, Inc. The tensile properties of the three new geogrids, referred to as GG500, GG250 and GG125 with opening sizes 0.5 inch, 0.25 inch and 0.125 inch respectively, were estimated using multi-

rib tensile tests (ASTM D6637). It is worth noting that all these geogrids exhibit opening sizes that are larger than the mean particle size of the modified GAB (D50) of 0.08 inches (2 mm), which is a typically accepted rule of thumb in practice as necessary for particle penetration and therefore, effective interlocking. In addition, the thickness of the geosynthetic and the tensile stiffness are properties that are known to influence to aggregate-geosynthetic interaction and are important for pavement design in practice. A summary of properties of the geosynthetics used is presented in Table 4-2.

Table 4-2 - Geogrid Specifications

(* indicates values supplied by manufacturer)

		GG1000*	GG500	GG250	GG125	GT*
Opening size, inch (mm)		1.0 (25.4)	0.5 (12.7)	0.25 (6.35)	0.125 (3.18)	0.024 (0.6)
Minimum rib thickness, inch (mm)		0.05 (1.27)	0.08 (1.95)	0.05 (1.30)	0.03 (0.74)	-
Tensile Strength @ 2% strain lb/ft (kN/m)	MD	410 (6.0)	292 (4.26)	209 (3.05)	132 (1.93)	-
	XMD	620 (9.0)	347 (5.06)	249 (3.63)	163 (2.38)	-
Tensile Strength @ 5% strain lb/ft (kN/m)	MD	810 (11.8)	402 (5.87)	286 (4.18)	169 (2.46)	1274 (18.6)
	XMD	1340 (19.6)	492 (7.18)	363 (5.3)	206 (3.02)	1439 (21.0)
Ultimate Tensile Strength lb/ft (kN/m)	MD	1310 (19.2)	410 (5.99)	292 (4.26)	169 (2.46)	2640 (38.5)
	XMD	1970 (28.8)	504 (7.36)	405 (5.91)	206 (3.02)	2460 (35.9)

Figure 4-3 shows specimens of all five geosynthetic materials. In terms of rib thickness, GG500 has the highest rib thickness of all the geogrids, followed by GG1000, GG250 and GG125. The stiffness of GT geotextile is almost double of the GG1000 geogrid, while the remaining three geogrids exhibit much lower stiffness values. While the GG500 and GG250 are composed of medium density polyethylene, the GG125 is composed of low-density polyethylene which explains it low stiffness. These properties of the geosynthetics could play a crucial role in their interaction with the aggregate layer and must be considered in the assessment of results from the experiments.

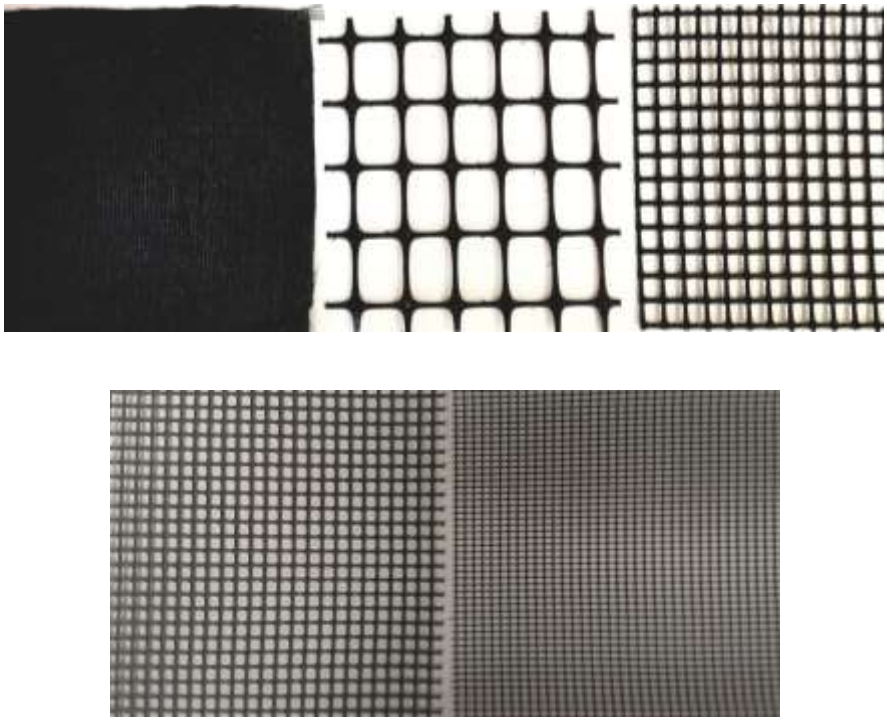

Figure 4-3 - Geosynthetics Used for Bench Scale Test

4.3 Preliminary Rutting Tests

Generally, following the development of a new laboratory testing system, it is desirable to run multiple tests at different scenarios to ascertain the functionality and validity of the procedure. If the observed behavior matches expected trends, the apparatus can then be used to meet the objectives of the study. In this study, the bench-scale procedure was first validated based on multiple tests which were used for establishing repeatability of results, comparing stress measurements in the specimen to expected values and assessing the rutting behavior for various loading stresses and stabilization. Following this, the tests comparing unstabilized and stabilized specimens were conducted. These results are presented below.

4.3.1 Typical Rutting Behaviour

The rutting curve obtained after the data processing steps described in the previous section followed a typical exponentially decreasing pattern, with majority of the deformations occurring in the initial 50 cycles and stabilizing in subsequent cycles. The typical rutting depths in the base layer at the end of the test ranged between 0.1 and 0.5 inches, which represents permanent strains of 10% to 50% of the base layer thickness. The rutting curves were in close conformance with exponential rutting model proposed by Tseng and Lytton (1989), as shown in Equation 1.

$$\epsilon_a = a.e^{-(\frac{b}{N^c})} \quad (4)$$

ϵ_a is axial permanent strain , N is number of load cycles

a, b and c are fitting parameters

(a)

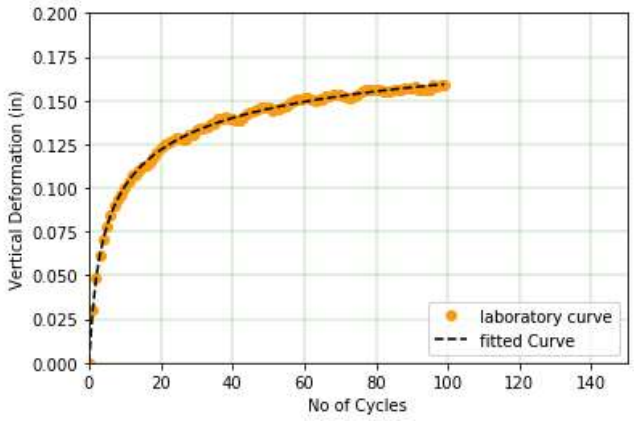

(b)

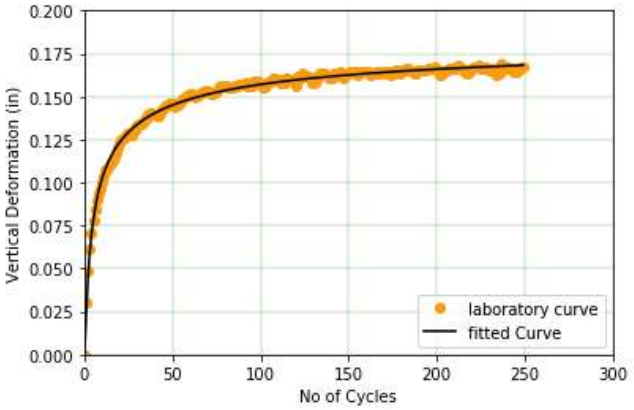

(c)

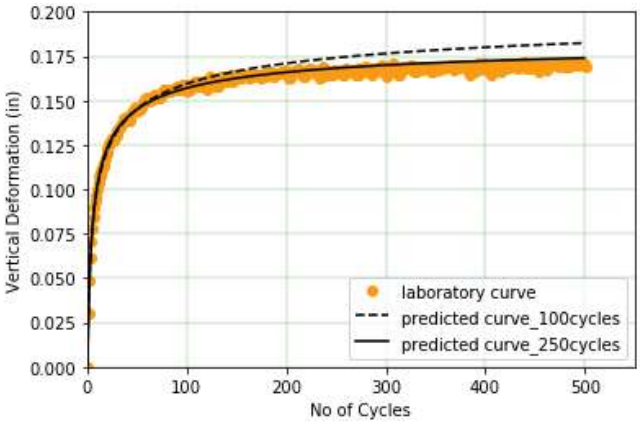

Figure 4-4 - Rutting curves fitted to exponential model for (a) first 100 loading cycles, (b) first 250 loading cycles and (c) comparison of laboratory curve over 500 cycles and predicted curves from (a) and (b)

To demonstrate the exponential nature of the rutting curves and justify 250 loading cycles for the test duration, the results from a sample test were used to form three datasets, each comprising of the first 100, 250 and 500 cycles. The first two datasets with 100 and 250 loading cycles were fitted to the rutting model shown in Equation 4, as shown in Figures 4-4 (a) and 4-4 (b). The fitted models were then extrapolated to 500 cycles and plotted along with the laboratory-obtained dataset for all 500 cycles, as shown in Figure 4-4 (c). Clearly, the predicted curve based on 100 cycles overestimates the rutting. However, there is negligible variation in the predicted curve using 250 cycles and the 500-cycle laboratory curve, thus justifying the selected test duration of 250 loading cycles.

4.3.2 Typical Stress Behaviour

While the surface rutting behavior is most commonly used to evaluate the performance of pavements, the pattern of stresses in the subgrade can also be crucial in gaining useful insights into the influence of the geosynthetics. Figure 4-5 presents a comparison of the theoretical stress distribution under a circularly loaded area (shown in Equation 2) for a surface stress of 27.6 psi, and the measured stresses at various depths under the wheel using the sensors (Boussinesq, 1885). In this figure, the depth z/R is normalized with the loading radius, which is 0.5 inches. Therefore, z/R of 2 is the bottom of base layer (top of subgrade) while z/R of 4 is at depth 1 inch below the top of subgrade. The measured stresses match reasonably closely with the expected distribution, even for the moving wheel loads.

$$p = q\left[1 - \frac{1}{\left[\left(\frac{R}{z}\right)^2 + 1\right]^{\frac{3}{2}}}\right] \quad (5)$$

where, *q=surface stress of 27.6 psi, p is vertical stress at depth z, R is radius of loading area*

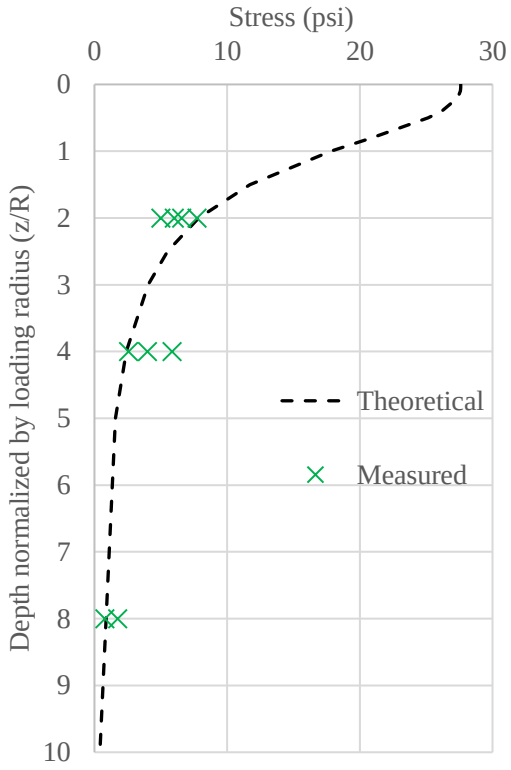

Figure 4-5 - Stress distribution below center of circularly loaded area

In addition to stress measurements under the wheel, stresses were also recorded at the wall to establish absence of boundary effects. Figure 4-6 presents test results showing sensor measurements at the top of subgrade and at the wall of the box at depth of 2 inches

below the surface. No stresses are recorded at the wall indicating no boundary effects are influencing the rutting behavior of the specimens.

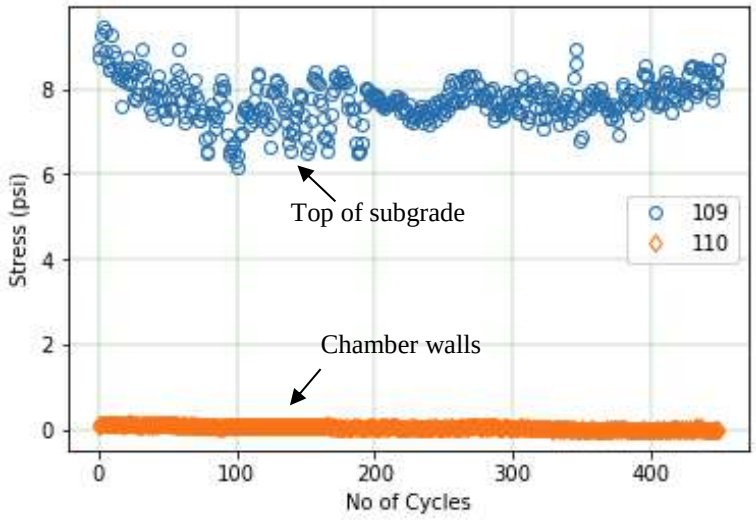

Figure 4-6 - Stress measurements made at bottom of base layer and side-wall of box

4.3.3 Repeatability of Rutting Behaviour

Multiple tests were repeated during the testing program to establish repeatability of results and gain confidence in the laboratory apparatus and procedure. A sample of these results, which includes unstabilized and stabilized cases for Gordon and Coweta subgrade soils are presented in Figure 4-7. It can be concluded that the repeated curves matched the previous trial of the tests, thus establishing repeatability.

The rutting tests shown in Figure 4-7 (b) for Coweta Co soils at 15% water content were conducted at a higher wheel stress of 38 psi (262 kPa), since these tests were part of initial iterations to identify study parameters. This explains the greater rutting compared to curves shown in Figure 4-7 (a) with Gordon Co soil at 20% water content.

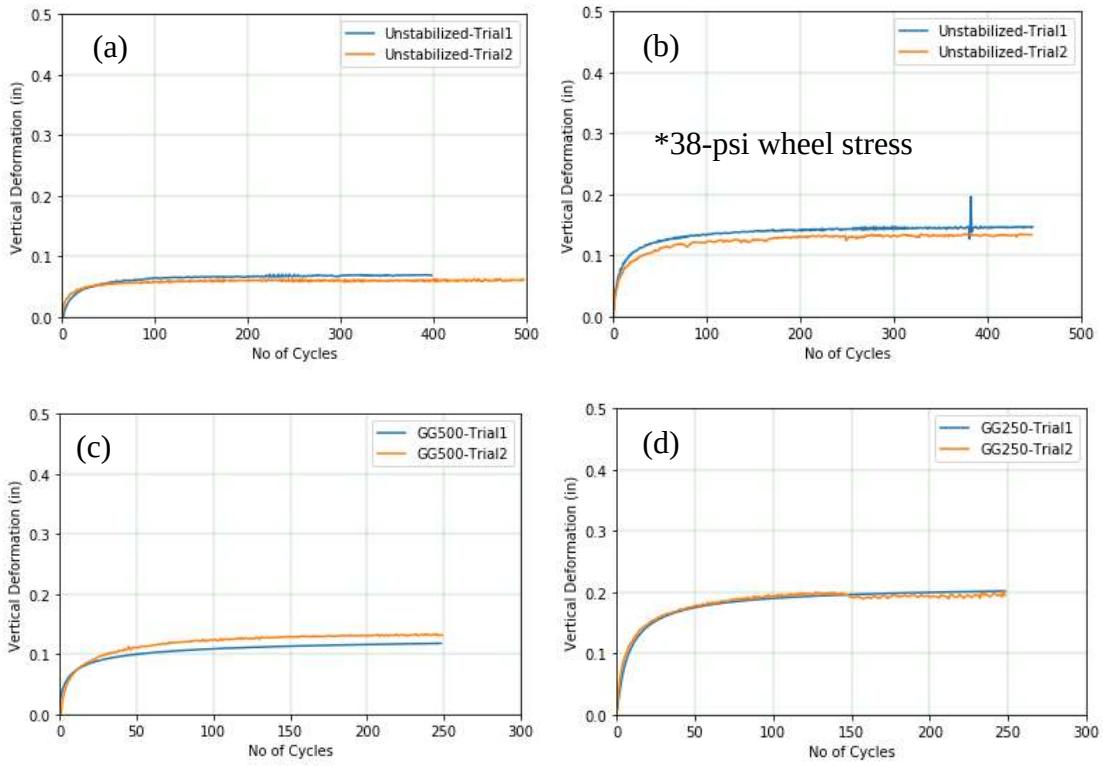

Figure 4-7 - Repeatability of rutting performance for tests with a) unstabilized specimens using Gordon co. soil at 20% water content, b) unstabilized specimens using Coweta co. soil at 15% water content, c) stabilized with geogrid GG500 over Gordon co. soil at 30% and d) stabilized with geogrid GG250 over Gordon co. soil at 30% water content

4.4 Effect of Subgrade Stiffness on Rutting Behavior

Subgrade stiffness is a critical parameter since it influences the behavior of the overlying base layer. A stiff subgrade acts as a strong foundation which provides structural support to the base layer and helps transmit traffic loads into the soil media. On the other hand, soft subgrades are prone to rutting and lack confinement due to their low stiffness. Figure 4-8 presents photographs from two sets of rutting tests conducted on a stiff and soft

Gordon Co. subgrade soil, after 300 cycles. The rut developed in the base layer over stiff subgrade (CBR>10) is significantly lower than the rut over soft subgrade (CBR<2.5).

Figure 4-8 - Photos showing rutting depths for (a) stiff and (b) soft subgrade conditions

Unstabilized rutting tests were conducted for at least two subgrade stiffness conditions for all three soils, corresponding to water contents between 15-20% and 27-33%. Two additional rutting tests were conducted with Gordon Co soil to obtain a trend of rutting behavior. The GAB material was consistent for all the tests, with 6% water content and placed at 95% relative compaction. These results are presented in Figure 4-9. As mentioned earlier, the rutting test on the Coweta Co. soil specimen at optimum water content was conducted at 38 psi as indicated in Figure 4-9 (a), all other tests were conducted at 27.6 psi.

(a)

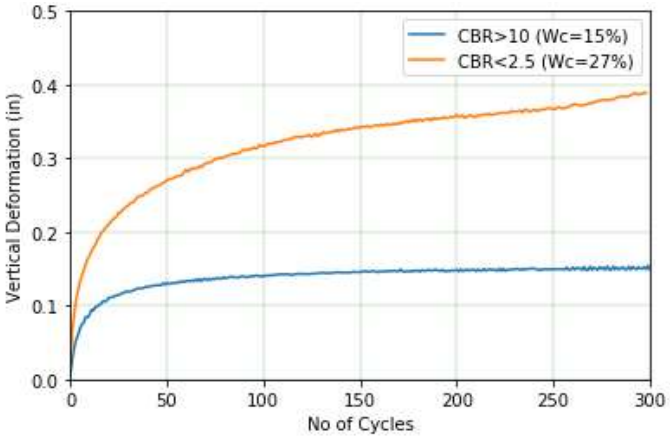

(b)

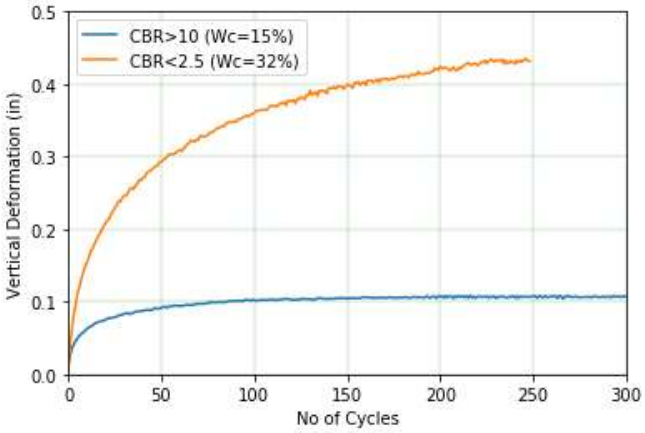

(c)

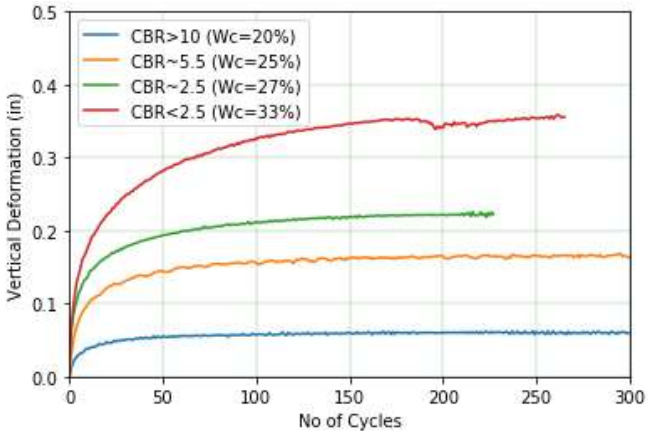

Figure 4-9 - Rutting behavior for unstabilized specimens with a) Coweta Co., b) Hall Co. and c) Gordon Co. soils at various stiffness conditions

As expected, increasing subgrade water contents results in degradation in the rutting behavior. At subgrade water contents close to optimum, the layer was stiff enough to support the base layer under the imposed traffic loads and resulted in rut depths between 0.05 to 0.15 inches after 250 loading cycles. These values of vertical permanent strains of 5-15% are below the accepted limits of 30% in practice. However, soft subgrade conditions with CBR below 2.5 were observed to result in rut depths of around 0.4 inches after 250 loading cycles, which represents a significantly high vertical strain of 40% in the base layer. This indicates a need for geosynthetic stabilization. In the case of the set of tests with Gordon Co. soils shown in Figure 4-9 (c) and Figure 4-10, the increase in rutting tendency is evident with increasing subgrade water contents (20, 25, 27 and 33%). Importantly, the steep slope of the trend line establishes the influence of subgrade water content on surface rutting in the base layer.

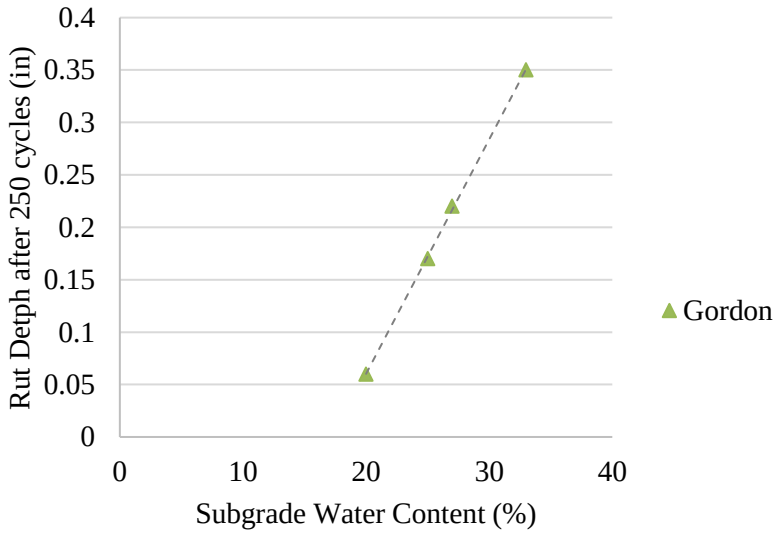

Figure 4-10 - Rut depths after 250 cycles for Gordon Co soil with no stabilization

4.5 Effect of Geosynthetic Stabilization on Rutting Behavior

Multiple studies (Barskdale, 1972, 1989, Perkins et al., 2005, Al-Qadi et al., 2008) have reported that geosynthetic stabilization shows the greatest improvement over soft subgrade soils with CBR below 2.5 or 3.0. This pattern was clear in the bench-scale rutting experiments.

4.5.1 Rutting with Stiff Subgrades at CBR>2.5

To assess the benefits of geosynthetics in stiff-subgrade conditions, rutting tests were conducted over relatively stiff subgrades with CBR of 5.0 or greater using Gordon and Hall Co soils. The Gordon Co specimen was prepared at a subgrade water content of 25% (CBR~5.5) and the Hall Co specimen was prepared at 15% water content (CBR>10). The rutting curves for each set of tests are presented in Figure 4-11, and the following observations can be made. Firstly, as noted before, the rutting for the unstabilized specimens are low with both subgrades, approximately 0.15 inches over Gordon Co subgrade and 0.1 inches over Hall Co subgrade, after 300 loading cycles. In the case of the Gordon Co subgrade (Figure 4-11a), GG500 cause a reduction in rutting while GG250 showed a higher rutting of 0.2 inches. In the case of the Hall Co subgrade (Figure 4-11b), the geogrids (GG1000, GG500, GG125) and geotextile did not show any further reduction in rutting, but instead showed a slightly greater rutting between 0.1 and 0.18 inches. The reason for this anomalous behavior can be explained as follows: In stiff granular and soil media, the particles are closely packed, which allows the stresses to be efficiently transmitted through the pavement system with minimal lateral movement of the aggregate particles. This degree of lateral spreading is not sufficient to show any benefits of

interlocking in geogrid apertures or frictional interaction with the geotextile. To the contrary, the presence of the geosynthetic material probably results in lower mobilized interface friction compared to the plain aggregate-subgrade interface.

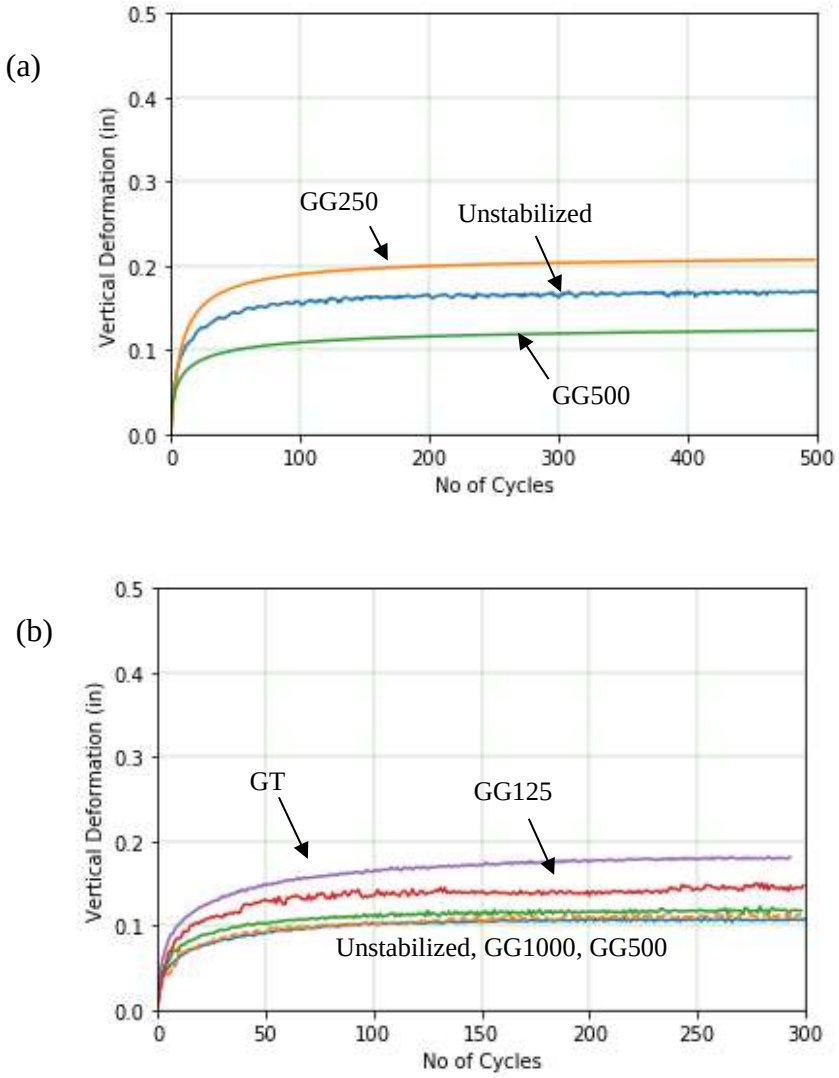

Figure 4-11 - Effect of geosynthetic stabilization on (a) Gordon and (b) Hall Co subgrades with CBR>2.5

Upon establishing the low rutting deformations over stiff subgrade and considering the focus of the bench-scale study was to establish the effectiveness of geosynthetic

stabilization over soft subgrades, further tests were conducted on wetter subgrade soils with CBR less than 2.5. These results are discussed below.

4.5.2 Rutting with Soft Subgrades at CBR<2.5

The stabilization effects of the geosynthetics were much more apparent in rutting tests over soft subgrade soils. Over soft subgrades, the larger magnitudes of rut depths induce significantly greater aggregate deformations, and the presence of a geosynthetic can be helpful in arresting these movements, as demonstrated in the following results. Figures 4-12 to 4-14 presents the rutting curves using low-stiffness (CBR<2.5) Coweta, Gordon and Hall Co subgrade soils respectively. Among the three soils at CBR<2.5, Gordon Co soil showed the least rutting of 0.35 inches after 250 loading cycles, followed by Hall Co and Coweta Co soils which showed 0.43 inches and 0.48 inches respectively. While the unstabilized rutting is significantly greater compared to stiff subgrade condition, geosynthetic stabilization reduces the rutting by 15 - 40 % after 300 loading cycles for all three subgrade cases. This is a significant improvement and emphasizes the effectiveness of stabilization. There are some variations in the relative influences of the geosynthetics in the three subgrade cases, which probably is due to a combination of factors including variations in soil properties and testing water contents.

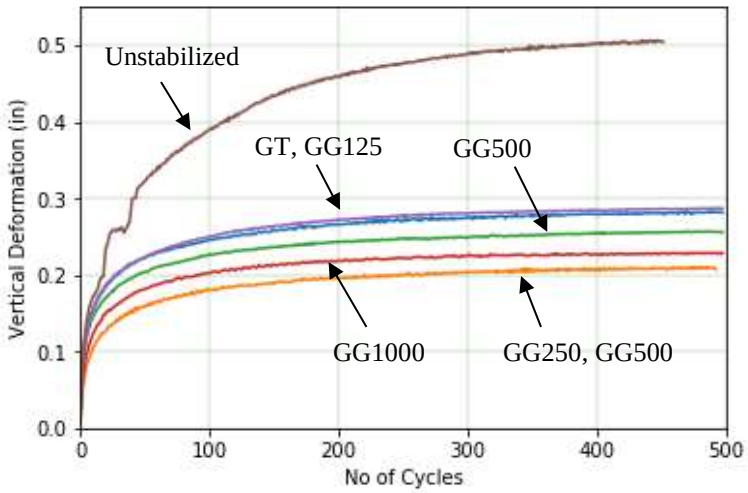

Figure 4-12 - Effect of geosynthetic stabilization on soft Coweta Co. subgrade at 27% water content

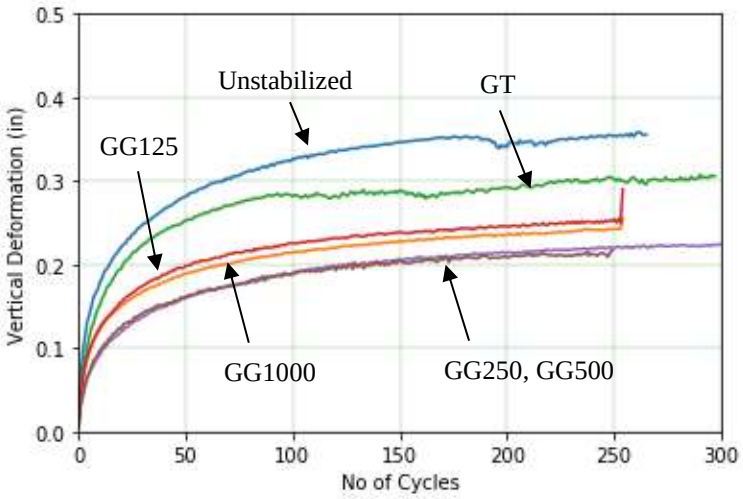

Figure 4-13 - Effect of geosynthetic stabilization on soft Gordon Co. subgrade at 32% water content

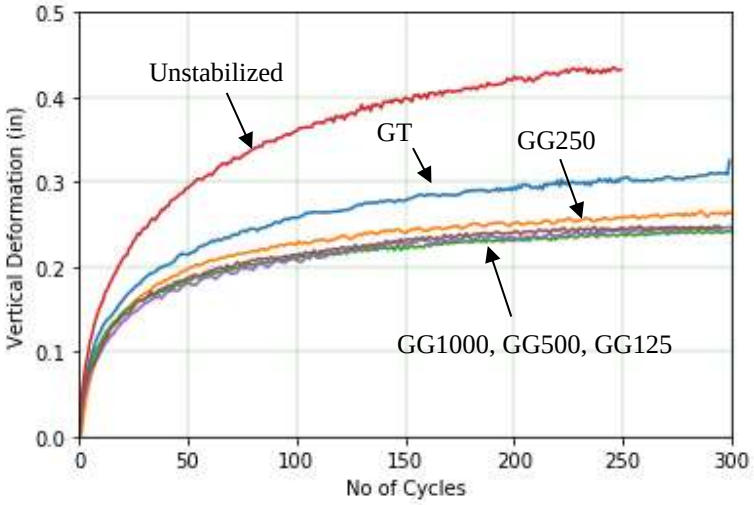

Figure 4-14 - Effect of geosynthetic stabilization on soft Hall Co. subgrade at 32% water content

As stated before, the performance of the geosynthetics are a function of a multitude factors including interaction mechanism, geometry, rib thickness and tensile stiffness. Owing to this fact, it is difficult to attribute the rutting depths to a specific parameter. Figures 4-12 through 4-14 clearly demonstrates the difference in mechanisms of aggregate-geogrid and aggregate-geotextile interactions, based on the consistent superior performance of the geogrids compared to the geotextile. The interlocking of aggregates achieved with geogrids is clearly more efficient than the solely frictional resistance that is mobilized with the geotextile, even though the geotextile has the higher tensile strengths among all geosynthetics. Meanwhile, the geotextile was extremely efficient in separating the aggregate and subgrade layers, while the intermixing was observed with the geogrid-stabilized specimens. This benefit of geotextiles may become significant over a longer timeframe over which the migration of fines might become an issue.

The other useful observation is based on the performance of the commercially available GG1000 and the three scaled down geogrids. GG1000 and GG500 are comparable in terms of the 2% tensile strength and rib thicknesses and are fairly close to each other in the rutting performance in all three subgrade-cases. Secondly, GG250 shows an equally good or improved rutting reduction behavior despite its relatively inferior tensile properties. This indicates that these geogrids fall within the range of optimal opening size for highest interlocking with the aggregate particles. Lastly, the performance of GG125, which is the least stiff of the five geosynthetics used in the study, is comparable to the other geogrids and geotextile based on the rutting curves in Figures 4-12 through 4-14. However, as presented in the subsequent section, stress measurements in the subgrade showed that this product was not as effective as the others.

4.6 Stress Distribution in Subgrade

The stabilizing potential of geosynthetics were assessed in terms of their influence on stress variations in the subgrade.

4.6.1 Effect of Subgrade Stiffness

The rutting curves over stiff subgrade were similar for both stabilized and unstabilized tests. Figure 4-15 presents stresses measured during the test in an unstabilized specimen (Figure 4-15a) and a GG250-stabilized specimen (Figure 4-15b) over Gordon Co subgrade at 20% water content (CBR > 10). Each subplot presents stress measurements made at the surface of subgrade and at a depth of 1 inch below the surface of the subgrade. The latter set of measurements inside the subgrade should clearly reflect the influence of the overlying geosynthetic, if present.

The mean stresses in the case of the unstabilized rutting test were 8 psi at the top of subgrade and 2.6 psi at a depth of 1 inch below the top of subgrade (Figure 4-15a). The corresponding values in the case of the GG250-stablized rutting test were 7 psi and 2 psi respectively (Figure 4-15b). The corresponding rut curves are very similar for the two test cases, as seen in Figure 4-15(c). Although it is expected that the impact of geogrid is going to be minimal in stiff subgrade conditions, the slight reduction in stress is an encouraging sign. The pattern of stress reduction at the top of subgrade seen in Figure 4-15 (b) presents an interesting insight. A hypothesis is that with increasing loading cycles, the particles in the loading zone are rearranging to a more stable configuration in relation to the surrounding particles as well as grid apertures, resulting in an improved lateral distribution of the vertical loads. The change in vertical stresses correlates with the change in rutting displacement shown in Figure 4-15 (c).

a)

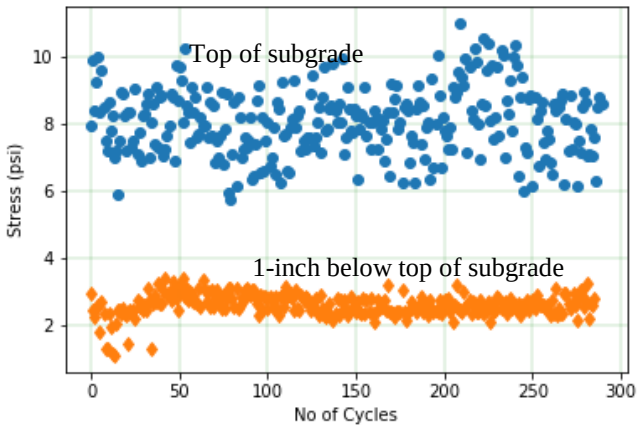

b)

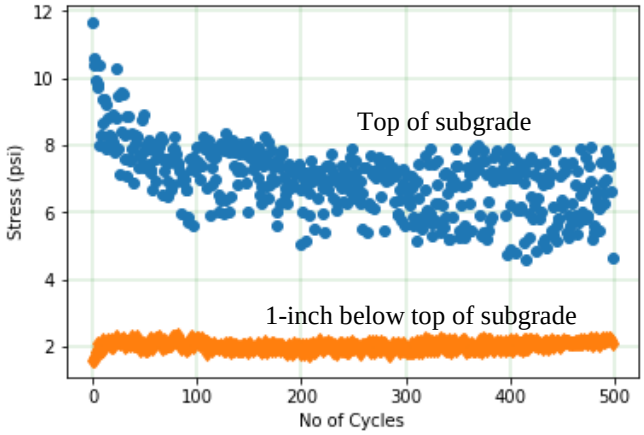

c)

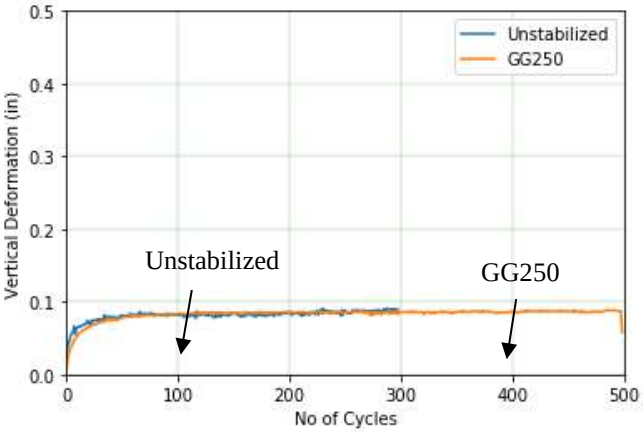

Figure 4-15 - Stress measurements in a) unstabilized and b) GG250 stabilized specimens with stiff Gordon Co subgrade and c) corresponding rutting curves

Figure 4-16 shows stress measurements made in the Gordon Co subgrade layer for various unstabilized and stabilized scenarios. The top-of-subgrade stresses vary initially and stabilize between 4-6 psi in all cases. Most of the tests with geogrids show a similar pattern with top-of-subgrade stress as was seen in Figure 4-15. The stresses either decreases over the first 50 cycles or stay stable. In comparison, the unstabilized specimen shows an increase in stresses. This clearly illustrates the load distribution capability of geogrids.

Moreover, the stress measured at depth 1 inch below the surface of subgrade, also shows different behaviour for the unstabilized and stabilized cases. As seen in Figure 4-16 (a), the stresses measured inside the subgrade increases to 4 psi at the end of 300 cycles of loading. This indicates deterioration of the base layer, leading to higher stresses being transmitted to the subgrade as the test progresses. Meanwhile, all other subplots in Figures 4-16 (b) to (f) except Figure 4-16 (e) show significantly lower magnitudes of stresses, of about 2 psi being experienced in the subgrade. This observation clearly demonstrates that the geosynthetics jare able to distribute the traffic loads laterally, which is crucial in maintaining the structural integrity of the pavement.

However, Figure 4-16 (e) shows a different behaviour compared to the other geosynthetic cases. In Figure 4-13, the rutting curve corresponding to GG125 lies between the remaining geogrids and the unstabilized case. However, Figure 4-16 (e) shows the top-of-subgrade stresses to be increase as the test progresses and thus, not efficiently distributing the loads laterally. Interestingly, this observation is supported by the measurements of subgrade rutting, which were typically made after completion of a rutting test. The aggregate layer was first exhumed and rut depths were recorded by manually placing a ruler horizontally across the subgrade surface and measuring the depth of the

centre point under the wheel path using callipers. The subgrade rut was recorded at three locations along the wheel path to get an accurate estimate of subgrade rutting. The values of subgrade rutting for the tests corresponding to Figures 4-16 (a) through (f) were 0.231 (unstabilized), 0.153 (GG1000), 0.099 (GG500), 0.099 (GG250), 0.157 (GG125) and 0.184 (GT) inches respectively. As stated before, the GG125 is the lowest stiffness material of all the geosynthetics. The above-stated observations regarding the lack of load distribution and increased subgrade rutting with the GG125 could be caused by its low stiffness, which led to a tensioned-membrane effect that was supporting the load rather than aggregate interlocking.

Another observation along similar lines concerns the results with GT-stabilized test results. Even though the rutting with the GT-case is higher than all the geogrid-stabilized cases, the stresses are comparatively smaller as seen in Figure 4-16 (f). Again, this could be caused by the high stiffness of the geotextile, which distributes the load to a larger area over the subgrade. Therefore, in spite of the high surface and subgrade rutting, the stress experienced over the stress sensor is smaller.

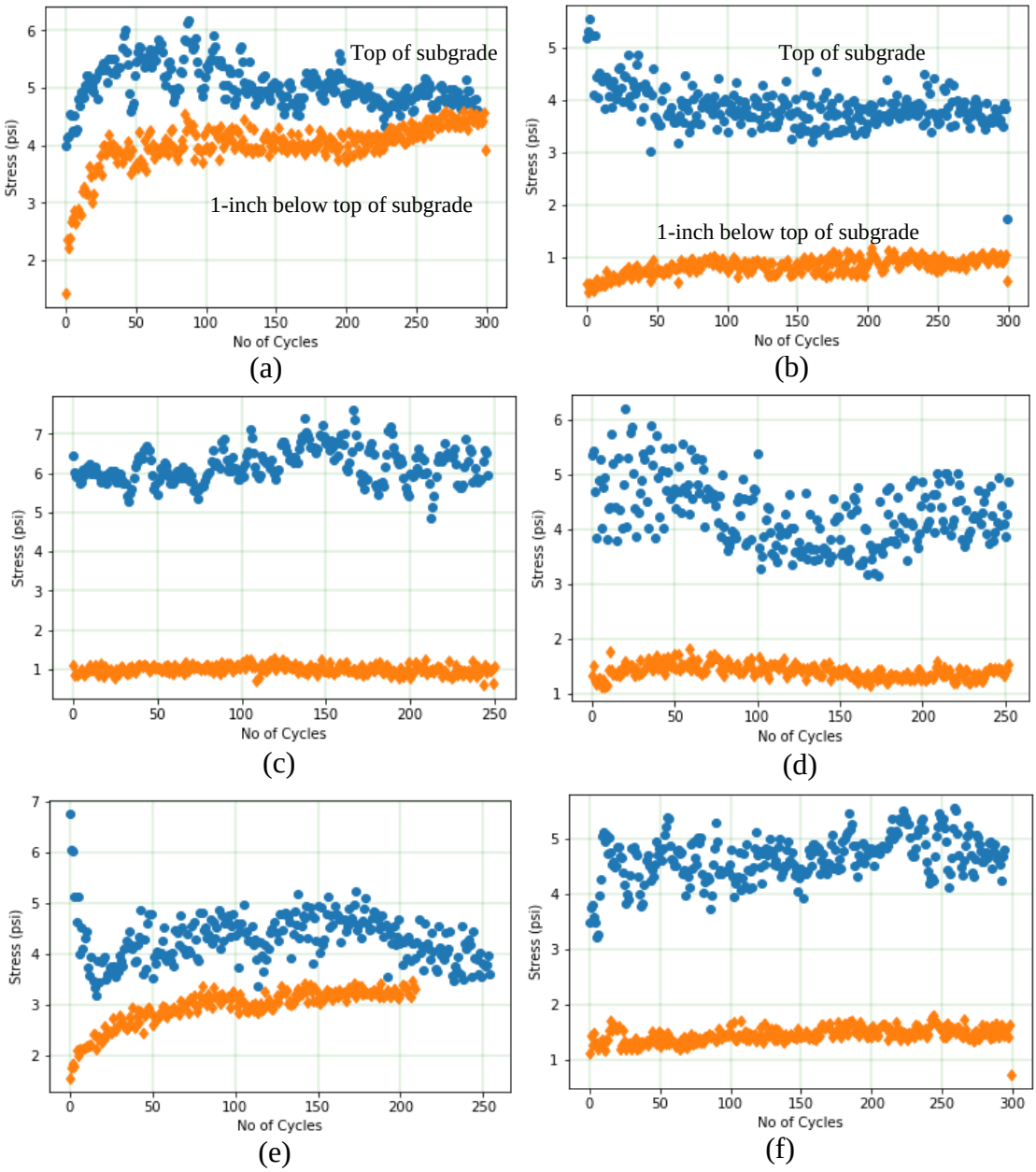

Figure 4-16 - Stress variation in top 1 inch of subgrade for a) unstabilized case and the stabilized cases with b) GG1000, c) GG500 and d) GG250, e) GG125 and f) GT

A clear variation in the stress measurements were observed at low and high subgrade stiffness's. Figure 4-17 presents the mean stresses measured in Gordon Co subgrade over a range of stiffness conditions, including subgrade water contents of 20%

(Figure 4-17a), 25% (Figure 4-17b), 27% (Figure 4-17c) and 32% water content (Figure 4-17 d-e). In each subplot in Figure 4-17, a comparison has been presented between measurements from unstabilized and stabilized cases, at both locations in the specimen, i.e., top of subgrade and 1 inch below the top of the subgrade. Figure 4-17 (e) presents the same comparison using geogrids GG500, GG250 and G125. The following observations can be made from Figure 4-17.

- Comparing the unstabilized cases in Figures 4-17 (a) through (d), the effect of subgrade stiffness can be observed. At 20% water content (Figure 4-17a), there is a significant drop of 6 psi in measured stresses from top of subgrade to one-inch below the top of subgrade. However, at greater water contents (Figure 4-17 b-d) this gap is reduced to about 1 psi or lower. These observations match expected behavior relating to high stiffness and low stiffness subgrade soils.
- The effect of inclusion of geosynthetic is also clearly observed from these plots. In Figure 4-17(a) in stiff subgrade conditions, the stabilized test shows slightly lower stress values than the unstabilized test, and more generally, follows the pattern of shown by the unstabilized test. This is similar to the observations made with the rutting curves, where the effect of stabilization on the rutting curves was negligible. Even at greater subgrade water contents (Figure 4-17 b-d), the stresses measured in stabilized case at top of subgrade is still generally slightly lower than the unstabilized case. However, the influence of the geosynthetic can be witnessed by the significant difference in the values recorded 1-inch into the subgrade. As

stated earlier, in the unstabilized tests at higher water contents (Figures 4-17 b-d), the gap in the stress magnitudes from top of subgrade to 1 inch below is greatly reduced. The stress measured 1-inch below the top of subgrade is very close to the measurement at the top of subgrade, due to the inability of the soft soil to distribute the applied load. On the other hand, the stabilized tests exhibit a much lower stress inside the subgrade compared to the unstabilized test measurements. This shows that the geosynthetics are able to distribute the loads laterally, and thereby reduce the intensity of the stress that is transmitted into the subgrade.

In summary, the geosynthetics are significantly more influential in stabilizing soft soils, which is the trend that was observed in the case of the surface rutting depth measurements. Figure 4-17(e) shows a comparison of the performance of the GG500 and GG250, which are stiff geogrids and GG125 which exhibits the least stiffness. In fact, GG125 can also be torn by hand, which gives a sense of its low stiffness. As explained earlier in Figure 4-17(e), the low stiffness of GG125 causes higher stress being transmitted into the subgrade, while the GG1000 as well as GT shows remarkably improved performance.

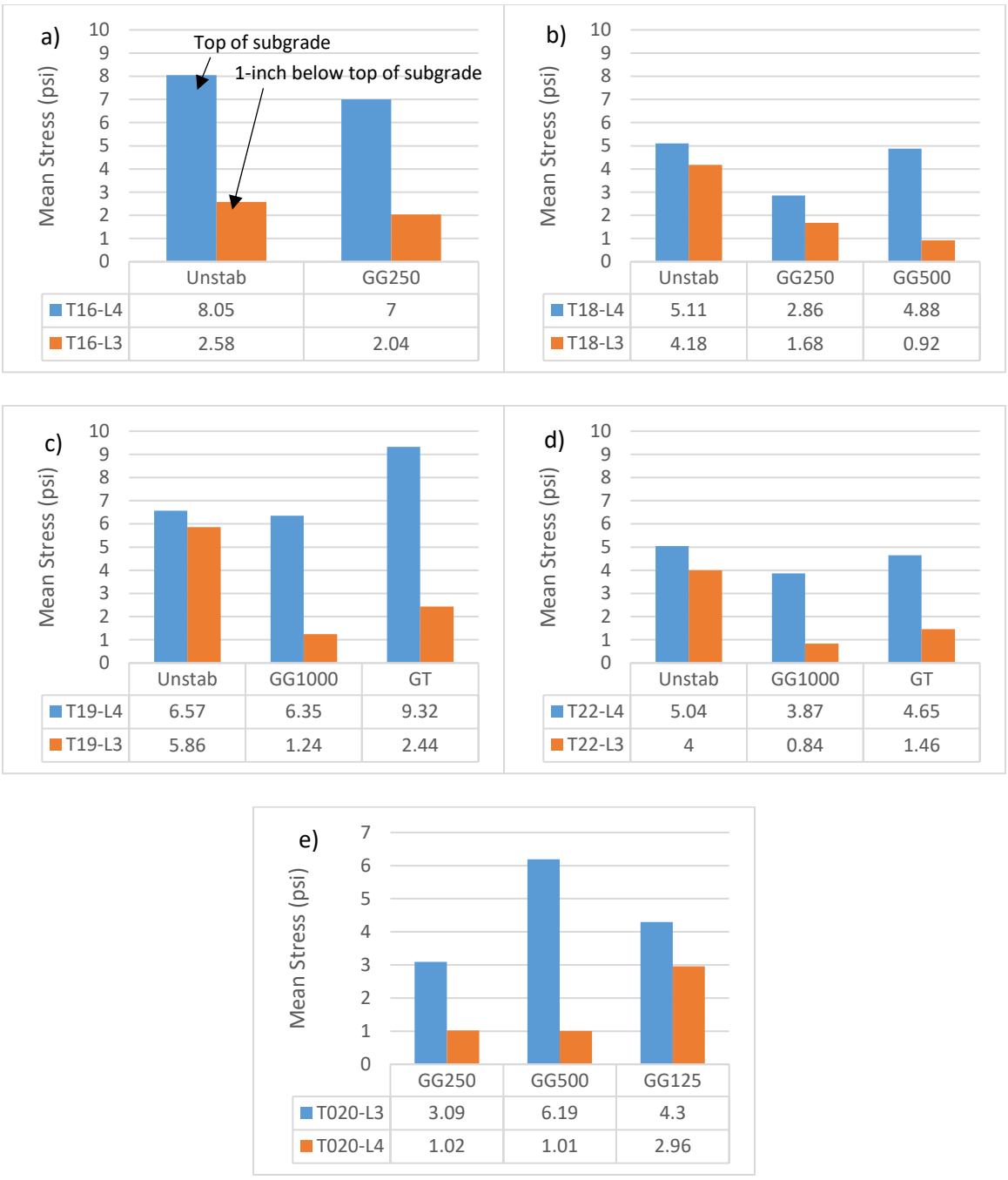

Figure 4-17 - Mean stress measured for various scenarios of stabilization using Gordon Co subgrade at water contents of a) 20%, b) 25%, c) 27%, d) and e) at 32%

4.7 Estimation of Equivalent Modulus of Geosynthetic-stabilized back-calculated from rutting deformations

By now, it is clear that stabilization of the base layer effectively increases the stiffness of the layer, thereby reducing surface deformation as well as reducing stresses transmitted to the subgrade. As stated previously Chapter 2, road design procedures are lacking a means to incorporate the effect of the geosynthetic directly into the framework. This is because, the resilient modulus is an important input in design procedures, which not only involves a complicated experimental procedure itself but also is difficult to include geosynthetics in the test specimens. As an alternative, the stabilized base layer is treated as an unstabilized layer with a greater modulus.

It is not uncommon for such indirect techniques to be employed to estimate resilient modulus. For example, resilient modulus can be estimated from field tests like Falling-Weight Deflectometer (FWD) tests, or using material properties like CBR and undrained shear strength. However, for techniques that depend on measuring the elastic deformation from impact forces like the FWD, studies have shown their application on geogrid-stabilized pavements do not produce accurate results. This is because although the geogrid is creating a higher-stiffness layer through confinement, it also increases the elastic rebound during unloading because of mobilized tension forces in its ribs. This results in underestimating the effective resilient modulus because of the greater resilient strains (Sun, 2017). Moreover, using laboratory techniques like the cyclic triaxial tests present challenges in terms of accurate representation of mechanisms involving geogrids in the small-sized cylindrical samples. As mentioned, resilient moduli of the individual materials are not indicative of field performance of the layered system. In this regard, back-

calculation of resilient modulus from permanent deformation behavior of the full system is a better-suited technique to capture the effects of geogrid-aggregate interaction and performance

4.7.1 Soil Damage Model

Sun et al. (2017) presented a back-calculation technique for estimating resilient modulus of the individual layers from permanent deformation at the top of base course and subgrade using laboratory plate-load test data. The technique was based on the MEPDG permanent deformation model, also known as the soil damage model and was originally proposed by Tseng and Lytton (1989) as presented in Equation 6. This model was calibrated with the data from the long-term pavement performance (LTTP) program and adopted in the current MEPDG (AASHTO 2008) as follows.

Soil damage model to estimate permanent deformation

$$\begin{cases} PD = k \cdot h_{\text{soil}} \cdot \varepsilon_v \cdot \left(\dfrac{\varepsilon_0}{\varepsilon_r}\right) \cdot e^{-\left(\frac{\rho}{N}\right)^{\beta}} \\ Log\beta = -0.61119 - 0.017638 W_c \\ \rho = 10^9 \cdot \left(\dfrac{-4.89285}{1-(10^9)^{\beta}}\right)^{\frac{1}{\beta}} \\ \left(\dfrac{\varepsilon_0}{\varepsilon_r}\right) = \dfrac{0.15 \cdot e^{\rho^{\beta}} + 20 \cdot e^{\left(\frac{\rho}{10^9}\right)^{\beta}}}{2} \end{cases} \quad (6)$$

where, PD is the permanent deformation of the soil layer, h_{soil} is layer thickness, k is the calibration factor, 1.67 for full pavements, Wc is the water content (%) and N is the number of loading cycles. The other variables are the same as the ones in Equation 1 (Chapter 2).

In the following section, a procedure to back-calculate the equivalent resilient modulus of the stabilized layered system from the surface permanent deformation behavior is presented. The technique employs a similar model as the soil damage model shown above, with the modification of treating the layered system as one composite layer. This allows for a comparison of the various factors studied in this chapter, like subgrade water content, stabilization, applied wheel stress and loading cycles. Additionally, since the modulus is scale-independent, it allows for estimation as well as to check the validity of the rutting data.

4.7.2 Composite Resilient Modulus for Gordon County Soils at different subgrade CBR

Consider the set of rutting tests conducted on Gordon county soil at different CBR values (<2.5, 2.5, 5.5 and >10) and no stabilization, shown as solid lines in Figure 4-18. Table 4-3 summarizes the set of four tests and associated subgrade water contents.

Table 4-3 - Gordon county tests at different CBR

Subgrade water content	Subgrade CBR	Dev Stress, kPa (psi)
20%	14	187.5 (27.2)
25%	5.5	
27%	2.5	
33%	1.5	

The following steps were carried out in sequence to estimate the composite resilient moduli.

- Estimate calibration factor k = 0.019 * σ_d (σ_d in kPa). This is a modified calibration factor for the bench-scale system. The AASHTO value is 1.67, and does not include a stress component since the stress was considered to be the standard equivalent single-axle truck load of 18000-lbs.
- Estimate β and ρ and $\varepsilon_0/\ \varepsilon_r$ as a function of water content as per the equations shown above
- Start with an initial estimate of Mr and estimate the PD. Iterate using different back-calculated modulus values until the estimated permanent deformation matches the measured permanent deformation as shown below.

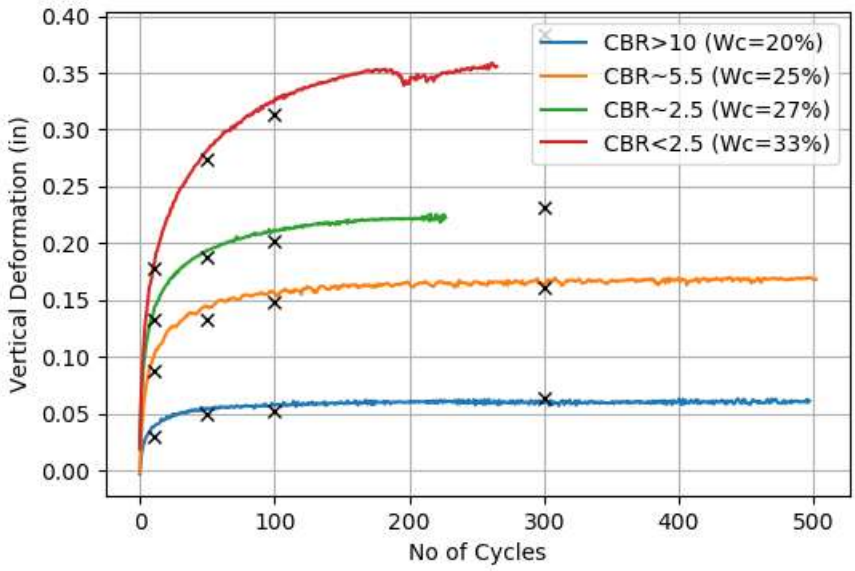

Figure 4-18 - Gordon Co rutting tests at different CBR's (crosses represent predicted rutting estimated at N=10, 50, 100, 300)

The estimated composite moduli are presented in Table 4-4. The moduli generally increase with loading repetitions and then stabilize (Figure 4-19). Additionally, when near

the optimum water content of the subgrade (high CBR), the moduli range in the 200-400 MPa range, while at low subgrade CBR, it ranges between 30-100 MPa. These values can be compared with the typical Mr values based on USCS classification presented in Table 4-5 (FHWA Geotechnical Aspects of Pavements Reference Manual). It can be observed that at high subgrade CBR, the composite moduli matches that of the typical base-layer gravel material, while at low subgrade CBR, it is heavily influenced by the subgrade.

It is worth re-noting that this is a composite moduli of the base course-subgrade combination in the upper two inches of the specimen. The moduli can be estimated for the base layer only as well, by following a similar procedure, if the fraction of total deformation that is solely from the base layer is known.

Table 4-4 - Estimated composite resilient moduli

	N=10	N=50	N=100	N=200
SG wc	Estimated Mr (Mpa)			
20	200	280	320	350
25	60	95	105	120
27	38	65	75	82
33	25	40	44	46

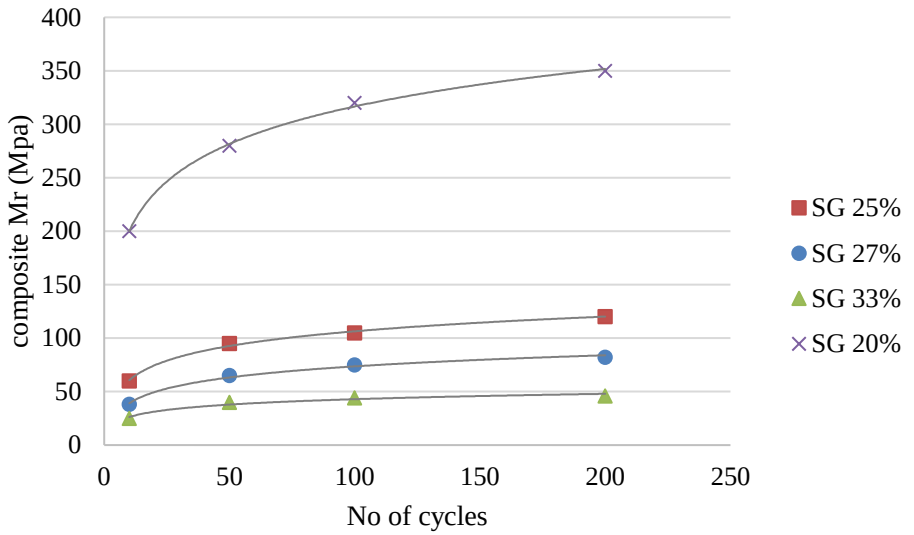

Figure 4-19 - Variation of M_r with loading cycles

Another approach is to estimate the CBR from the moduli using commonly used correlations like the one below used in AASHTO (1993).

$$Mr = 17.6\ CBR^{0.64}\ (MPa) \qquad (7)$$

The estimated CBR using this equation is N=10 loading cycles is 45, 7, 3.3 and 1.7 for the four cases presented in Table 4-4 respectively. These values are comparable to the test-based values.

Table 4-5 - Default M_R values for unbound granular and subgrade materials at un-soaked optimum moisture content and density conditions (NCHRP 1-37A, 2004).

Material Classification	*MR Range (psi)**	Typical MR (psi)	Typical MR (MPa)
USCS Soil Class			
GW	39,500 - 42,000	41,000	283
GP	35,500 - 40,000	38,000	262
GM	33,000 - 42,000	38,500	266
GC	24,000 - 37,500	31,000	214
GW-GM	35,500 - 40,500	38,500	266
GP-GM	31,000 - 40,000	36,000	248
GW-GC	28,000 - 40,000	34,500	238
GP-GC	28,000 - 39,000	34,000	235
SW	28,000 - 37,500	32,000	221
SP	24,000 - 33,000	28,000	193
SM	28,000 - 37,500	32,000	221
SC	21,500 - 28,000	24,000	166
SW-SM	24,000 - 33,000	28,000	193
SP-SM	24,000 - 33,000	28,000	193
SW-SC	21,500 - 31,000	25,500	176
SP-SC	21,500 - 31,000	25,500	176
ML	17,000 - 25,500	20,000	138
CL	13,500 - 24,000	17,000	117
MH	8,000 - 17,500	11,500	79
CH	5,000 - 13,500	8,000	55

4.7.3 Coweta Co at different stresses

In the previous section, the back calculation procedure was applied to Gordon county subgrade at different CBR values. In this section, the Coweta county tests at different stresses are considered. Similar steps are followed, while also using the same calibration factor (k = 0.019 * σ_d (σ_d in kPa)). Table 4-6 summarizes the set of three tests and associated applied stresses. This serves as a check to the robustness of the procedure.

Since the subgrade CBR was 1.4, the estimated resilient modulus value was expected to lie in the 20-50 MPa range as observed in the previous section. Inserting these values in the equation and iterating, i.e. by using values of 30, 42, 42 and 44 MPa at 10, 50, 200 and 450 loading cycles respectively, a close match is observed as shown in Figure 4-20.

Table 4-6 - Coweta county tests at different loading stresses

SG w.c.	SG CBR	Dev Stress, kPa (psi)
27 %	1.4	187.5 (27.2)
		110 (16)
		67 (9.6)

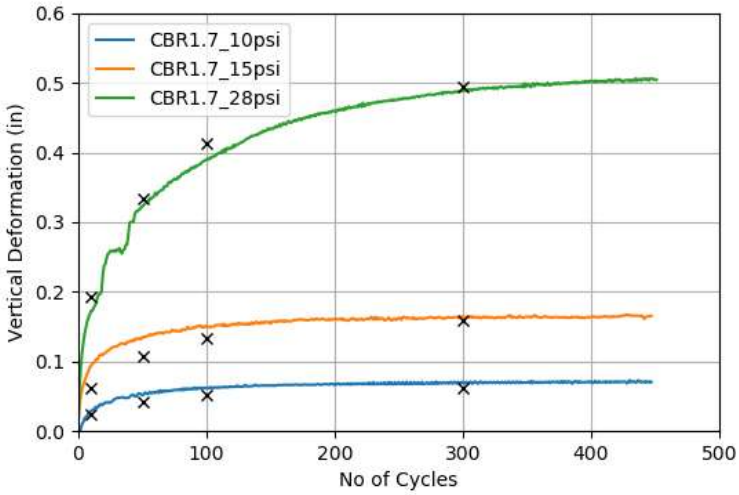

Figure 4-20 - Coweta Co rutting tests and estimated rutting using back-calculated composite resilient moduli

4.7.4 Evaluation of geosynthetic benefits

Now, by conducting the same analysis on unstabilized and stabilized rutting tests, the effect of presence of geosynthetics can be quantified in terms of the modulus. The Modulus Improvement Factor (MIF), defined as shown below can be estimated.

$$MIF = \frac{E_{stabilized}}{E_{unstabilized}} \quad (8)$$

Figures 4-21 and 4-22 present predicted and measured rutting deformations using the back-calculated moduli and the MIF for geogrid and geotextile stabilized tests respectively. As expected from the rutting results, the geogrid shower higher MIF values, of about 1.5 compared to 1.75 achieved with the geotextile.

In summary, this back-calculation is useful, and should be tested more rigorously with resilient modulus tests for the same materials. It presents a very quick procedure to obtain resilient modulus values from existing and easy-to-collect permanent deformation data. This information can be used in design of roads, comparing different geosynthetic products and comparing lab-testing results to field-testing results.

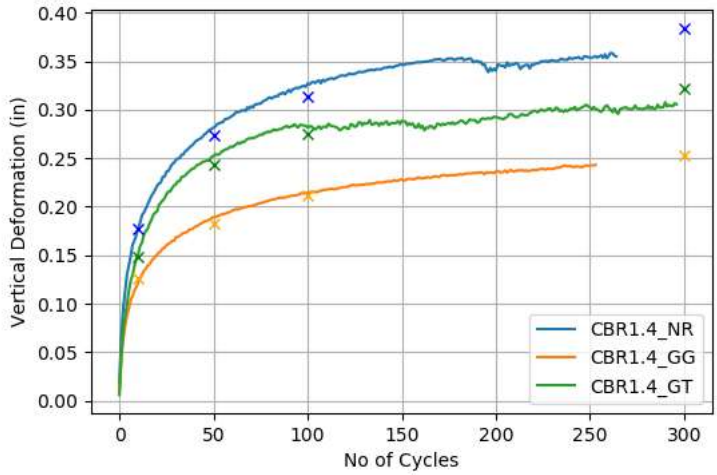

Figure 4-21 - Gordon Co rutting tests at CBR 1.4 and different stabilization conditions

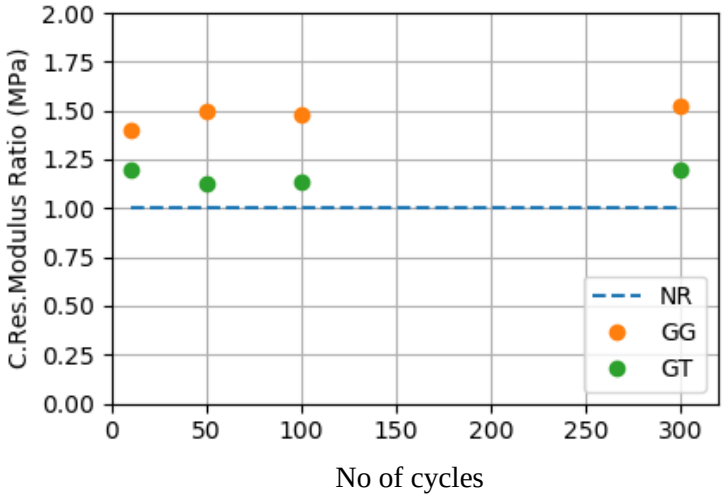

Figure 4-22 - Ratio of stabilized to unstabilized composite moduli for N=10, 50, 100, 300

CHAPTER 5. EFFECT OF PARTICLE SHAPE ON INTERLOCKING WITH STEEL AND POLYMER GEOGRIDS

The previous chapter showed that geosynthetics, especially polymeric geogrids, significantly improve the performance of pavement systems in soft subgrade conditions, and the rutting test apparatus provides a standardized test methodology for assessing their performance. To build on this knowledge and further achieve a strong fundamental understanding of the interaction behavior of aggregate-geogrid systems, a systematic investigation of the influencing factors is required. The focus of this chapter is the role of grid opening size, grid location in the base layer and aggregate morphology on unbound aggregate base layer stabilization in pavement systems. For this purpose, a series of rutting tests were conducted using four biaxial steel grids and three biaxial polymer geogrids of different opening sizes. The two aggregate materials were of similar particle size distribution but with different morphological properties.

In order to focus on aggregate-grid interaction, some of the other influencing variables were removed as follows: all rutting tests were performed over the same stiff subgrade, and the two aggregate materials comprised of uniformly-sized particles (0.25 inch - 0.375 inch or 6.35 mm - 9.5 mm). A narrow range for the particle size was chosen to avoid influence of grading on rutting behavior. Thus, the observed rutting behavior can provide insights into the significance of aggregate-grid mechanisms such as lateral spreading and interlocking within the grid apertures.

The effect of grid opening size was studied by using steel grids and polymer geogrids of opening sizes ranging from 0.25 inch (6.35 mm) to 1 inch (25.4 mm). The effect of grid stiffness were also evaluated using these results. The effect of grid location was studied by placing these grids at various locations in the aggregate layer, i.e., bottom, two-thirds and one-third the layer thickness from the surface. The effect of particle morphology was studied, by comparing the performance of the two aggregate materials which exhibit vastly different morphologies. The first material comprised of round and smooth particles, referred to as rounded aggregate (RA) and the second material comprised of angular and rough particles, referred to as quarry aggregate (QA). In addition, a third material was prepared by mixing the two individual aggregates in an equal proportion to assess the rutting behavior of the mixture. These sets of test parameter combinations permits a systematic assessment of aggregate-grid interlocking mechanisms as discussed in this chapter.

5.1 Materials

5.1.1 Aggregates

The three aggregate materials, rounded aggregate (RA), quarry aggregate (QA) and a mixture of the two referred to as rounded-quarry aggregate (RQA), are shown in Figure 5-1. All three aggregates are classified as poorly graded materials as per Unified Soil Classification System (USCS) with particle sizes ranging between 0.25 in. (6.5 mm) and 0.375 in. (9.5 mm) in diameter. The properties of each material are presented in Table 5-1.

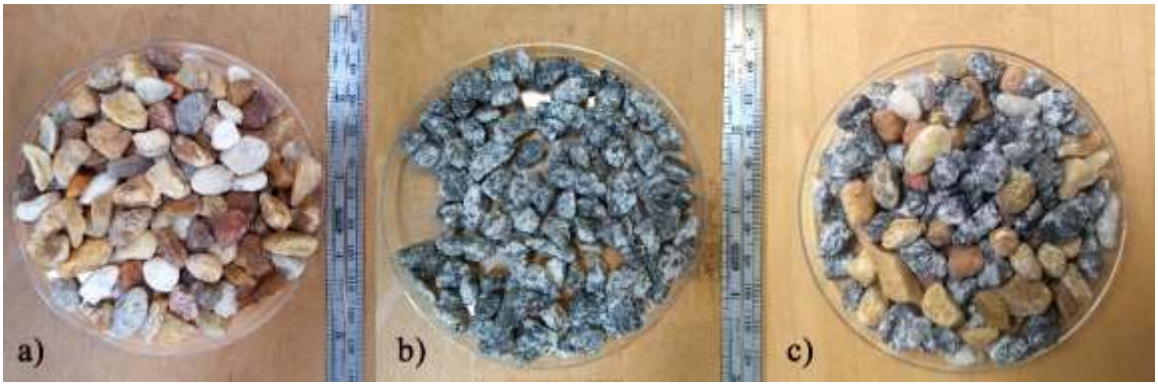

Figure 5-1 - Aggregate materials used in this study (a) river aggregate (b) quarry aggregate (c) river-quarry aggregate

Table 5-1 - Summary of material characteristics

Material ID	RA	QA	RQA
USCS Classification	GP	GP	GP
D_{10}, *in (mm)*	0.236 (6)	0.236 (6)	0.236 (6)
D_{30}, *in (mm)*	0.276 (7)	0.276 (7)	0.276 (7)
D_{50}, *in (mm)*	0.291 (7.4)	0.299 (7.6)	0.295 (7.5)
D_{60}, *in (mm)*	0.315 (8)	0.315 (8)	0.315 (8)
C_u	1.33	1.33	1.33
C_c	1.02	1.02	1.02
Angle of Repose, °	30.2	34.8	32.8
e_{max}	0.753	0.940	0.796
e_{min}	0.540	0.775	0.636

5.1.2 Steel Grids

Four inextensible welded-wire steel grids, SG1, SG2, SG3 and SG4 were selected for this study, with varying square-shaped openings and rib thicknesses as presented in

Table 5-2. These opening sizes span across the minimum and maximum particle size of the aggregates, which are 0.25 inches (6.35 mm) and 0.375 inches (9.5 mm).

Table 5-2 Steel grid properties

Steel Grid	Aperture Size, in. (mm)	Rib Thickness, in. (mm)
SG1	0.25 (6.35)	0.020 (0.50)
SG2	0.50 (12.7)	0.032 (0.815)
SG3	0.75 (19.05)	0.069 (1.76)
SG4	1.00 (25.4)	0.055 (1.4)

5.1.3 Polymer Geogrids

The three geogrids, GG1000, GG500 and GG250 that are used in this study are the same as ones discussed in Chapter 4. Their opening sizes are 1 inch (25.4 mm), 0.5 inch (12.7 mm) and 0.25 inch (6.35 mm) respectively. In comparison to the steel grids which are welded wires in orthogonal directions in two planes, these geogrids are punched and drawn from polypropylene or polyethylene sheets in a single plane. The difference in the rib structure and stiffness could potentially have an influence on the rutting behaviour but represents their different manufacturing processes.

5.2 Testing Procedure

The sequence of sample preparation and testing is as follows. The subgrade system consisting of a soil layer of 4 inches (100 mm) thickness was compacted at optimum water content and 90% of the maximum dry density, and a 0.06-inch (1.5 mm) thick aluminum sheet was placed over the soil layer. The purpose of the aluminum sheet was to serve as a

semi-rigid smooth platform and thus, eliminate any effects of aggregate contamination, subgrade rutting or interface friction on the overlying base layer. A two-inch thick aggregate layer was placed over the subgrade system, and densified appropriately by hand tamping over a wooden block. This thickness of the aggregate layer was chosen so that the influence of the grid was evident in rutting deformations while also accommodating several particle diameters across the layer. The relative density of the aggregate layer was maintained at 60±10% for all tests, by using the same quantity of material, compaction effort and measuring the layer thickness. A 0.125-inch rubber membrane sheet was placed over the aggregate layer to provide a stable loading surface for the wheel and prevent aggregate waving. The specimens were tested using a constant loading stress of 5 psi applied by the rolling wheel. This magnitude of stress was chosen to induce` relatively gradual and distinct rutting formations in the base layers, which allowed the comparison of effects of aggregate type and grid stabilization. A schematic of a typical specimen cross-section is shown in Figure 5-2.

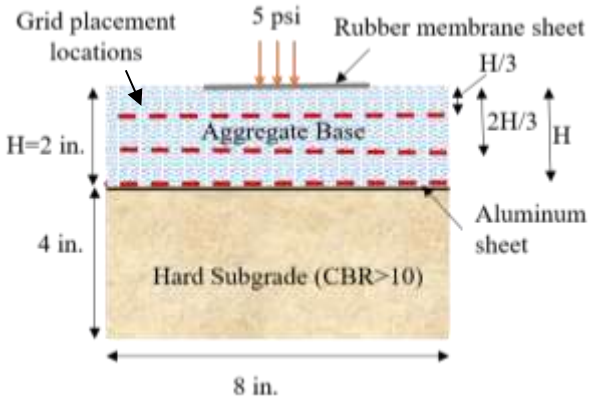

Figure 5-2 Typical specimen cross-section showing various grid locations

5.3 Experimental Program

The testing program was conducted in two stages. In the first stage of the study, rutting tests were conducted with all combinations of the four steel grids (SG1, SG2, SG3 and SG4), three geogrids (GG1000, GG500 and GG250) and both the aggregate materials (RA and QA). For combinations of each aggregate material with steel grids, the rutting performance was assessed at three grid-locations, namely, at the bottom, two-third and one-third thickness of the base layer. For tests with geogrids, the rutting performance was assessed at the lower two grid-locations, namely, at the bottom and two-third thickness of the base layer. These tests enable a systematic understanding of the effects of grid location and grid opening size on the surface rutting behavior of the stabilized-aggregate system. In the second stage, additional rutting tests were conducted on the RQA material, which represents an intermediate aggregate material based on particle morphology, using the SG2 grid. The purpose of these tests was to assess the relationship of particle shape on the rutting behavior, using the RA, QA and the RQA mixture.

5.4 Results

The rutting tests were conducted up to 35 loading cycles for most of the experiments, typically resulting in rut depths ranging between 0.2 inches (5 mm) and 0.5 inches (12.7 mm) at the end of the test. The rutting curves obtained can be represented by exponential rutting model proposed by Tseng and Lytton (1989) as shown in Equation 1.

$$\epsilon = A \,.\, e^{\frac{-B}{N^C}} \tag{9}$$

where, ϵ is the total permanent deformation, N is the number of loading cycles, and A, B and C are model fitting parameters

As an example, Figure 5-3 illustrates the close match obtained between the laboratory-measured rutting curve and the fitted-curve using the aforementioned rutting model, for the test with the unstabilized QA material. As is typical of exponential curves, the rate of accumulation of vertical displacement was initially high followed by gradual stabilization as the test progressed. The high degree of rutting observed in the tests in the study can be attributed to the poorly-graded nature of the aggregate materials used, which hinders the material's ability to form a stiff closely-packed matrix thereby increasing susceptibility to rutting deformations. It is also worth mentioning that 35 loading cycles were sufficient to observe distinct trends in the rutting behavior corresponding to the test-specific condition, indicating the effect of stabilization provided by grids. For tests with excessive deformation and thus terminated prior to completion of 35 loading cycles, the collected data was fit to the above rutting model and then extrapolated to 35 loading cycles. This enabled a comparative analysis of the ultimate rutting depths at the end of 35 loading cycles across all tests.

5.4.1 Repeatability of results

Several tests in the testing program were repeated to confirm observed trends as well as to establish repeatability of test results with the rutting apparatus. Figure 5-4 presents two sample sets of tests that were repeated for the same set of testing conditions, namely the unstabilized RA material and the QA material stabilized with the SG4 grid at

depth 2H/3. A close match in the rutting response of the test specimens was obtained which confirms the repeatability of the test results.

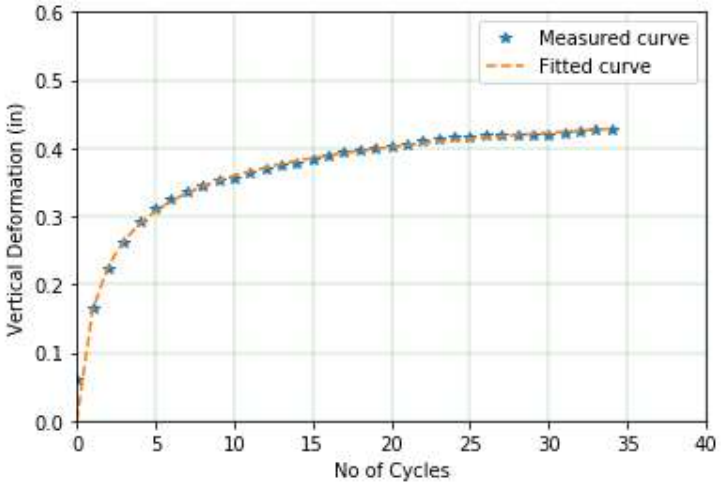

Figure 5-3 - Example showing a close-fit of rutting model to laboratory data obtained with unstabilized test with the QA material

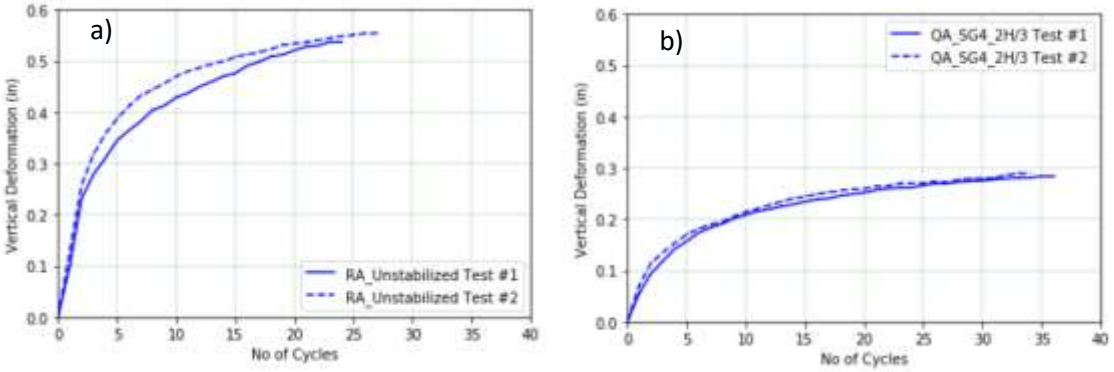

Figure 5-4 - Sample experimental test results for a) unstabilized RA and b) QA stabilized with grid-SG4 at depth 2H/3 cases to show repeatability of rutting test apparatus

The following sections present a detailed analysis of the observed rutting behavior from the following standpoints, i.e., effects of grid stabilization, grid location in the base layer, grid opening size and particle morphology.

5.4.2 Rutting Tests using Steel Grids

This section presents the results and discussion for tests involving steel grids, while Section 5.4.3 presents the corresponding results for geogrids.

5.4.2.1 Effect of Grid Location

Figures 5-5 and 5-6 present the measured rutting response of RA and QA materials respectively, with unstabilized and stabilized tests using the four grids (SG1, SG2, SG3 and SG4). Each subplot in the figures represents an aggregate-grid combination and contains four rutting curves, namely, the unstabilized test and tests with three different grid locations in the base layer (at depths H, 2H/3 and H/3). A few tests shown in Figure 5-5 involving the RA material were stopped short of 35 loading cycles owing to excessive surface rutting.

In general, a reduction in rutting is observed with grid stabilization for both materials. The exception to this observation in seen in Figures 5.5(a), 5-5(b) and 5-5(d), where the rutting performance of the RA-base layer is similar when unstabilized or stabilized with corresponding grids placed at depth H. This behavior can be reasonably explained using the following conceptual framework. When an unbound aggregate layer is loaded using a rolling wheel, the particles directly under the wheel are first densified vertically and immediately afterward begin to spread laterally, creating ruts at the surface

(Barksdale, 1989). However, when a grid is introduced in this layer, the particles in its vicinity are interlocked in the apertures, consequently becoming restricted to displace laterally. In addition to this grid-aggregate interaction component, the particles surrounding the interlocked particles also experience some, albeit reduced, degree of lateral restraint owing to inter-particle interlocking and interface friction. Therefore, a zone of increased confinement and consequently increased stiffness is created around the grid. Figures 5-5(a), 5-5(b) and 5-5(d) indicates that for these combinations of aggregate and grid locations, the zone of confinement is not extending to the surface to have any effect on the particles close to the surface of the base layer. In Figure 5-5(c), however, the curve for grid SG3 placed at depth H shows a deviation from unstabilized curve after 5 loading cycles, potentially indicating an improved interaction with aggregate layer compared to other grids and will be elaborated in later sections.

In contrast, the QA material shows an immediate reduction in rutting from unstabilized case to stabilization at depth H with all grids (Figure 5-6). Thus, the grid-induced confinement at the bottom of the base layer complemented with the greater interlocking potential of the QA material, results in reduced displacements of the particles at the surface of the base layer. This observation emphasizes the importance of aggregate morphology towards interlocking, as well as role of the grid in enhancing this interlocking. For the test combination of the QA material with grid SG1 at depth H (Figure 5-6a), the rutting at the end of 35 cycles is close to the unstabilized case, although the rate of accumulation of permanent displacement is much more gradual. This can be accounted for by the fact that the aggregate particles are larger than the opening size of SG1 (0.25 inches or 6.35 mm), and therefore unable to mobilize and sustain a well-interlocked particle

matrix. Once again, grid SG3 shows a large improvement in rutting performance even when placed at depth H as seen in Figure 5-6(c).

Amongst the stabilized tests, the location of the grid in the base layer has a significant effect on the surface rutting. For each aggregate-grid combination, the observed rutting decreased with shallow depths of grid placements. This trend is expected considering the zone of confinement is close to the surface at shallow grid-placements, and therefore the particles under the wheel can adequately transfer the wheel load to adjoining particles with minimal lateral deformation.

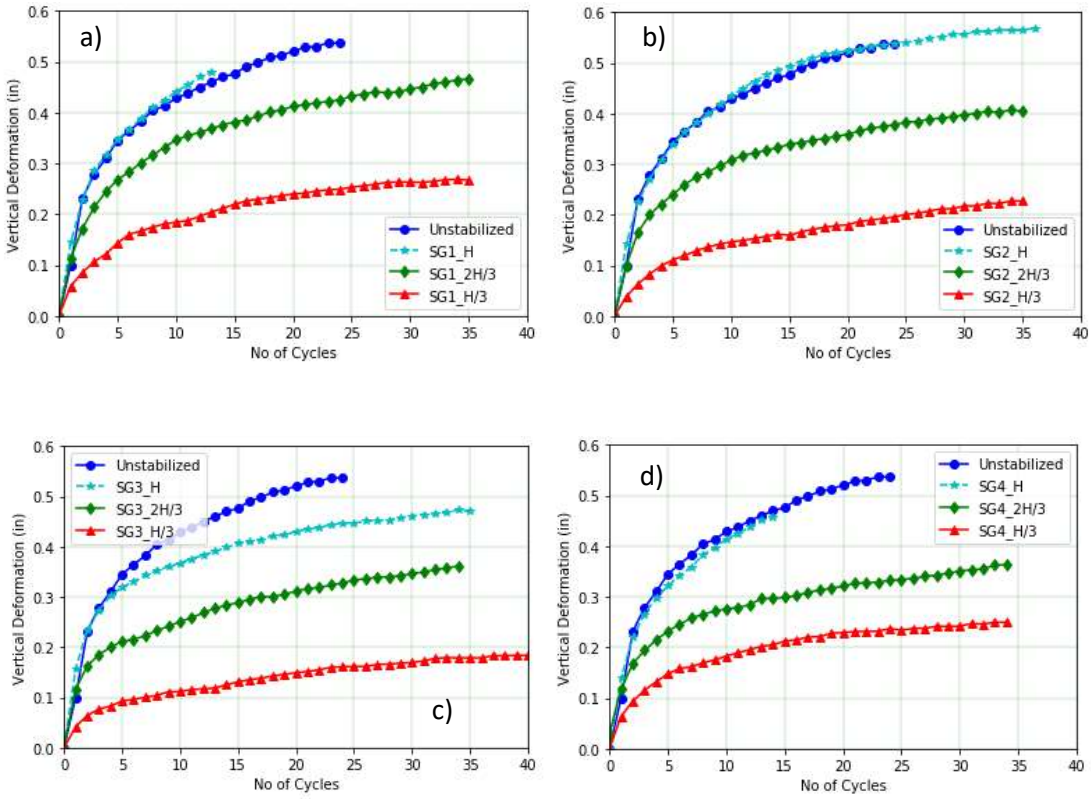

Figure 5-5 - Rutting response of RA with a) SG1, b) SG2, c) SG3 and d) SG4

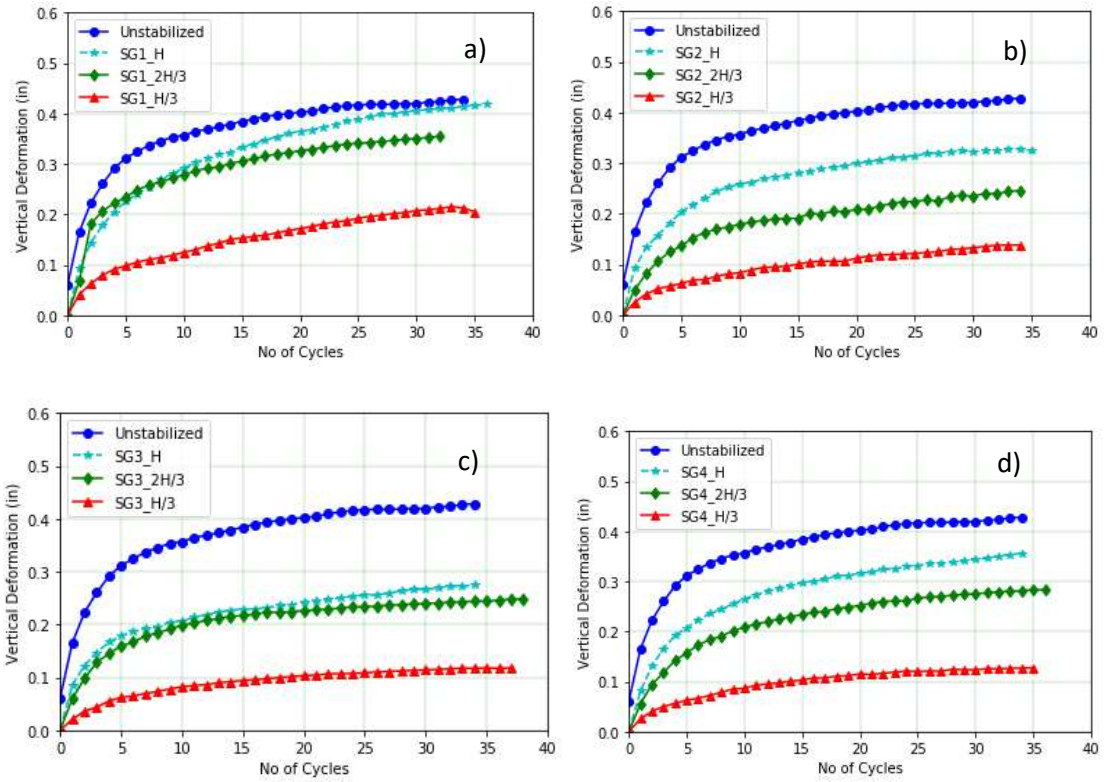

Figure 5-6 - Rutting response of QA with a) SG1, b) SG2, c) SG3 and d) SG4

5.4.2.2 Opening Size

The grid opening has a clear influence on the rutting behavior as explained below. Figure 5-7 shows the observed relationship between rutting depth at 35 loading cycles for both aggregates and the four grid opening sizes at various locations of grid placements. For the tests that were stopped short of 35 loading cycles, the rutting depth was extrapolated to 35 cycles using an exponential model (Equation 9) fitted to the data. After conducting multiple tests to confirm the observed behavior, grid SG3, with opening size of 0.75 inches (19.05 mm) clearly showed the lowest rutting for all grid-locations and both aggregates. The values of rut depths at the end of the tests decreases with increasing opening size from

0.25-inch (6.35 mm) to 0.75-inch (19.05 mm) and then slightly increases with 1-inch (25.4 mm) opening size in most cases.

This behavior indicates that SG3 has the optimal geometry to accommodate aggregate particles in its openings, facilitating a strong interlocked zone to mechanically support overlying aggregate particles. Grid SG1 with an opening size of 0.25 inch (6.35 mm) shows the highest rutting (except at location H/3), which can easily be explained by the fact that the aggregate particles are too large to even pass through its openings, and therefore their ability to interlock is minimal. This effect is clearly seen in the corresponding rutting curves in Figure 5-5(a) and 5-6(a), where the rutting curves throughout the test is much closer to the unstabilized curve than for any other grid.

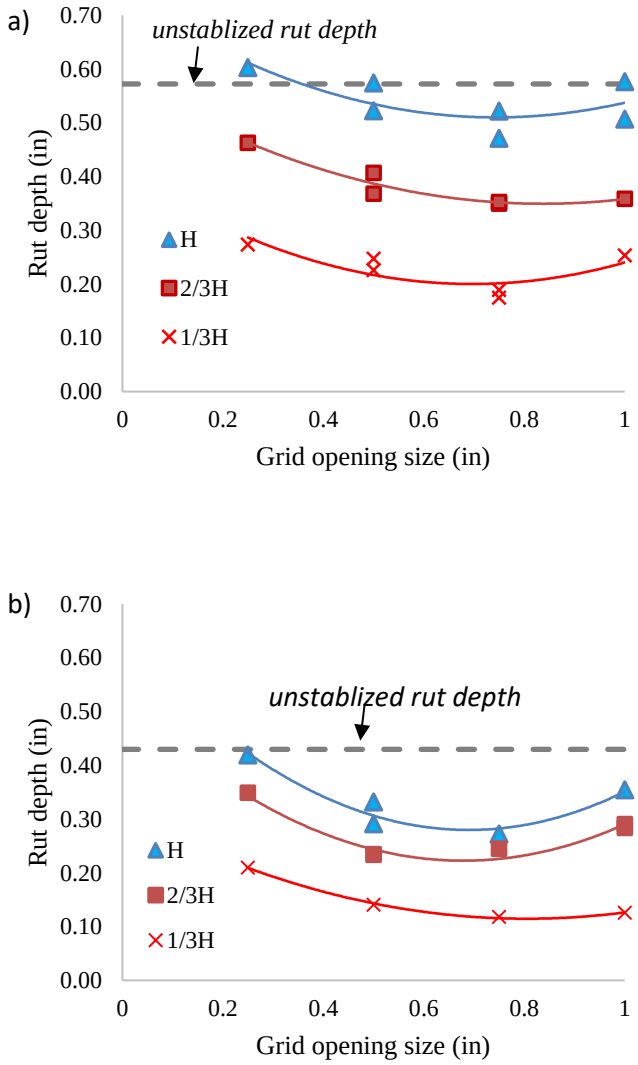

Figure 5-7 - Rutting depth for (a) RA and (b) QA materials and all four grid openings

5.4.2.3 Effect of Particle Shape

The importance of particle shape angularity and roughness is evident from the results presented above. For the unstabilized case, the rutting depths with the RA and QA materials after 35 loading cycles were 0.57 inches (14.54 mm) and 0.43 inches (10.92)

respectively, indicating that QA particles offered highest resistance to rutting deformation under wheel loading. Table 5-3 presents a summary of the rutting depths measured at 35 cycles for stabilized cases. These results clearly show that QA exhibited lower rutting depths than the RA demonstrating the benefits of low sphericity and high angularity towards mobilizing improved particle-particle and particle-grid interlocking. Conversely, the quality of interlocking diminishes with decreases in angularity and increases in the sphericity.

Table 5-3 - Summary of final rutting depths for stabilized tests

Material	Location	Rutting depths at 35 loading cycles (inch, (mm))			
		SG1	SG2	SG3	SG4
RA	H	0.603 (12.3)	0.574 (14.6)	0.471 (12.0)	0.507 (12.9)
	2H/3	0.463 (11.8)	0.368 (9.3)	0.353 (9.0)	0.321 (8.2)
	H/3	0.274 (7.0)	0.226 (5.7)	0.189 (4.8)	0.253 (6.4)
QA	H	0.419 (10.6)	0.292 (7.4)	0.272 (6.9)	0.355 (9.0)
	2H/3	0.349 (8.9)	0.233 (5.9)	0.245 (6.2)	0.291 (7.4)
	H/3	0.120 (3.1)	0.141 (3.6)	0.118 (3.0)	0.126 (3.2)

Further, to establish a quantitative measure for the difference in shape properties of the two materials, an image-based computational method proposed by Vangla et al. (2017) was used. For this purpose, a representative sample of 30 particles from the RA and QA aggregate materials were chosen and images of each particle are captured in three orthogonal directions (top, front and side view projections of particle) to get a three-dimensional estimate of shape parameters. The computational steps involved in this

method identifies corners and edges of the particles by fitting circles to the particle outline, as shown in Figure 5-8 for a representative particle from RA and QA materials. It is evident from Figure 5-8 that the RA-particle has larger diameter circles and fewer corners indicating rounded and smooth edges. In comparison, the QA-particle shows a larger number of relatively smaller-radii circles and more corners indicating high angularity and an irregular surface texture.

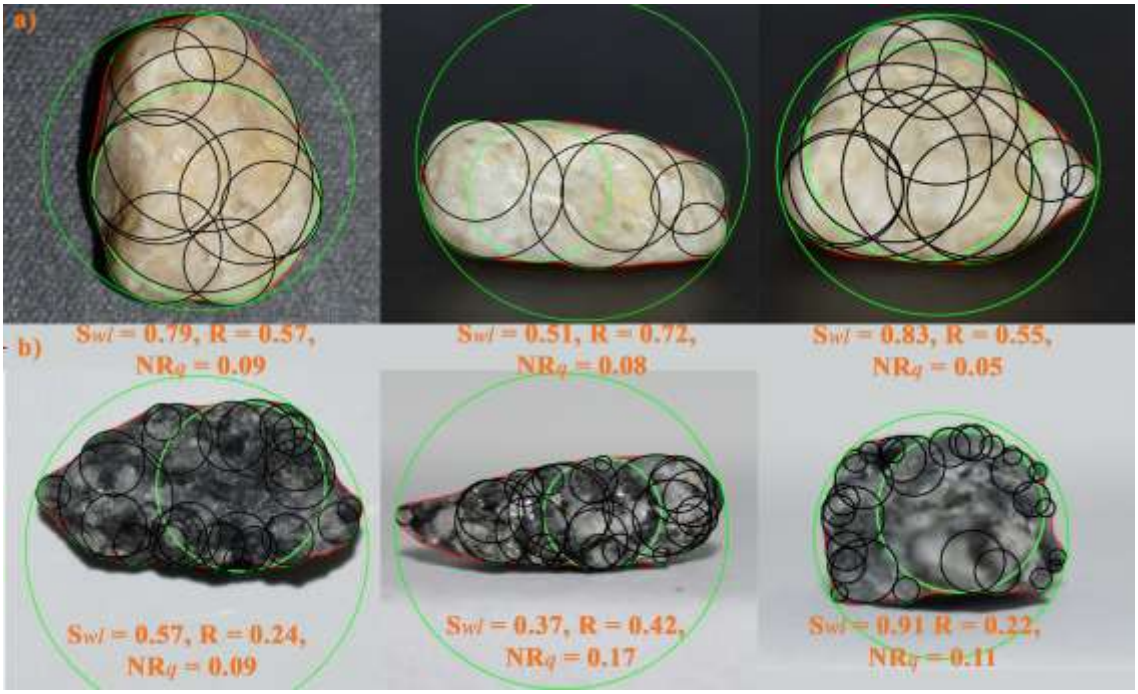

Figure 5-8 – Estimation of shape properties for a representative particle from RA and QA materials

In order to corroborate this observation, an additional set of rutting tests was conducted with the RQA material and SG2 grid at all three locations (H, 2/3H and H/3). To quantitatively illustrate the effect of particle shape, the rutting depths at 35 cycles are

plotted as shown in Figure 5-9. The effect of particle shape features on rutting depths is clearly seen.

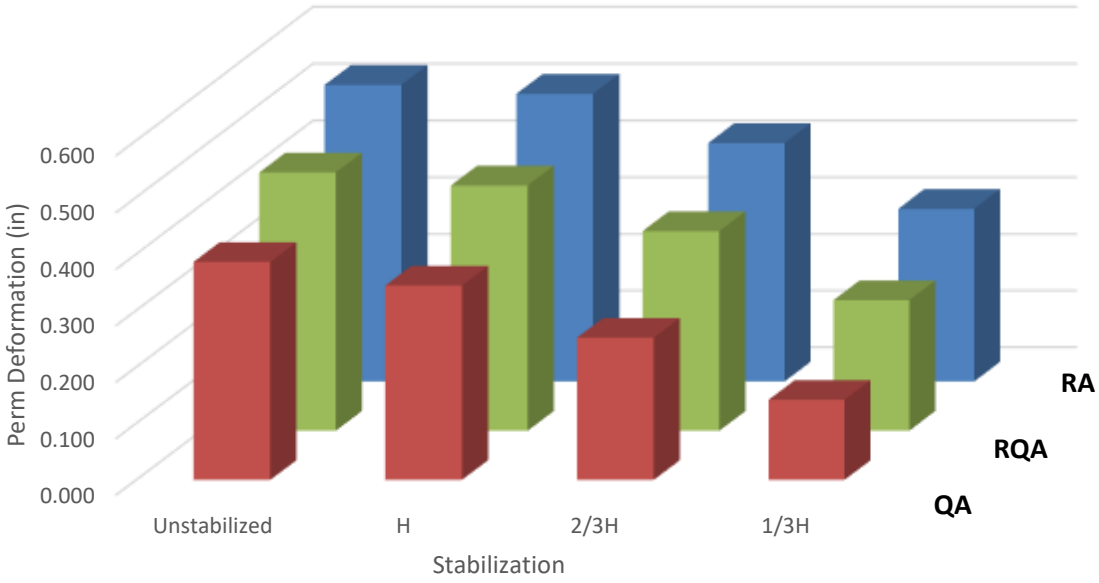

Figure 5-9 - Plot showing trends of rutting depths versus sphericity for RA, RQA and QA materials

5.4.2.4 Further Discussion

In addition to these observations relating rut-depths at the end of the test, the particle morphology also affected the evolution of rut development in the base layer at the start of the tests. In Figure 5-5, which shows the rutting curves for tests with the RA material, the curves corresponding to grids at 2H/3 and H cases follow the same initial trajectory as the unstabilized case and then branch off, typically after 3-4 loading cycles. It is important to note that the rate of accumulation of rutting is highest at the start of the test,

and therefore the displacement induced in the first 3 loading cycles is not insignificant. This indicates that the effects of the grid are only experienced after the accumulation of some amount of vertical permanent displacement. Once the wheel stresses start to affect particles which are under the influence of the confinement effects of the grid, the rutting curves begin to deflect from the trajectory of the unstabilized curve. In comparison, as is evident in Figure 5-6 for the curves with the QA material, all grids show distinct trajectories from the first loading cycle itself. This is a very interesting observation indicating the greater compatibility of the grid-QA pairs relative to grid-RA pairs to form more stable layers and requires further exploration from a computational modelling perspective to establish the underlying mechanical interactions. It is noted that the above trend with the RA material is not observed when the grids are placed at H/3, probably owing to its proximity to the surface, which would inhibit the lateral spreading of particles from the very beginning of the test along with grid stiffness playing a more crucial role.

The shape of the rutting curves in Figures 5-5 and 5-6 also suggest a direct effect of particle morphology on rutting behavior. While the rutting curves with the RA are more curvilinear in shape throughout the duration of the test, the rutting curves with the QA show a change in slope typically after 5 cycles, indicating the frictional nature of the particles.

Ultimately, pavement design is informed by a combination of technical and practical factors, among others. For example, the experiments conducted above showed the geogrid placed at one-third layer-thickness from the surface show the least rutting. This could be due greater confinement of grid for particles susceptible to lateral spreading as well as grid stiffness transmitting some of the vertical load through its ribs. However, in

reality, this is difficult to achieve in the field due to practical concerns, including grid exposure under wheel movement during construction or even grid damage by puncturing under the heavier loads near the surface. However, for thicker base layers (>10 inches), grids placed at mid-height could significantly outperform locations near the bottom. For thin base layers, it is recommended to have a very thin layer of aggregate to bed the grid and achieve proper interlock with overlying aggregate material. Otherwise, there is a danger of grid being embedded into the subgrade and reduces interlocking.

5.4.3 Rutting Tests using Polymer Geogrids

Following the set of experiments with steel grids, an analogous set of experiments were conducted using the same geogrids as described in Chapter 4. Specifically, the geogrids referred to as GG1000, GG500 and GG250, with opening sizes 1 inch, 0.5 inch and 0.25 inch were used. These geogrids have a much lower stiffness to better conform to aggregates and also are manufactured by drawing out geosynthetic sheets, as opposed to the welded procedure used for the steel grids. Therefore, it would be interesting to observe the trends in rutting with the different opening sizes. The geogrid locations were either at the bottom of the aggregate layer (depth H) or at two-thirds of the thickness from top (depth 2H/3). Following the discussion in the previous section, grid placement at H/3 was excluded from this study.

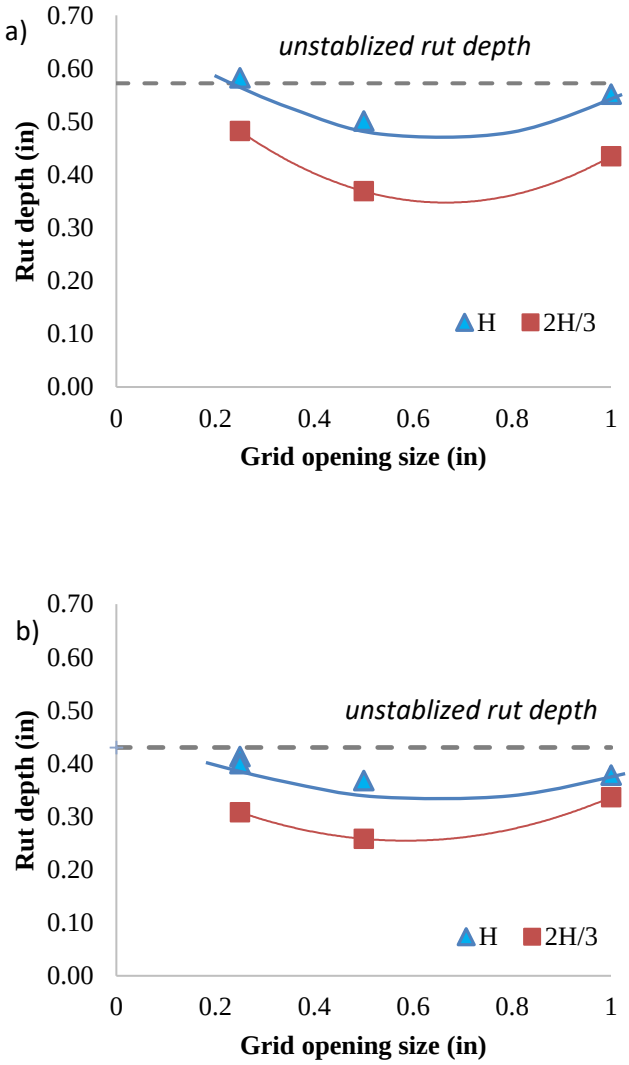

Figure 5-10 – Rutting depth for (a) RA and (b) QA materials versus opening size for the three geogrids

a)

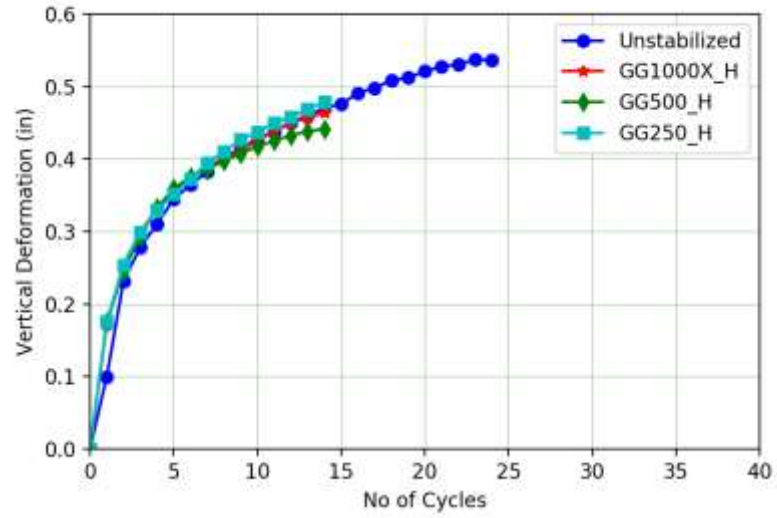

b)

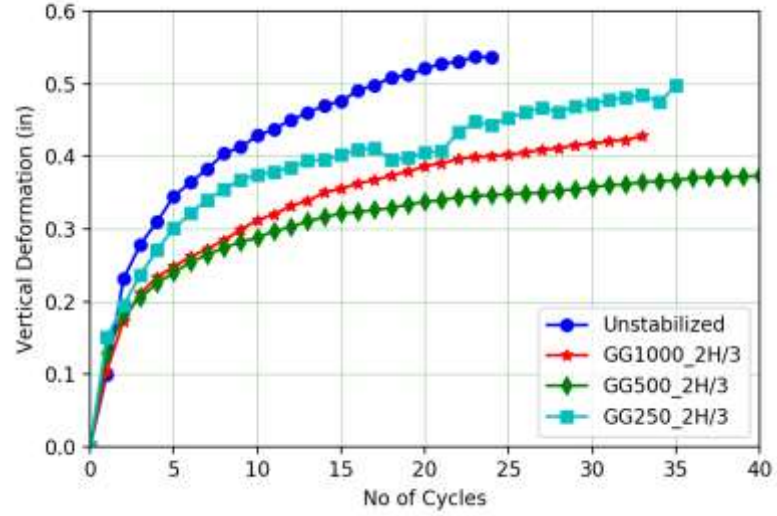

Figure 5-11 - Rutting response of RA with GG1000, GG500, G250 at location (a) H and (b) 2H/3

a)

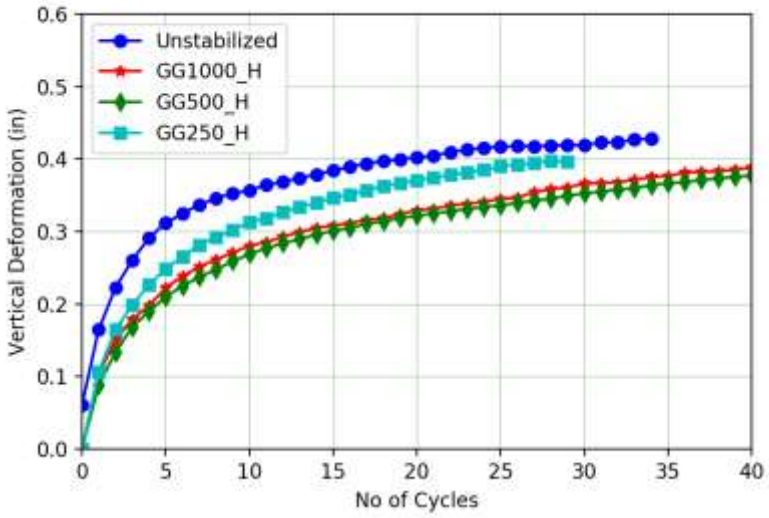

b)

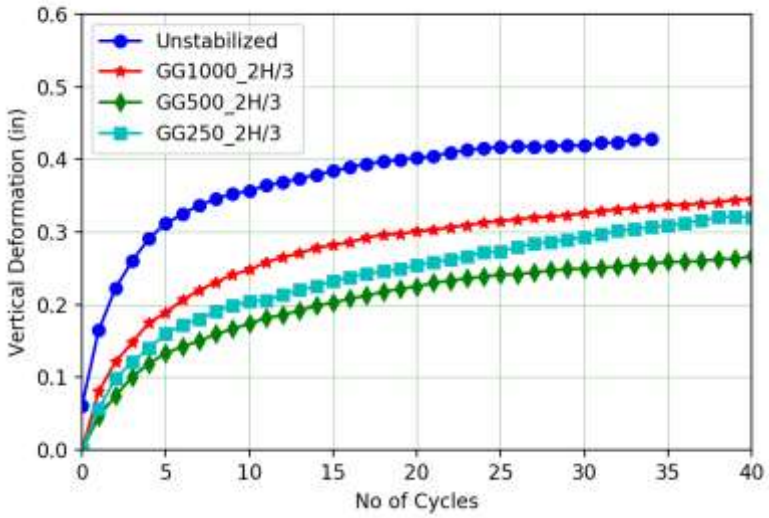

Figure 5-12 – Rutting response of QA with GG1000, GG500, G250 at location (a) H and (b) 2H/3

5.4.3.1 Discussion

The results obtained with the geogrid show a very similar pattern as observed with the steel grids. The following summarizes the observations with geogrids in comparison to the observations made previously with the steel grids.

- For the two geogrid locations considered, the rutting after 35 cycles range between 0.6 inch and 0.4 inch for the RA material and 0.4 inch and 0.25 inch for the QA material.
- The optimal opening size for the geogrids to interlock with the particles appears to be between 0.5 inch (12.7 mm) and 1 inch (25.4 mm), as shown in Figure 5-10. The distinct concave shape is observed again, very similar to Figure 5-7 with the steel grids.
- Figure 5-11 and 5-12 presents the rutting curves for RA and QA material respectively. In general, the curvilinear nature of RA material and bilinear nature of QA material is obtained, similar to tests with steel grids, indicating stabilizing potential of the QA material.
- The rutting curves with RA material all follow the same initial trajectory (also indicating similar modulus). At geogrid location H, the three curves perfectly overlap, indicating negligible influence of the geogrid. At location 2H/3 (Figure 5-11b), GG500 clearly outperforms the other geogrids.
- Rutting curves with QA (Figure 5-12) show distinct trajectories as before. GG500 performs the best for both locations. Grids placed at the bottom of the aggregate layer shows a clear influence on the surface rutting. Clearly,

aggregate morphology is a hugely influential factor in transmitting the confinement effect to surrounding particles.

Further, Figures 5-13 and 5-14 present two sets of comparison between rutting curves with geogrid and steel grid at locations H and 2H/3. Figure 5-13 shows rutting curves using grids of 0.5-inch opening size while Figure 5-14 shows rutting curves using grids with 0.25-inch openings.

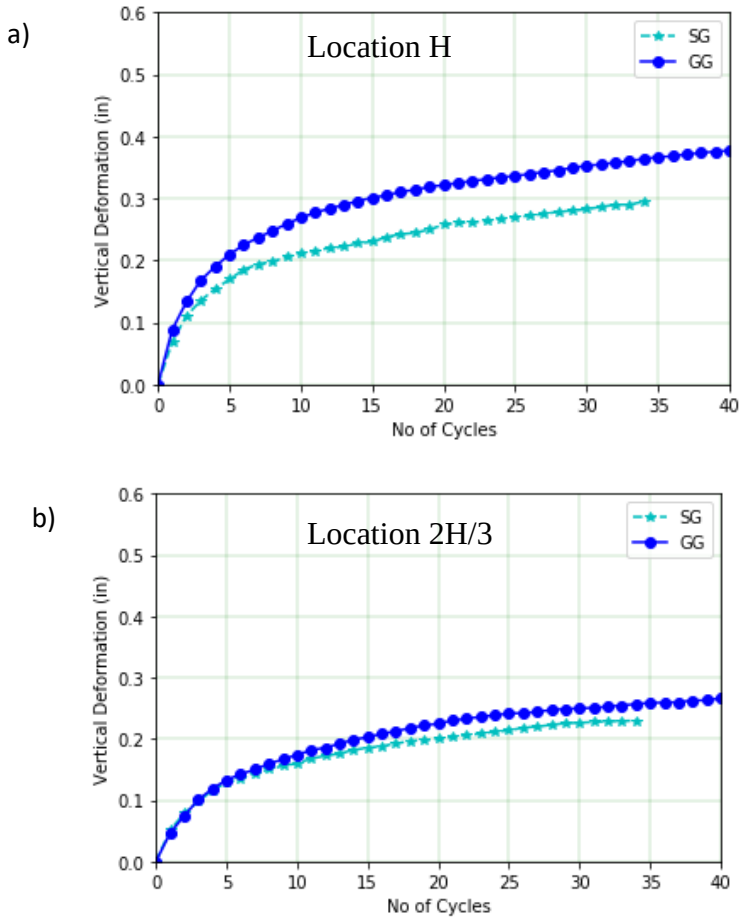

Figure 5-13 Comparison of rutting curves with 0.5 inch steel (SG) and polymer geogrids (GG) at locations H and 2H/3

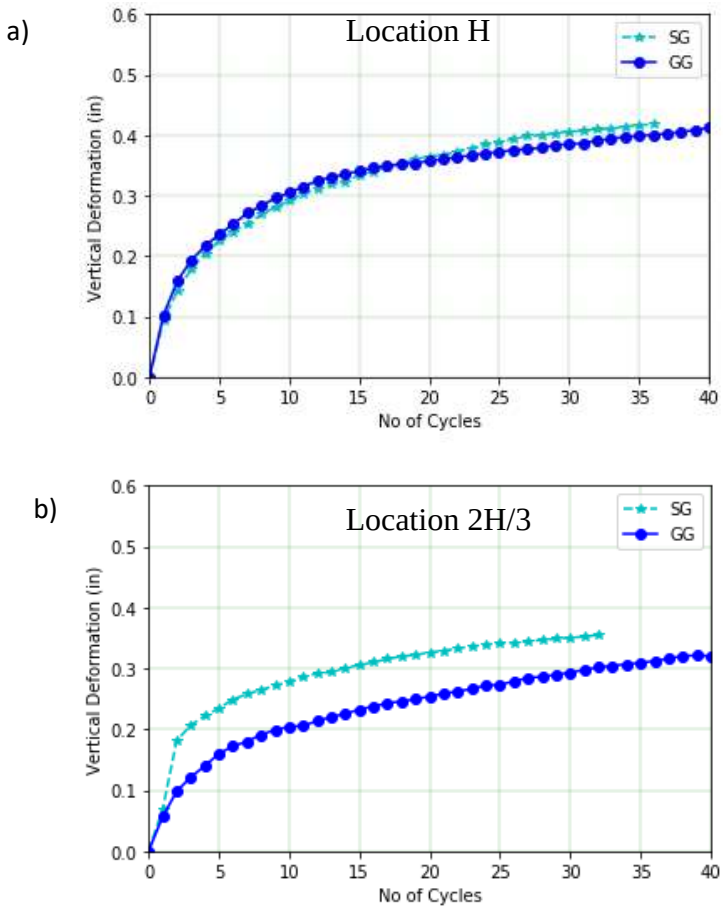

Figure 5-14 Comparison of rutting curves with 0.25 inch steel (SG) and polymer geogrids (GG) at locations H and 2H/3

At opening size of 0.5 inch, the steel grid shows lower rutting at location H ((Figure 5-13a), while grid with openings of 0.25 inch show similar rutting at this location (Figure 5-14a). At a location of 2H/3 from the top, grid openings of 0.5 inch show similar performance (Figure 5-13b). However, at an opening size of 0.25 inch, geogrids show lesser rutting than its steel counterpart. Among the 1-inch opening sizes, the steel grids outperformed the geogrids.

These results demonstrate how parameters like grid location, stiffness and opening sizes are inter-coupled with each other. For example, steel grids placed at locations H and 2H.3 showed a reduction in rutting compared to unstabilized case that was not observed with geogrids at location H. However, at shallower locations (2H/3) and at the optimal opening size, geogrids were much more effective even surpassing steel grids as shown in Figure 5-14(b). This probably arises from the benefit of flexibility to better integrate with the surrounding aggregate particles without any large voids that could potentially arise with very stiff grids.

In summary, results from this chapter further reinforces the importance of choosing the right aggregate material and appropriate geogrids for stabilization in the field.

CHAPTER 6. AGGREGATE-GEOGRID INTERACTION SIMULATION USING DISCRETE ELEMENT MODELLING

While laboratory experiments are greatly beneficial in predicting the performance of a pavement system under different operating conditions, the information obtained from them are limited to the sensors used in the tests, which are again limited in their capabilities. On the other hand, advancements in computational techniques are accelerating the adoption of numerical modelling for analyzing several engineering problems. These computational models have the benefit of generating immense data at micro and macro scales, without the need for any physical tests or sensors.

Discrete element modeling (DEM), is one such technique, which facilitates the simulation of complex physical processes by modelling the behavior of individual particles subject to Newtonian mechanics. An explicit numerical scheme is used to calculate contact forces and displacements over all particles in the simulation, based on predefined force-displacement laws and Newton's second law of motion (Cundall and Strack, 1979). A short summary of the workflow of a DEM simulation is as follows. After, the simulation geometry, material characteristics and contact laws are defined, the simulation executes the following iterative process over all particles. When two particles come in contact, the force between the particles, and resulting particle acceleration and velocities are calculated. Then, the corresponding displacement and rotation is determined and the position of the particle is appropriately updated. The entire process is repeated until a stopping condition is reached.

For this study, DEM was used to simulate a repeated-load test over various combinations of aggregate specimen and geogrid properties and testing conditions, to facilitate a comprehensive study of the effects of stabilization, geogrid aperture size and location. The 3-dimensional (3D) numerical model was developed using YADE_DEM (Smilauer et al., 2015). YADE-DEM is an open-source software library used across the world by several research laboratories and continuously updated by contributors. The following section details the modelling procedure, specimen properties followed by an analysis of the results obtained.

6.1 Geogrid and Aggregate Modelling

The first step in setting up the cyclic load simulation is to model the materials to be used in the test, i.e. aggregate particles and geogrid. The aggregate material was modelled as a collection of mon-sized spherical particles, with unit weight of 2700 kg/m3, inter-particle friction angle of 45º and normal stiffness, K_N was set to 9.6 x 10^9 N/m^2. The diameter of the particles was generally fixed at 0.5 inches or 12.5 mm. The box walls had the same interface properties as the spheres. The numerical damping coefficient (λ) was set at 0.70. A constitutive law that is an augmented implementation of the original Cundall & Strack (1979) contact law was used to govern the behavior of the particles. Along with tangential stiffness, normal stiffness, and friction coefficient, this law allows cohesion and torques at contacts. No cohesion was applied for the aggregates in any of the simulations in this study. The kinematic variables for the behavior of the particles are based on 6 degrees of freedom of the particles at each contact as shown in Figure 6-1. These are normal straining (1 DOF), shearing (2 DOFs), twisting (1 DOF) and bending (or rolling; 2 DOFs). Normal motion occurs when there is a difference of linear velocity along the interaction

axis between the two particles; shearing originates from the difference of linear or angular velocities perpendicular to the interaction axis; twisting is caused by the part of relative angular velocity parallel with interaction axis; bending arises the part of relative angular velocity perpendicular to interaction axis.

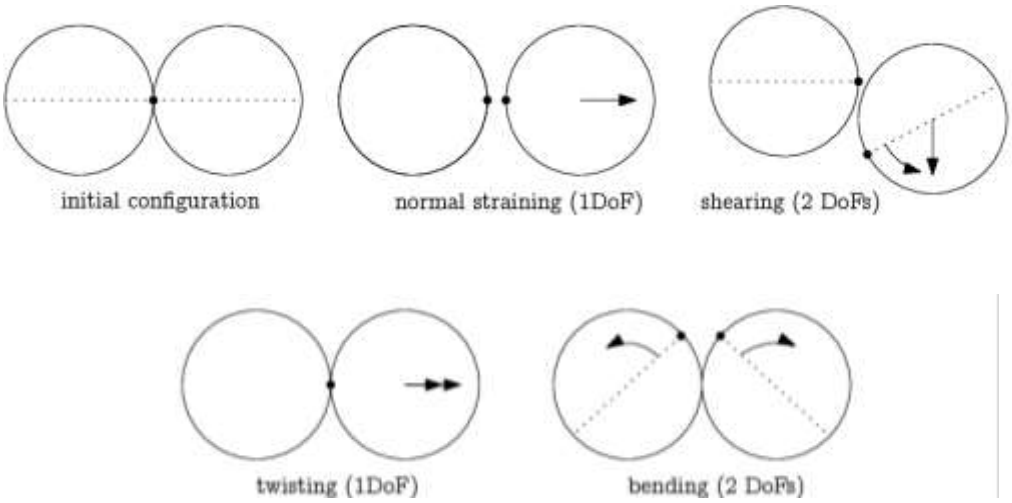

Figure 6-1 – Degrees of freedom for configuration of two particles (YADE documentation)

Figure 6-2 shows the forces and displacements at the contact point between two particles. The normal forces are calculated as linear-elastic, based on the overlap distance of the two particles in the direction of the interaction axis, denoted by **n** in Figure 6-2. The shear forces are calculated based on elasto-plastic model based on tangential displacement and Coulomb failure criterion. When the shear force is greater than the strength, the contact reaches shear failure. The expressions for normal and shear forces are presented in Equations 10 and 11.

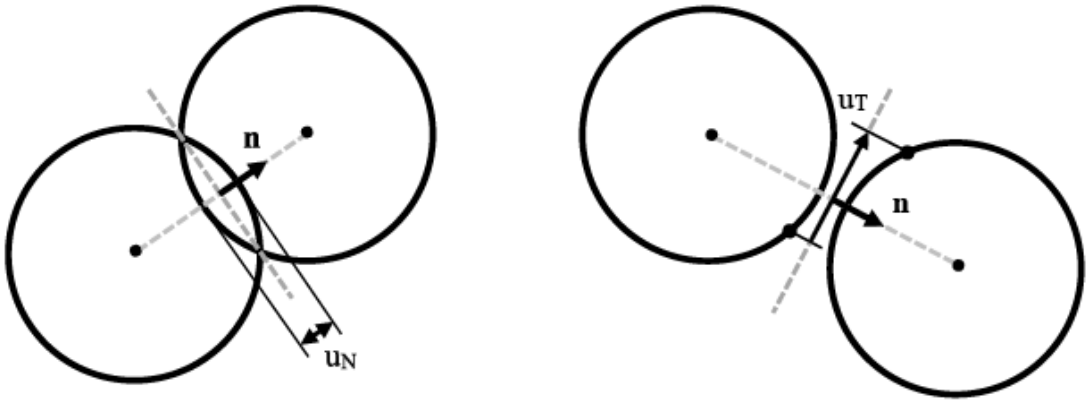

Figure 6-2 – Schematic showing normal and tangential forces at the contact between two particles

$$F_N = K_N u_N \tag{10}$$

$$F_T = \begin{cases} K_T u_T \\ |F_N| \tan \emptyset_i \ if \ K_T u_T > |F_N| \tan \emptyset_i \end{cases} \tag{11}$$

Twist and rolling stiffness (k_{tw} and k_r) are expressed as a multiple of the shear stiffness. The dimensionless multiple is represented by the terms α_{ktw} (alpha-k_{tw}) and α_{kr} (alpha-k_r) respectively. For simulations that incorporate rolling resistance, these parameters are set to an appropriate value after setting the Moment Rotation Law to True. As per this law, the bending and twisting moments are computed as per the linear relationship below, where θ is the relative rotation between the two particles.

$$M = k \theta \tag{12}$$

In the case of the geogrid, it was modelled using YADE module called gridfacet, which allows creation of grids using an arrangement of grid nodes as spheres and

connections as cylinders. For the control case for stabilized simulations, the geogrid geometry was modelled as a biaxial grid with aperture opening size of 25 mm, and rib thickness of 1.27 mm. The tensile stiffness for all geogrids were calibrated to a tensile stiffness of 220 kN/m, which corresponds to a Young's modulus of 6 x 10^9 Pa. The flexural rigidity or out-of-plane stiffness of the geogrid was calibrated based on ASTM D47748, by measuring the length of a strip of geogrid needed to bend by 41.5º from the horizontal under its own weight. The simulation generated geogrid was calibrated to a real BX1200.

6.2 Simulation Setup

The goal of this exercise for the current study is to provide a glimpse into the particle-level information available using DEM technique. The scale of the model was chosen to achieve a balance between incorporating a sufficiently sized geogrid to observe benefits as well as reduce computation time. The aggregate particles are generated as spheres and assembled in a chamber measuring 0.4 m x 0.4 m x 0.4 m (16 inches-cube) in two layers. The geogrid was typically placed in the middle of the specimen before generation of the top layer of aggregate particles. Figure 6-3 shows a geogrid-stabilized specimen with the geogrid located in the middle and loading cylinder over the specimen. Next, the chamber is cyclically constricted and expanded axially to simulate the compaction process, which results in rearrangement of the particles to a denser state. If the geogrid is present in the specimen, this ensures, interlocking between the aggregate particles and geogrid openings. While the thickness of the specimen was chosen to be approximately 0.4 m (16 inches) prior to compaction, which reduced to 0.2 m (8 inches) after the compaction stage. The loading cylinder, measuring 0.1 m (4 inches) in diameter, is made to cyclically impact-load the specimen applying a predefined stress for at least 300

cycles. The performance of the specimen was assessed at a range of loading stresses, with the baseline being 27.6 psi or 190 kPa. This value was chosen to be the same as that used in the experimental study presented in Chapter 4, reasoned as the typical stress experienced at the top of the base layer in surfaced pavements under maximum truck loads.

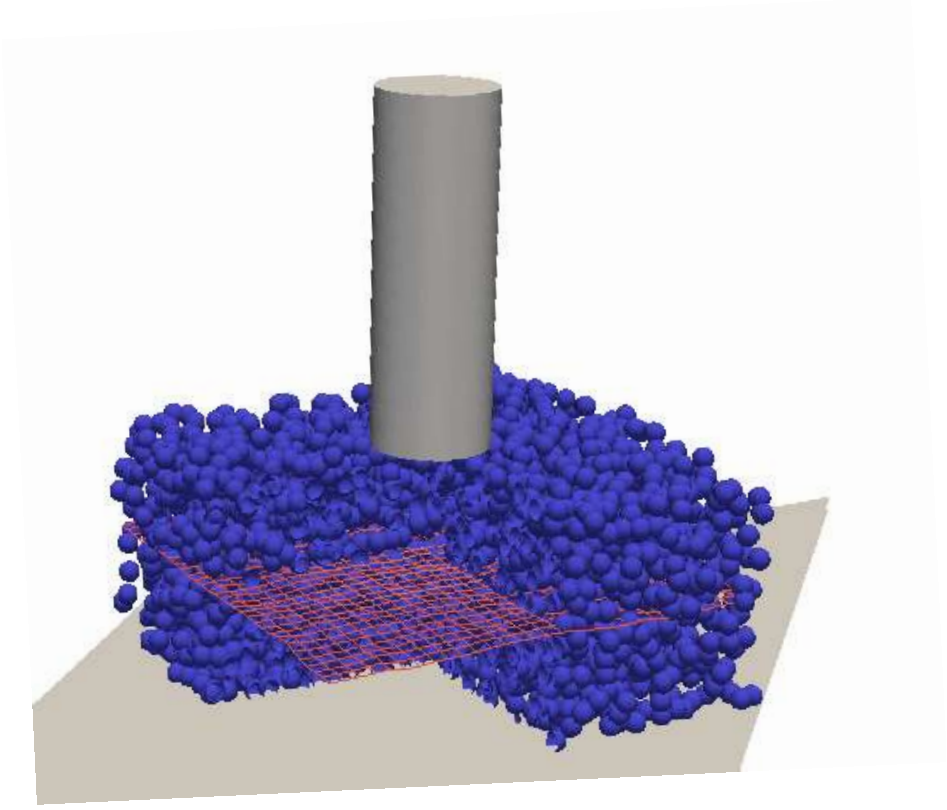

Figure 6-3 - DEM specimen and loading setup

6.3 Performance variables

The primary performance parameters that are recorded during each simulation are the surface vertical deformation, porosity, lateral displacement for each particle and mean lateral displacement calculated at several sub-layers in the specimen. The surface vertical deformation or rutting is recorded as the downward displacement of the bottom of the

loading cylinder at the end of each loading stage. The porosity is calculated using a built-in function in the middle one-third volume around the central axis of the chamber, extending from under the cylinder down to the bottom of the specimen. It does so by dividing the volume into voxels of user-defined resolution and estimating the fraction of volume that does not belong to spheres (particles). These two parameters are estimated in each cycle of loading/unloading. Additionally, an extensive volume of information including particle displacements and rotations in x, y, z direction, interaction forces between particles as well as forces and displacements in the geogrid ribs and nodes are recorded at cycles 1, 10, 50, 100, 200, 300 cycles during the simulation. Lateral deformations profiles at these loading stages can be obtained by plotting movement of each individual particle or by estimating the mean for all particles in a given sub-layer.

6.4 Parametric Study

The following were the parameters considered for the DEM modelling:

- Applied loading stresses: Keeping all other variables the same, the specimens were tested at loading stresses of 70, 100, 140 and 190 kPa for both unstabilized and stabilized conditions.
- Grid opening size or Aggregate diameter to geogrid ratio (AGR): The AGR is typically used to compare performances of various geogrid openings with an aggregate mix of known particle gradation. As stated earlier in Chapter 2, the general guideline is to have the geogrid rib length between the D50 and 2*D85 of the aggregate mix. To evaluate this, geogrids with a range of opening sizes from 12.5 mm to 60 mm were generated in the simulation and tested with 12.5 mm diameter aggregate particles.

- Location of geogrid: Results from Chapter 5 showed that grids placed closer to the pavement surface were more effective in limiting surface rutting. Simulations were conducted with the geogrid placed at 0.3H from the surface, and compared with the geogrid locations of 0.5H and 0.67H, where H is the thickness of the aggregate layer.
- Aggregate properties: Rounded aggregates are more prone to rutting due to lack of inter-particle interaction, both frictional and interlocking, while angular particles demonstrate improved rutting performance. To evaluate the effect of aggregate properties, rounded aggregates were generated as spherical particles with zero rolling resistance and angular aggregates as spherical particles with nonzero rolling resistance. The rolling resistance can be defined using the rolling stiffness parameter and the rolling strength parameter, in the laws governing material behavior, as mentioned previously. It is important to emphasize that aggregate particles with zero rolling resistance does not indicate absence of frictional interaction between the particles. The particles still do exhibit frictional resistance and rolling tendencies. The rolling resistance increases the 'interlocking' tendency of the material assembly by means of introducing rotational bending and twisting moments.
- Grid stiffness: The stiffness of the grid influences the manner of interaction with the aggregate particles in relation to rutting performance with steel grids and geogrids. Even at the low number of cycles and low stresses used in the experiments presented in Chapter 5, there was an effect of stiffness observed. To gain further clarity, DEM simulations were performed using geogrids with typical stiffness

values (BX1200) and a grid with very high stiffness (both Young's modulus and out-of-plane stiffness) to simulate a steel grid.

The goal from running the various cases listed above is to gather evidence for formulating an understanding of aggregate-geogrid interaction and identifying the influence zone of geogrid focusing on lateral displacements. Information about lateral displacement behavior of particles under cyclic loading for the various cases can be a crucial in linking aggregate-geogrid interaction to pavement performance.

6.5 Results and Discussion

6.5.1 Effect of loading stress

The surface rutting and porosity curves for three loading stresses, i.e. 70, 140 and 190 kPa are presented in Figure 6-4 and 6-5 respectively. Increasing stresses are resulting in greater rutting deformations as expected. The linear shape of the rutting curves instead of the exponential shape observed in the lab experiments is probably because of a combination of reasons. Firstly, the idealized nature of the material comprised of mono-sized spheres would prevent the formation of an interlocked matrix. As a result, the applied loads would cause constant readjustment of particles inducing a relatively greater rate of deformation accumulation. Secondly, the number of cycles required to reach the stabilized state and thus a plateau in the rutting curves, is greater than the 300-400 cycle range of the simulations. The latter aspect was illustrated by running a simulation up to 1200 loading cycles, and the rutting curve was observed to plateau. This is shown later in this chapter.

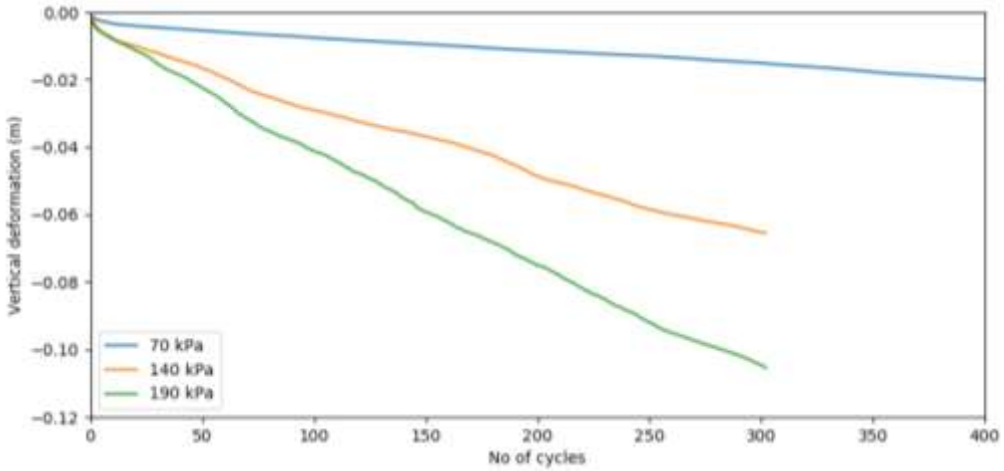

Figure 6-4 - Rutting curves at 70, 140 and 190 kPa

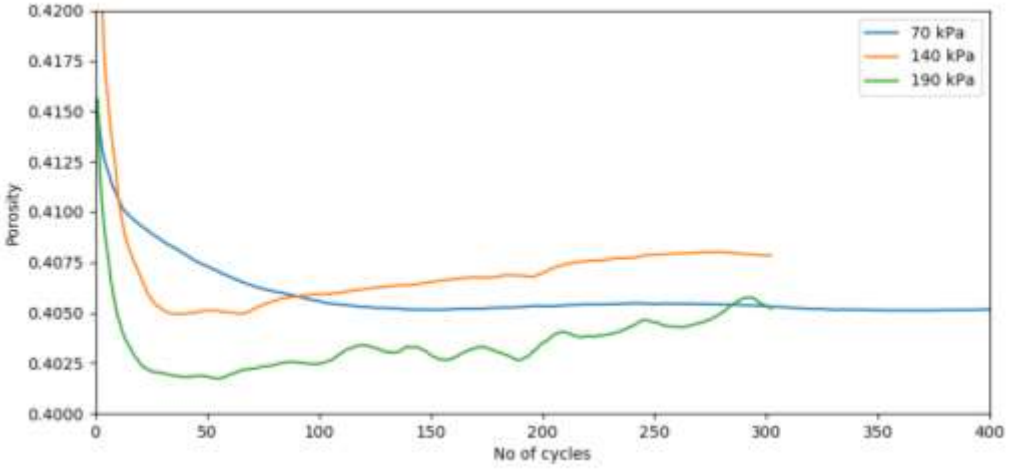

Figure 6-5 - Change in porosity with loading cycles at 70, 140 and 190 kPa

The porosity curves in Figure 6-5 all show drastic densification in the first few cycles followed by stabilization in the case of 70 kPa or slight dilation at higher stresses. At higher stresses, the loading cylinder causes greater particle displacements sideways and towards the unconfined boundary at the top of the specimen, causing the porosity to

increase. This effect can be observed in the form of particle rotations shown in the specimen cross-sections in Figure 6-6.

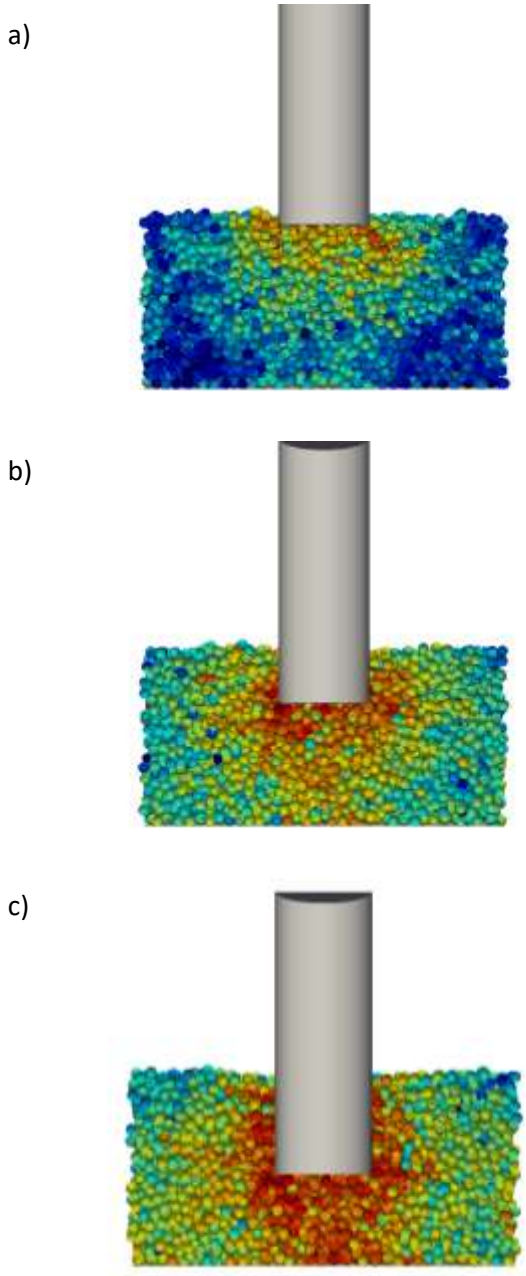

Figure 6-6 - Cross-sections of specimens after 300 loading cycles at a) 70 kPa, b) 140 kPa and c) 190 kPa. Particle colored by magnitude of rotation

Figure 6-6 shows the cross-sections of specimens at the end of the 300 loading cycles at the three loading stresses. The colors of the particles are based on the amount of rotation experienced during the course of the test. Clearly, the specimen is showing larger deformation as well as rotations at 190 kPa loading stress than at other lower stress levels.

The accumulation of vertical deformations is coupled with particle displacements in horizontal direction; therefore, visualizing the horizontal movement of the particles could provide insights into the evolution of rutting behavior over the duration of the simulation. To do this, the specimen was divided into 10 sublayers, and the mean horizontal displacement was estimated in each sublayer by calculating the average horizontal displacement of all particles in the sublayers. Figure 6-7 shows this data plotted at various stages of the test, for surface loading stresses of 70, 140 and 190 kPa. In each displacement profile shown, the horizontal displacement increases up to a certain depth before tapering downward. These profiles shift rightward with increasing number of loading cycles as the displacements accumulate. Additionally, the region with peak horizontal displacement shifts downward with increasing number of loading cycles, as the cylinder penetrates downward through the specimen. For the three different loading stresses, the displacement profiles exhibit greater magnitudes of displacements at higher stresses as expected. It is also evident that at higher stresses, the particles in the lower half of the specimen are pushed outward, indicating the formation of a wedge under the loading cylinder.

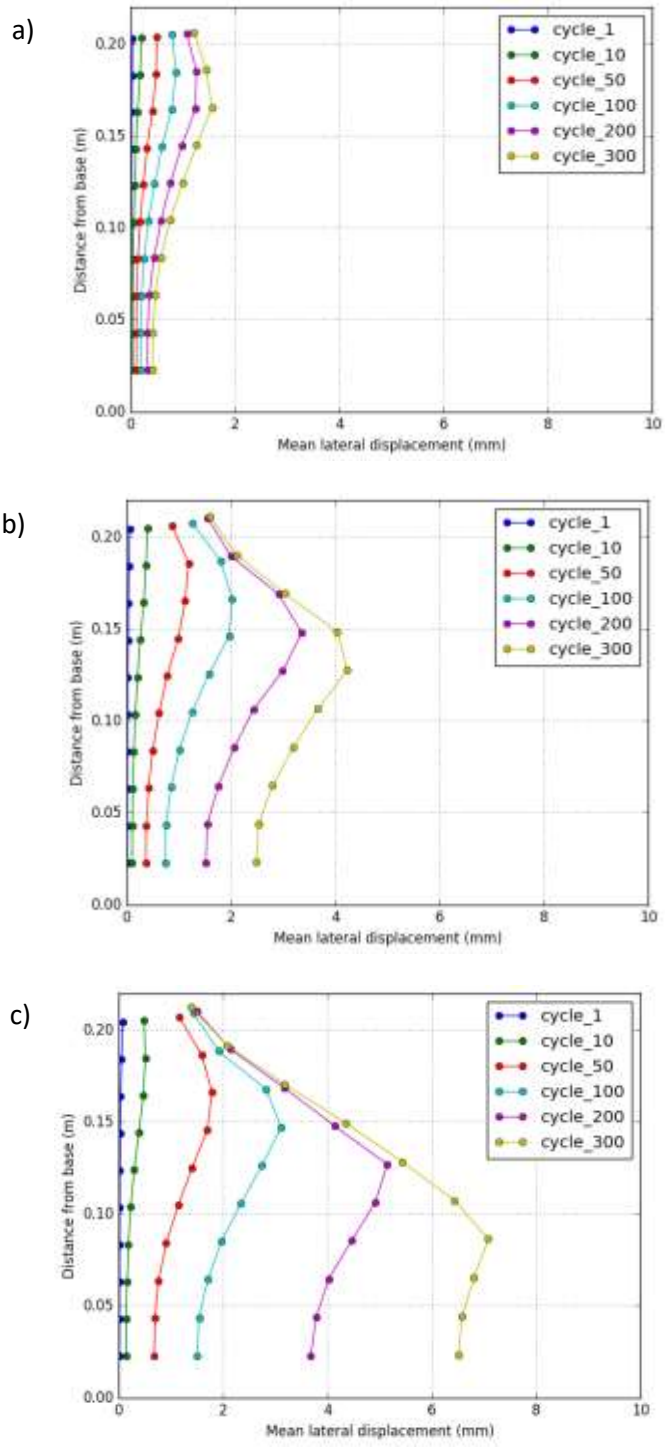

Figure 6-7 - Profiles of mean lateral displacement across thickness of aggregate layer at various testing stages at (a) 70 kPa, (b) 140 kPa and (c) 190 kPa.

6.5.2 Effect of Geogrid Stabilization

Inclusion of a geogrid in the above scenario should limit the lateral displacements of particles, thereby limiting vertical deformation. In Figure 6-8, this effect is observed by plotting and comparing the particle displacement vectors for an unstabilized and a stabilized specimen (with 25-mm geogrid) at 190 kPa for various stages of the simulation. The influence of the geogrid in constraining particle movement becomes more evident after 100 loading cycles. In the early stages of the test, the particles at the surface which are not close enough to the geogrid to experience the confinement provided by the improved interlocking are easily displaced. As the loading cylinder continues to penetrate through the specimen, it approaches particles that are under greater confinement which causes the rate of rutting to decrease. This behavior is also reflected in the corresponding rutting curves for the same specimens, shown in Figure 6-9, where the stabilized specimen overlaps with unstabilized specimen curve until approximately 100 loading cycles before diverging. It is worth noting this behavior was also observed in the rutting tests with the RA material in Chapter 5.

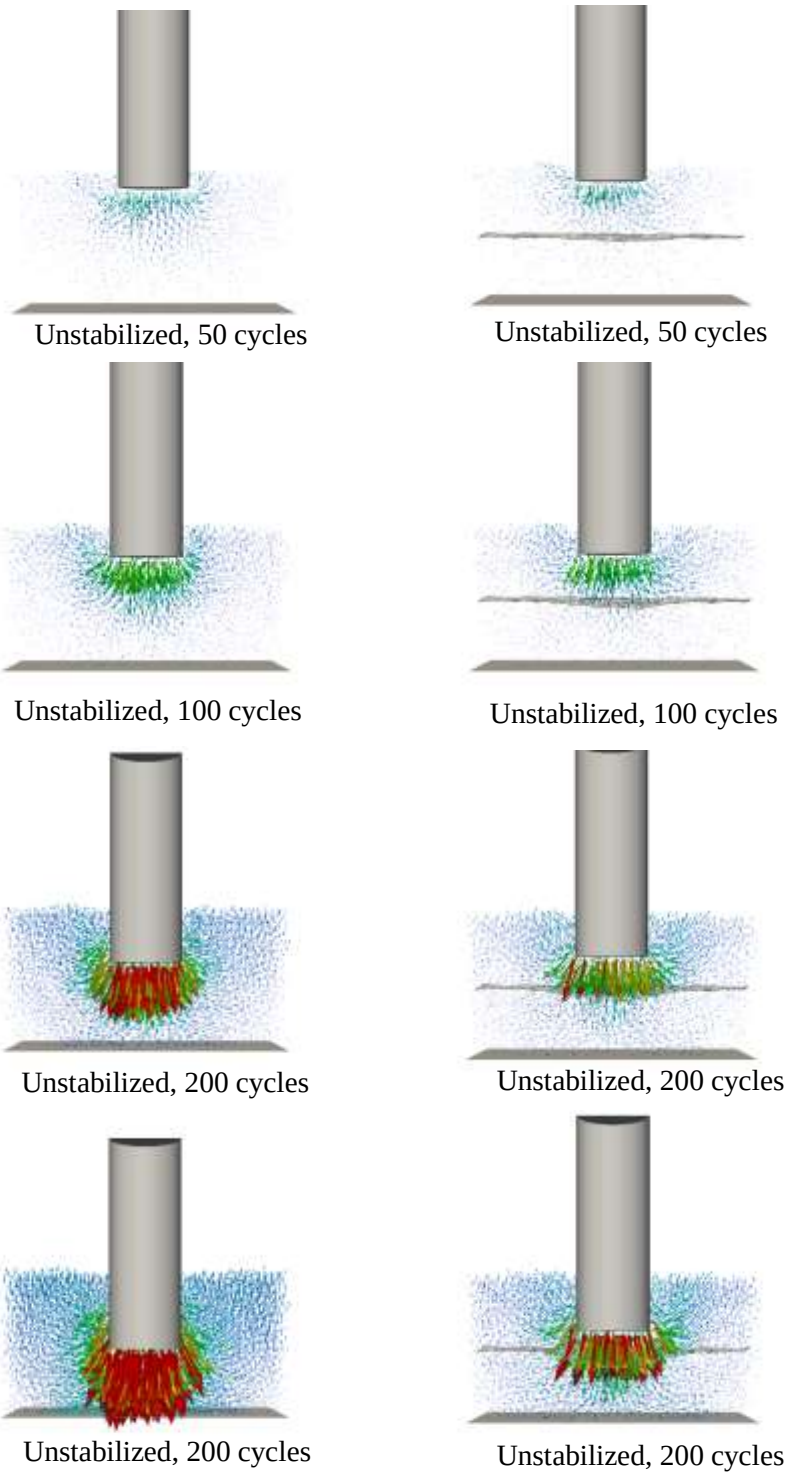

Figure 6-8 - Comparison of mean deformations for unstabilized and stabilized cases

Specimens stabilized with 25-mm aperture geogrids were also tested at 70 and 140 kPa. The rutting curves at all 3 stress levels are presented in Figure 6-10. Observing just the rutting curves at 140 and 190 kPa, the influence of the geogrid seems to emerge at different stages of the test, i.e., around 90 loading cycles at 190kpa and 180 loading cycles at 140 kPa. At 70 kPa, the small amount of surface penetration seems to not reach the influence zone of the geogrid, causing both curves to generally overlap.

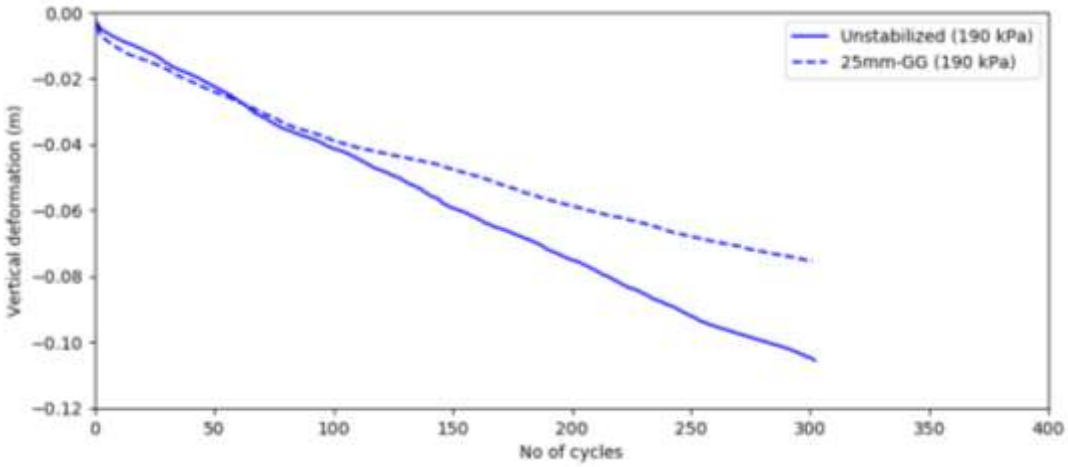

Figure 6-9 - Rutting curve for an unstabilized and stabilized specimen at 190 kPa

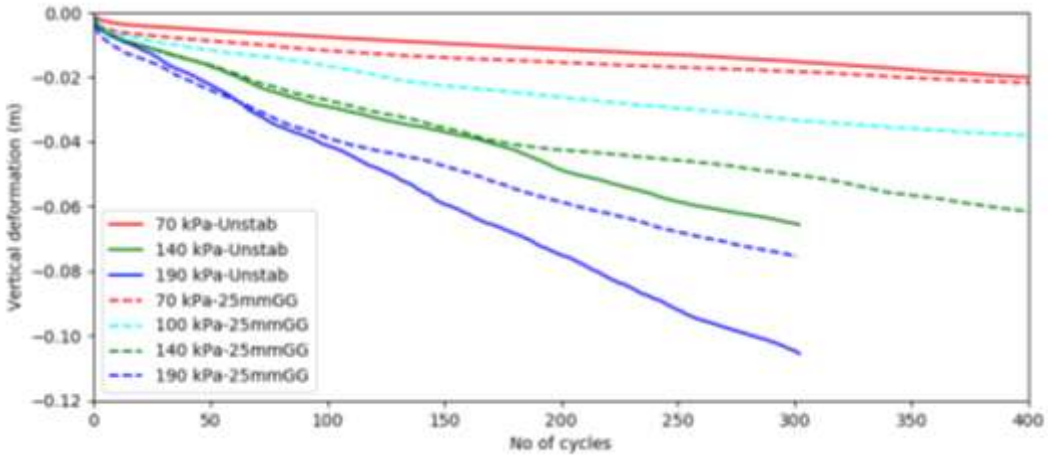

Figure 6-10 - Rutting curves for unstabilized (solid) and stabilized (dashed) specimens at 70, 140 and 190 kPa.

The lateral displacement profiles at various stages of the test for the geogrid-stabilized specimen are shown in Figure 6-11(b), along with unstabilized specimen profiles shown (Figure 6-11a). The following observations are worth noting by comparing the two figures.

- At the location of the geogrid, the lateral displacements are significantly curtailed in comparison with the unstabilized specimen test demonstrating the lateral confinement capability of the geogrid.
- Even though the vertical deformation (rutting) curve shows divergence at 100 loading cycles, the horizontal deformations at the geogrid elevation are lesser even at 50 loading cycles. The geogrid has a clear influence at this stage of the test.

In addition to the reduced lateral deformations at the geogrid elevation, even particles located above the geogrid elevation (0.11 m) show lower lateral deformations in

the stabilized specimen compared to the unstabilized specimen. This is true even at 50 loading cycles, although it becomes more evident at later stages in the test. For example, at 50 cycles, the lateral displacement at 0.15m elevation for the stabilized specimen is lower. This shows that the geogrid is having an influence on particles even further away than its immediate vicinity.

The lateral displacement profiles presented in Figure 6-11 also contain useful information about the influence zone of the geogrid. Figure 6-12 presents the lateral displacement profiles for unstabilized and stabilized (25mm GG) cases at cycles 10, 50 and 100. At 10 loading cycles, both cases show the same lateral displacements. At 50 loading cycles, the effect of the geogrid is already evident, with smaller displacements observed in almost the entire specimen. This indicates that the influence zone of the geogrid extends almost until the surface of the specimen. With increasing loading cycles, all sub-layers underneath the loading cylinder exhibit smaller deformations than the unstabilized case.

a)

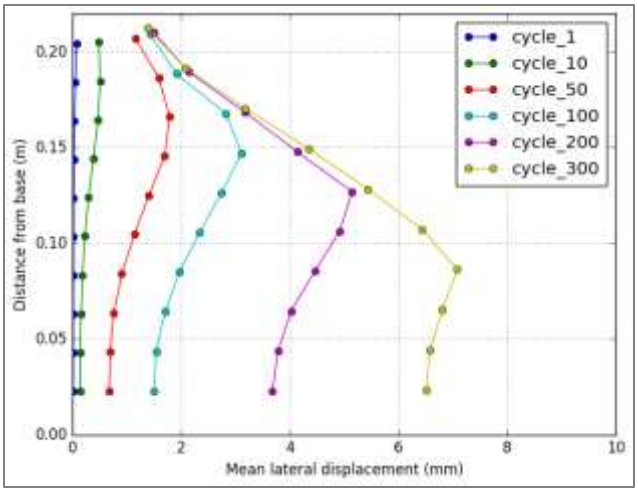

b)

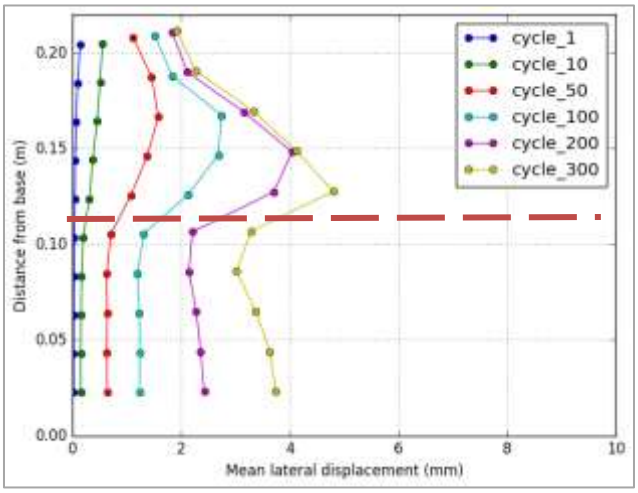

Figure 6-11 - Profiles of mean lateral displacement across thickness of aggregate layer at 190 kPa for (a) unstabilized and (b) stabilized specimens

The above discussion shows that the lateral displacement profiles are indicative of the mechanisms inside the aggregate layer, and useful in gauging the extent of the influence zone of the geogrid.

a)

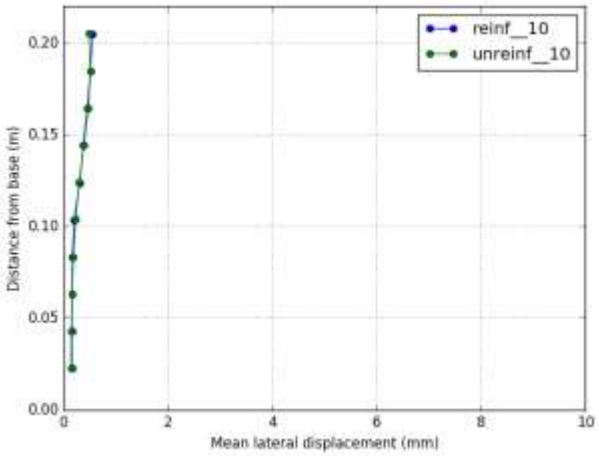

b)

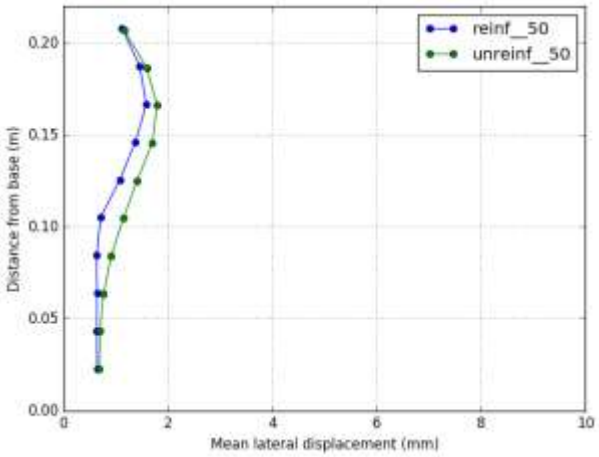

c)

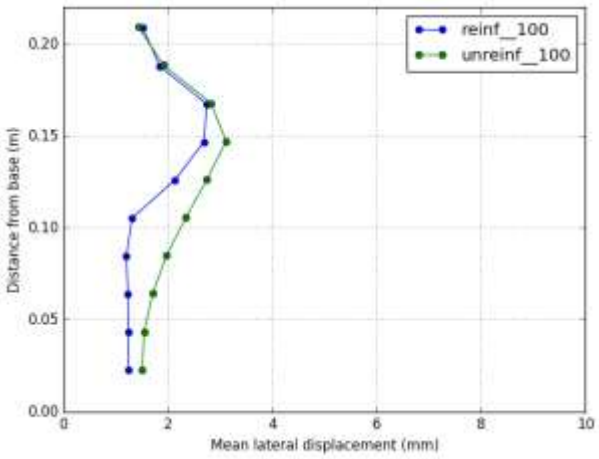

Figure 6-12 - Comparison of lateral displacements for unstabilized and stabilized specimens at a) 10 cycles, b) 50 cycles and c) 100 cycles at 190 kPa

To illustrate the lateral displacement behavior at different loading stresses, profiles for the cases corresponding to 70 kPa and 140 kPa are presented in Figure 6-13. At 70 kPa, there is no distinguishable difference between the unstabilized and stabilized tests (Figure 6-13a), indicating the stress level is too low to reach the influence zone of the geogrid. However, at 140 kPa (Figure 6-13b) and 190 kPa (Figure 6-11) the geogrid clearly restricts lateral motion of the particles around it, which results in the rutting behavior observed in Figure 6-10. This clearly illustrates the direct relationship between surface rutting deformation and lateral displacements within the aggregate layer.

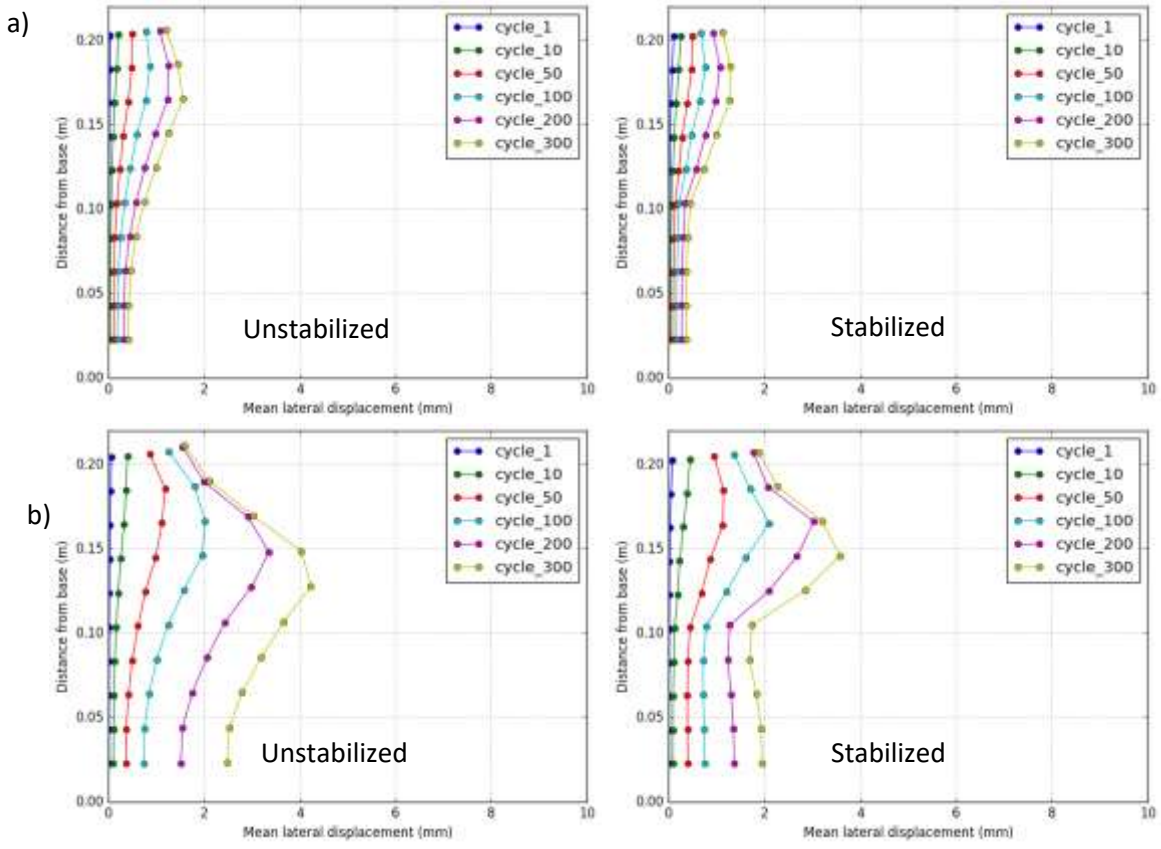

Figure 6-13 - Lateral displacement profiles at a) 70 kPa and b) 140 kPa

6.5.2.1 Prediction of Rutting at 100 kPa

With rutting behaviour available for 70, 140 and 190 kPa, a linear trend is observed in the applied stress versus rutting depths. Using this trend, the rutting displacement at 100 kPa was interpolated and compared with that obtained with simulation results at 100kPa. A very close match is observed as shown in Figure 6-14 for both stabilized and unstabilized cases. The following interesting observations are also evident from Figure 6-14. The diverging nature of the stabilized and unstabilized trends reiterated several observations from literature that the benefits of geogrids are evident at extreme performance scenarios like high stresses, poor-quality aggregates or soft subgrades. The ratio of unstabilized to stabilized depths increases from 1.0 at 70 kPa to 1.17, 1.36 and 1.45 at 100, 140 and 190 kPa respectively. Further, since the stabilized rutting trend is also linear with respect to stress, the contribution of geogrid can also be considered as linear with stress.

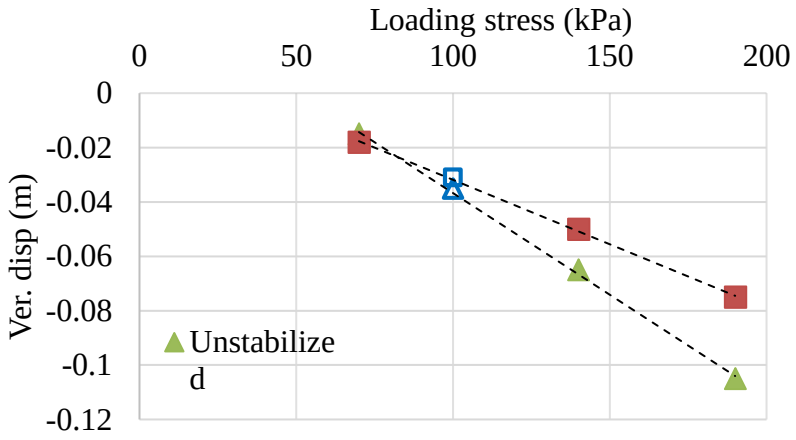

Figure 6-14 - Vertical deformation for unstabilized stabilized specimens at various stress levels and after 300 loading cycles

6.5.3 Effect of Geogrid Opening Size

Figure 6-12 presented the lateral displacement plots for 25 mm geogrid compared with the unstabilized specimen at 10, 50 and 100 loading cycles. At 50 cycles, the geogrid clearly showed a reduction in lateral displacement of particles. A similar simulation was conducted using a 37-mm geogrid and the corresponding plots are showed in Figure 6-15. Figure 6-15 (a) and (b) are identical for both cases showing the geogrid is not having much of an impact. At 100 loading cycles, the 37-mm geogrid shows lower deformation in its vicinity, up to about 0.15 m. In comparison, at the same stage of the test, the 25-mm geogrid showed lower deformation up to 0.175 m in the specimen. Clearly, the 25-mm geogrid shows superior interlocking compared to the 37-mm geogrid. This would indicate that the 25-mm geogrid should allow lower surface deformation compared to the 37-mm geogrid.

a)

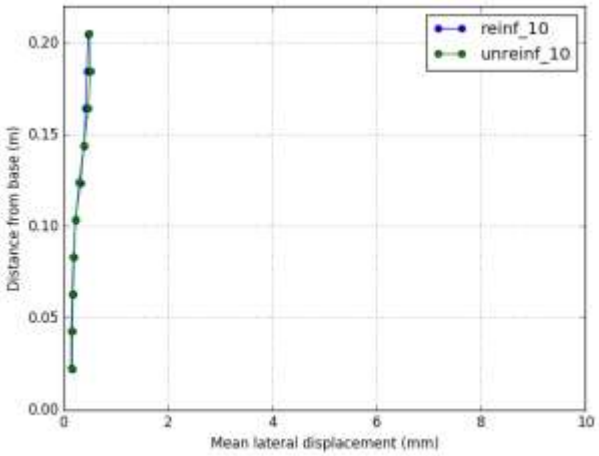

b)

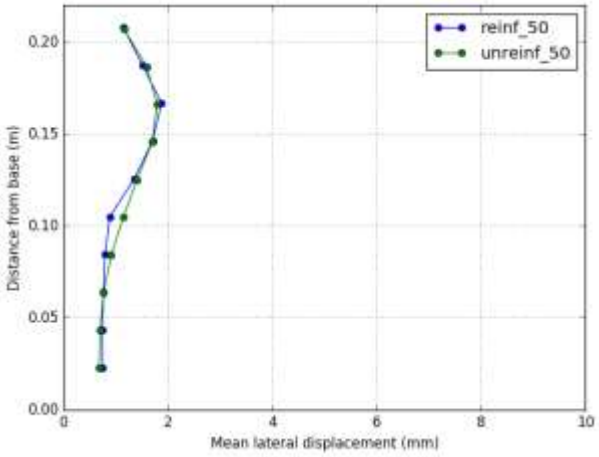

c)

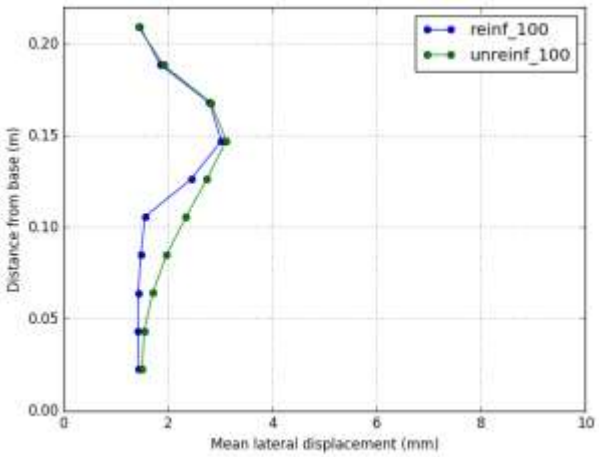

Figure 6-15 - Lateral displacement profiles for 37 mm geogrid stabilized specimen at 10, 50 and 100 loading cycles

Figure 6-16 shows the rutting and porosity curves with geogrids of 12.5, 25, 37 and 60-mm openings with aggregate particles of 12.5 mm in diameter and 190 kPa loading stress. The rutting curves establish superior performance of the 12.5 and 25-mm geogrids while 37 mm and 60 mm geogrids are similar. The 12.5 mm geogrid presents an interesting observation. The deviation in stabilized rutting curve from unstabilized curve that all geogrids exhibit happens very early in the case of the 12.5 mm geogrid. This is probably due to the relatively quick rearrangement so that each geogrid opening accommodates one particle, which is then difficult to displace due to the similarity in sizes. While this observation is understandable in the case of idealized spherical particles, real granular particles would not perfectly fit in the geogrid openings of this size thereby inhibiting efficient interlocking, as observed in the experimental study in Chapter 5. On the other hand, the 25-mm, 37-mm and 60-mm geogrids overlap with the unstabilized-specimen rutting curve initially to different number of loading cycles, before the geogrid confinement effect begins to dominate causing a divergence.

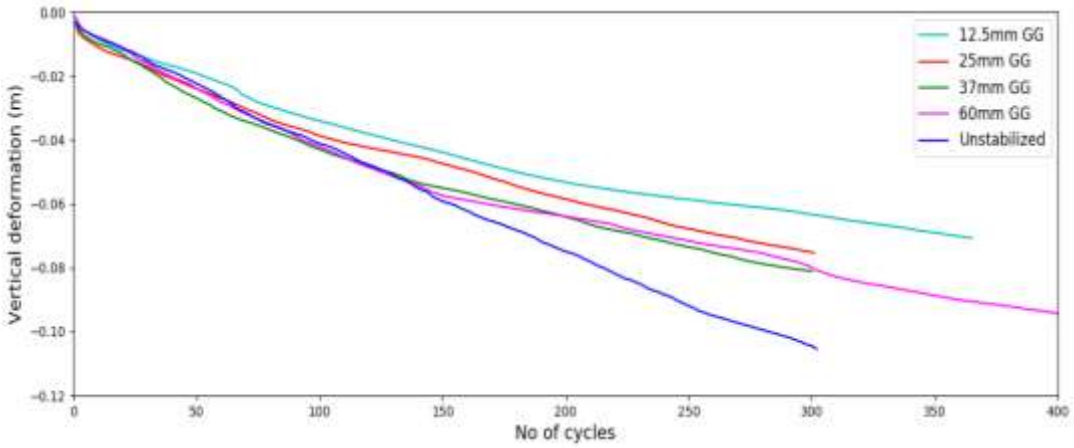

Figure 6-16 - Rutting curves for unstabilized and stabilized specimens using 25, 37 and 60-mm geogrids

To get a sense of the rutting behaviour for particle that are larger than geogrid openings, a simulation was conducted with 12.5 mm geogrid and 15-mm diameter particles. As anticipated, results showed greater rutting than the case with 1:1 ratio of geogrid to aggregate particle diameter. A bar chart showing the total rutting at 300 loading cycles for the various aggregate-geogrid combinations is shown in Figure 6-17. The combinations are represented using ratios of geogrid rib length to aggregate diameters (Table 6-1). Geogrid to aggregate size ratios between 1.0 and 2.0 facilitate tight interlocking and reduced surface rutting.

In Chapter 5, the optimal geogrid opening size for 6.35-9.5 mm particles was observed to be 19 mm (ratio of 2.4 using D50 of 7.93 mm). In the real world, aggregate particles are irregularly shaped, and it is more challenging to represent the particle size using one number. For example, the circumscribed circle around the particle outline would be larger than the actual particle size that falls through the corresponding given sieve

opening. In any case, the experimental and simulation results suggest a ratio of 1.0– 2.5 to mobilize sufficient interlocking to reduce rutting.

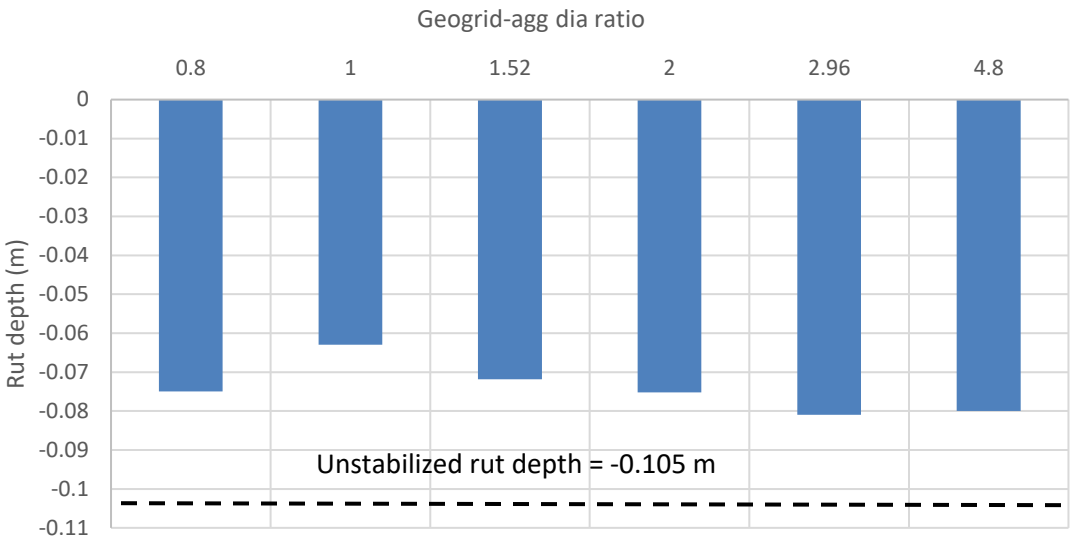

Figure 6-17 - Geogrid to aggregate diameter ratio vs rut depth

Table 6-1 - Various aggregate-geogrid combinations considered in study

Case	Geogrid rib length	Aggregate diameter	Geogrid to agg ratio
1	12.5	15	0.8
2	12.5	12.5	1.0
3	19	12.5	1.5
4	25	12.5	2.0
5	37	12.5	3.0
6	60	12.5	4.8

The superior performance of the 12.5 geogrid with 12.5–mm diameter particles (case 2 in Table 6-1) can also be observed from the displacement vector plot after 300 loading cycles, shown in Figure 6-18.

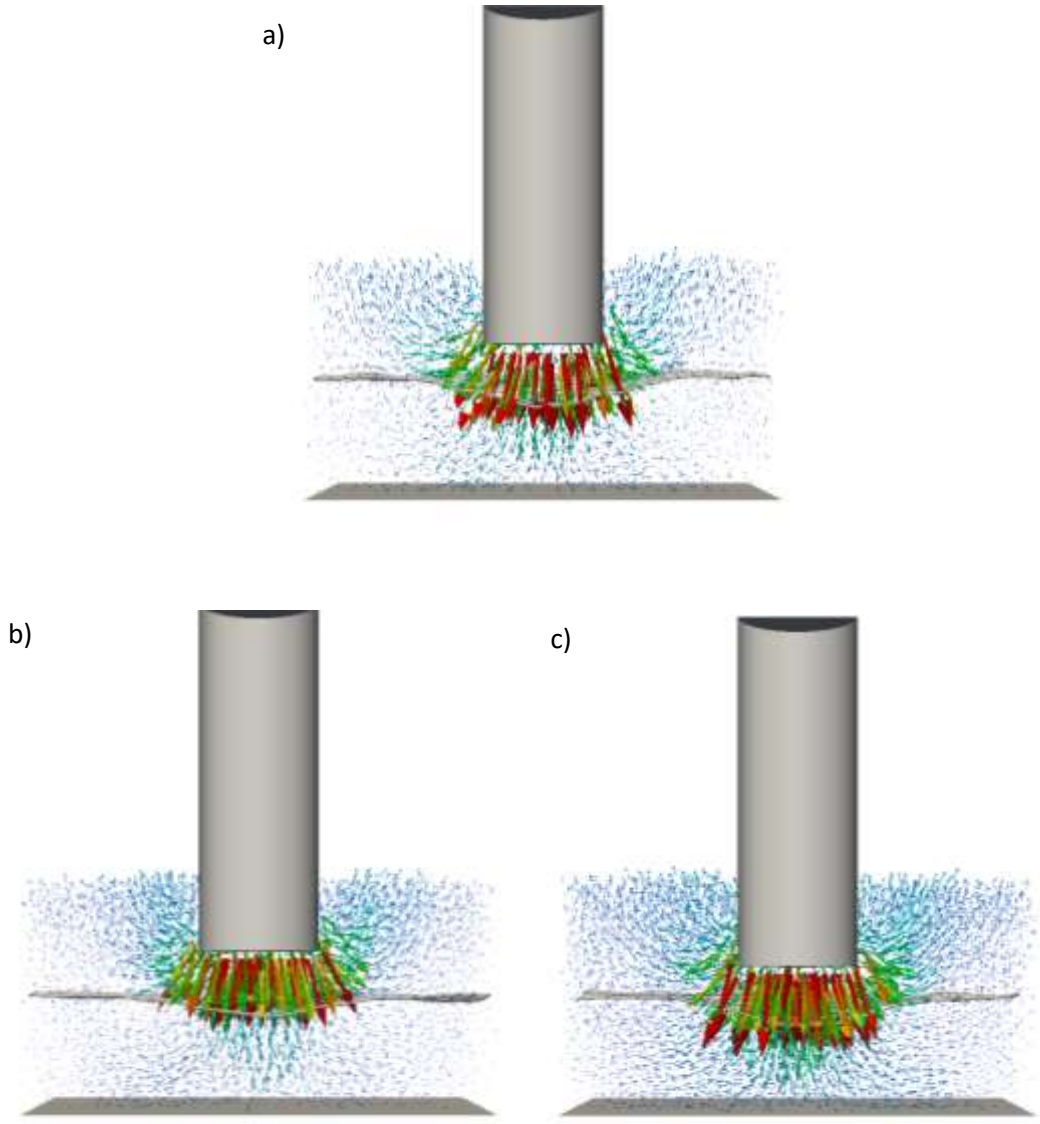

Figure 6-18 - Effect of gg opening size (a) 12.5 mm GG, 15 mm particles, (b) 12.5 mm GG, 12.5 mm particles, (c) 25 mm GG, 12.5 mm particles

Figure 6-18 (a), (b) and (c) represent cases 1, 2 and 3 respectively. Case 2 (Figure 6-18b), clearly has lower magnitudes of larger displacements (fewer red arrows). Case 3 (Figure 6-18c), with the 25-mm geogrid, is allowing more particle displacements under the geogrid, owing to its larger opening size. Meanwhile, in Case 1 (Figure 6-18a), there is a larger depression trough over the geogrid. This is potentially because the larger sized particles are rolling over the geogrid upon being restricted to displace in the vertical downward direction. To demonstrate this effect, the lateral displacements for each particle in the specimen is plotted against depth in Figure 6-19. The gap in the plot at the geogrid elevation (~0.11) m and excessive lateral displacements immediately above the geogrid indicates that the geogrid is acting as a barrier and not mobilizing optimal interlocking.

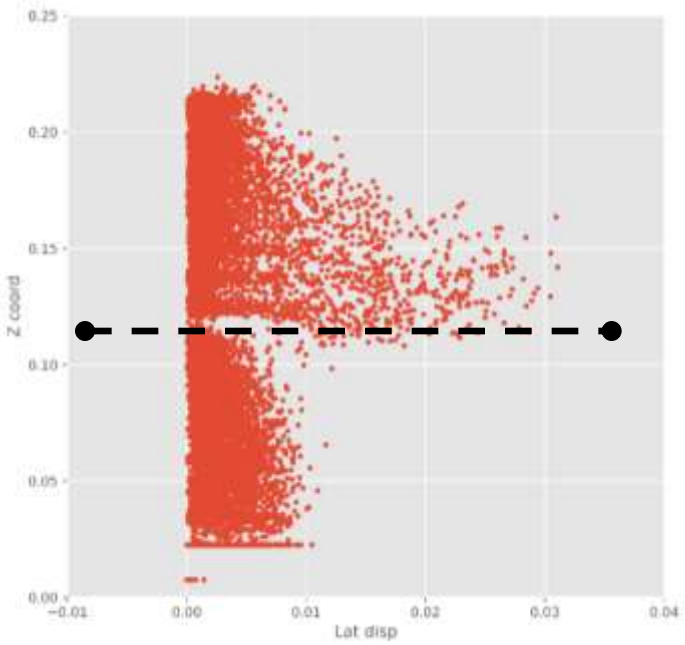

Figure 6-19 - Lack of penetration with 12.5 mm geogrid and 15 mm particles showing importance of opening size

6.5.4 Effect of Geogrid Location

The placement location of the geogrid has been an extensively studied topic over the decades. The consensus from literature is that for thin aggregate layers (approximately 6 inches) or over soft subgrades, geogrids at the bottom of the base layer are optimal. In case of thicker base course layers, including over stiff subgrades, geogrids placed closer mid-height are optimal. The specimen thickness used in the current simulation study is 0.2 m (8 inch), which is an intermediate thickness for a real pavement. At this point, it is clear that the lateral deformations are dependent on applied stress.

Test specimens were generated with geogrid placed at mid-height, upper-third and lower-third of the total thickness and the loading sequence was conducted. Figure 6-20 shows the rutting curves for all three cases along with the unstabilized rutting curve. The specimen with geogrid placed at one-third thickness from top shows significantly improved rutting performance, followed by mid-height and lower-third locations. In general, geogrids places near the surface allows engagement with upper particles which are prone to displace the earliest.

To investigate this further, the lateral displacement profiles for specimens with geogrids at depths H/2, H/3 and 2H/3, where H is the thickness of the specimen, were generated (after 300 cycles) and presented in Figure 6-21, along with the unstabilized specimen. These results clearly indicate the impact of the geogrid on lateral displacements. At a depth of H/3, the geogrid is in the middle of the peak lateral displacement zone and limiting excessive spreading. Thus, the structural integrity of the layer is preserved from an early stage. From the geogrid point of view, it experiences greater stresses at the H/3

location and transmits it laterally through its ribs. As a result of it experiencing larger forces closer to the surface, the geogrid at H/3 also shows larger vertical settlement compared to geogrid at H/2. This is evident from Figure 6-22, which plots the positions of the geogrid nodes across the specimen at end of the respective tests.

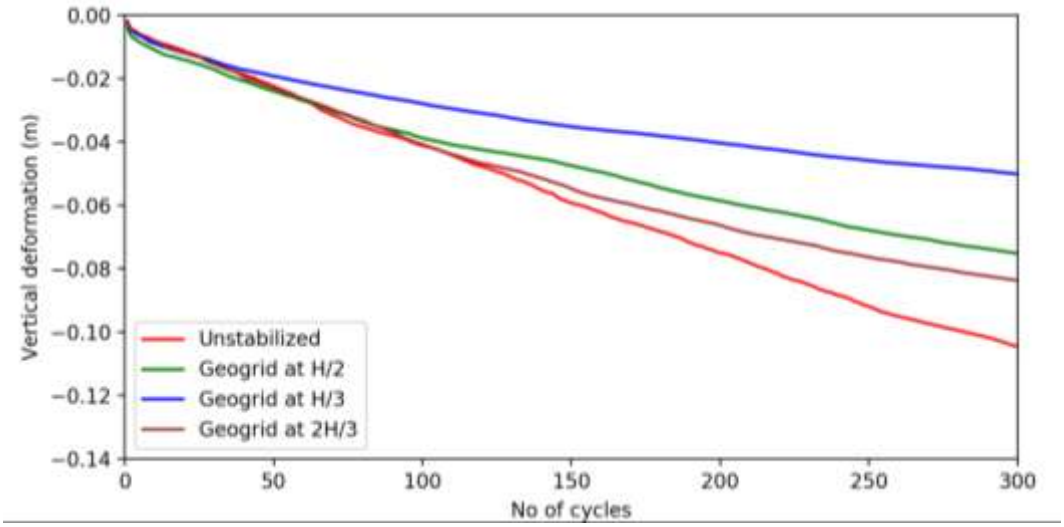

Figure 6-20 - Rutting curves for unstabilized and stabilized specimens with geogrid at depths 2H/3, H/2 and H/3

In summary, the optimal placement of the geogrid is where it is close to the surface so as to minimize lateral spreading, while also deep enough so that it can form an interlocked matrix. The simulations presented here are an idealized scenario, where specimens are generated and compacted to follow a specific set of instructions. In reality, the placement and compaction of the base course is a much less controlled process, involving heavy equipment driving over the later to achieve a design criteria. In such conditions, geogrids placed very close to the surface are at the risk of being exposed to the surface, preventing the formation an aggregate sandwich around the geogrid. Therefore, in

practice, geogrids are typically placed at the mid-height of the base layer or near the bottom. This is also convenient from compaction standpoint to divide base course into two equal-thickness lifts or one full-thickness lift respectively.

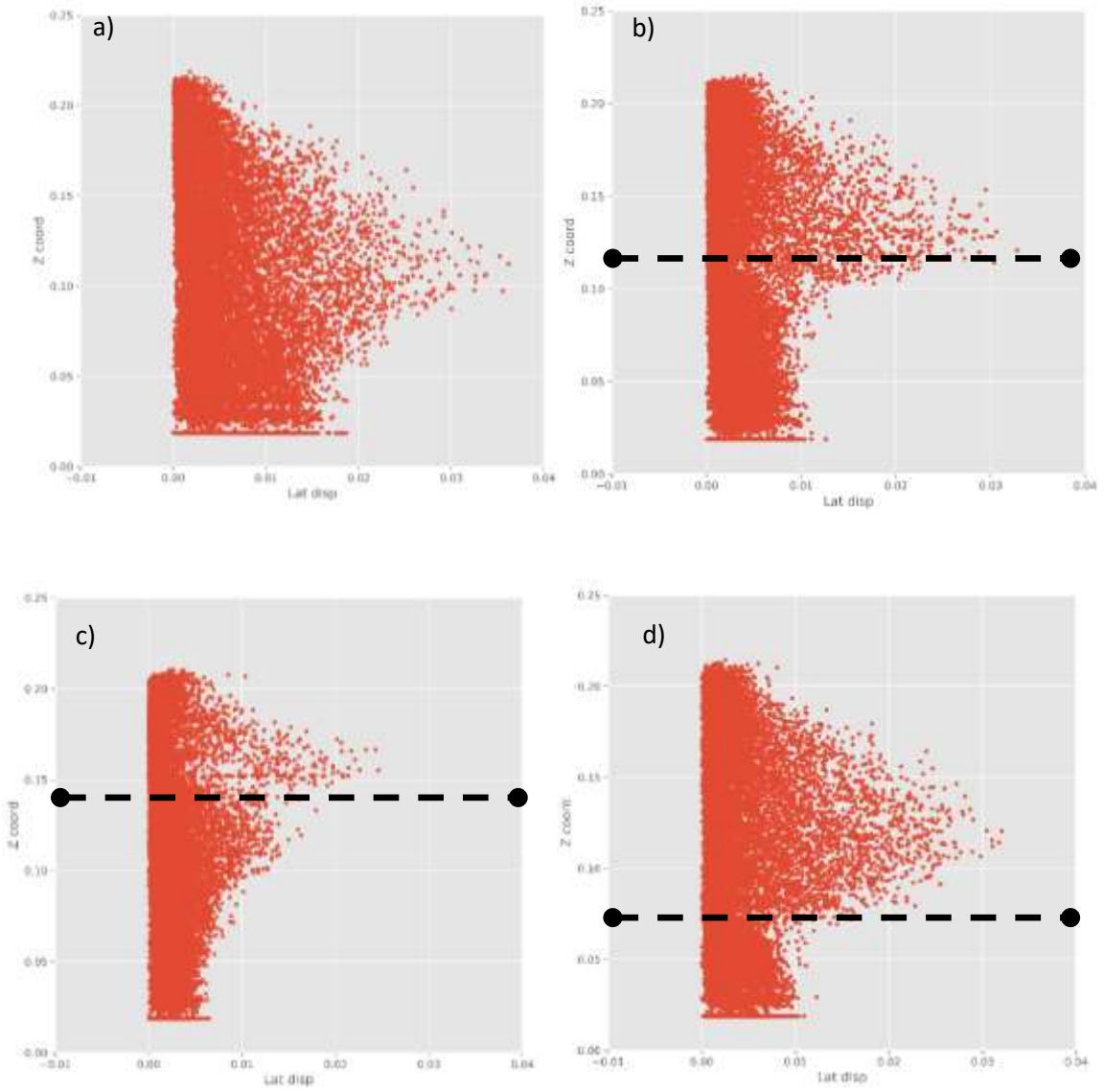

Figure 6-21 - Lateral spreading for stabilized specimens with geogrid at depths (a) unstabilized, (b) H/2, (c) H/3 and (d) 2H/3 at 300 cycles

a)

b)

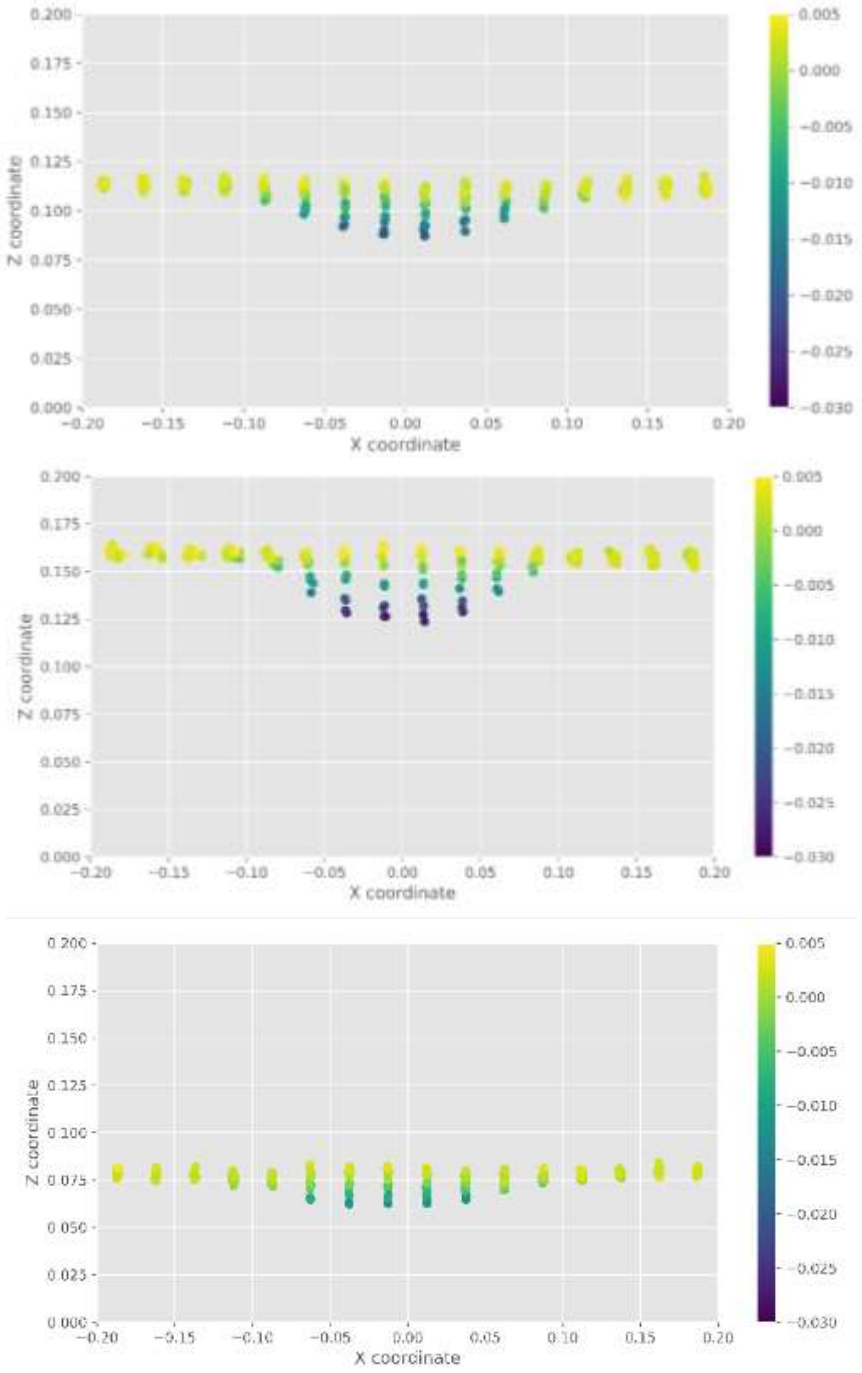

Figure 6-22 - GG node vertical displacement at 300 loading cycles for (a) location H/2, (b) location H/3 and (b) location 2H/3 from surface

As stated previously in Chapter 5, placing the geogrid at location H/3 poses practical concerns like risking grid exposure or grid damage under moving heavy

equipment during construction. The key requirement for the functioning of a geogrid is to have sufficient aggregate on top (preferably both sides), and any scenario that risks that is should be carefully evaluated.

6.5.5 Effect of Grid Stiffness

Grid stiffness is another important parameter that was evaluated using the discrete element model. In theory, greater stiffness would transfer a bigger proportion of the vertical load into lateral tensile forces, thereby reducing vertical deformations.

For the comparative study using simulations, a grid specimen with much greater Young's modulus and out-of-plane stiffness was generated to simulate a steel grid. This test was only run for 200 cycles as the computational time significantly increased. The displacement visualizations at the end of 200 cycles for a geogrid of 25-mm opening size and a steel grid of same geometry, with 12.5-mm particles is shown in Figure 6-23. None of the nodes of the stiff grid show any vertical deformations, while the geogrid is already beginning to form a depression trough. Additionally, since the stiff grid doesn't deform to adjust to the particles in its vicinity, it provides a stiff platform for the overlying particles to resist the applied loads. Therefore, the influence of the stiff grid is noticed very early in the test, starting at about 50 cycles as evident from the rutting curves in Figure 6-24.

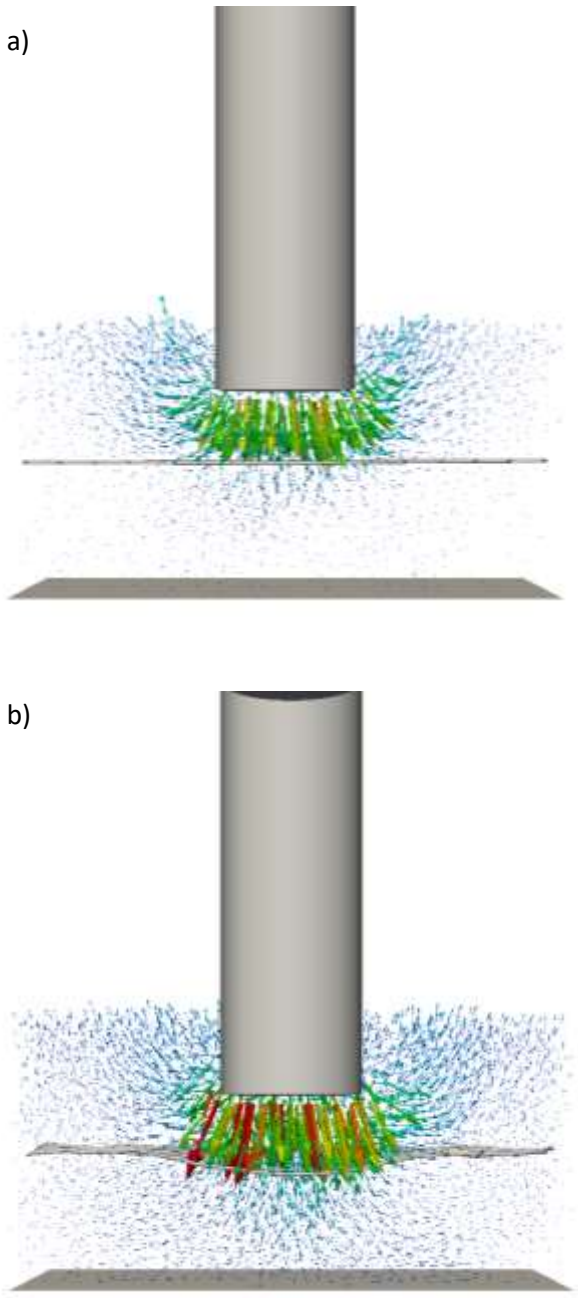

Figure 6-23 - Displacement vector at 200 cycles with a) high stiffness grid and b) geogrid

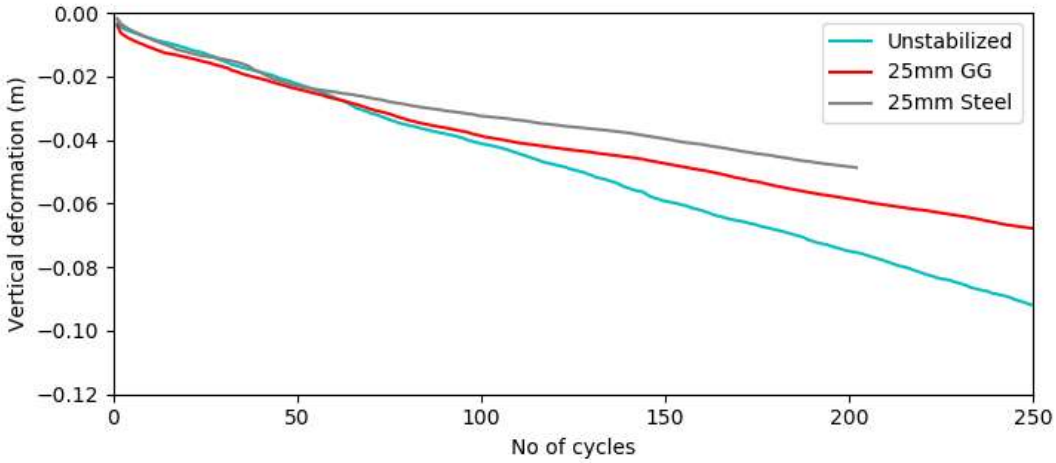

Figure 6-24 - Rutting performance of specimens stabilized with geogrids and stiffer grids

The main benefit is observed with lateral displacement profiles presented in Figure 6-25. Owing to the inflexibility of the stiffer grid, the particles underneath the grid experience much lower lateral deformations compared to the standard geogrid case. Therefore, over the longer term, the stiffer grid would show better pavement health under channelized traffic. Additionally, the stiff grid in Figure 6-25(b) shows lower displacements above the grid, between 0.1m to 0.15m compared to the geogrid in Figure 6-25(a).

In summary, the numerical simulations show that stiffer grids show improved rutting performance than less stiff grid. However, stiff grids, especially steel grids are more expensive and prone to deterioration from chemicals and moisture. In some cases, the high grid stiffness shows a tendency to uplift during construction causing a separation between upper and lower aggregate lifts.

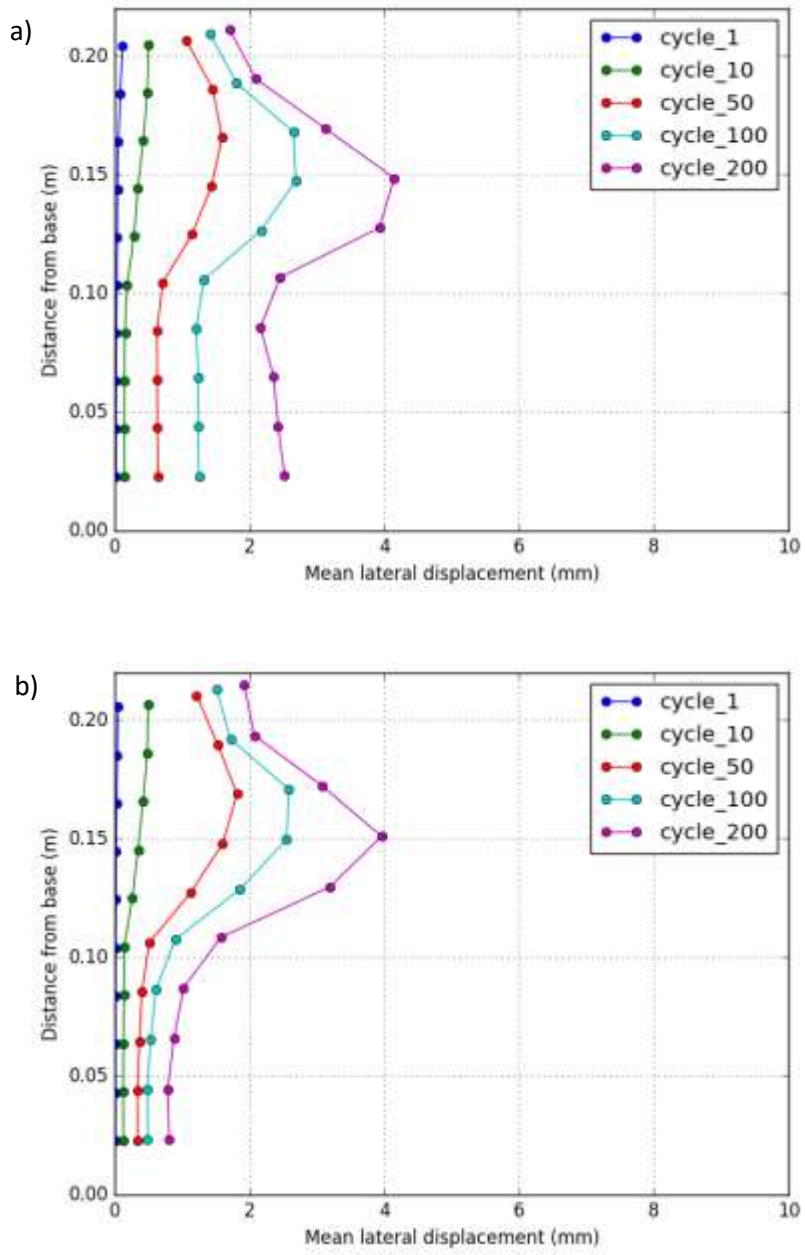

Figure 6-25 - Lateral displacement comparison of (a) geogrid versus (b) stiff grid

6.5.6 Effect of multiple layers of geogrid

For base course layers that are greater than 10 inches or when aggregate quality is poor, two layers of geogrid might be beneficial in limiting surface rutting. A specimen was

generated to include geogrids placed at mid-height (H/2) and at three-quarter (3H/4) times the thickness from the top. The corresponding rutting curves are presented in Figure 6-26 and the specimen cross-sections showing geogrids, along with particle displacements are shown in Figure 6-27. For the first 300 cycles of the simulations, both cases showed exactly the same rutting behaviour. The effect of the lower geogrid was apparent in the latter half of the test after 300 cycles, when particles in its vicinity were being displaced. The rutting curves indicate the lower geogrid contributes towards the longer-term performance of the pavement.

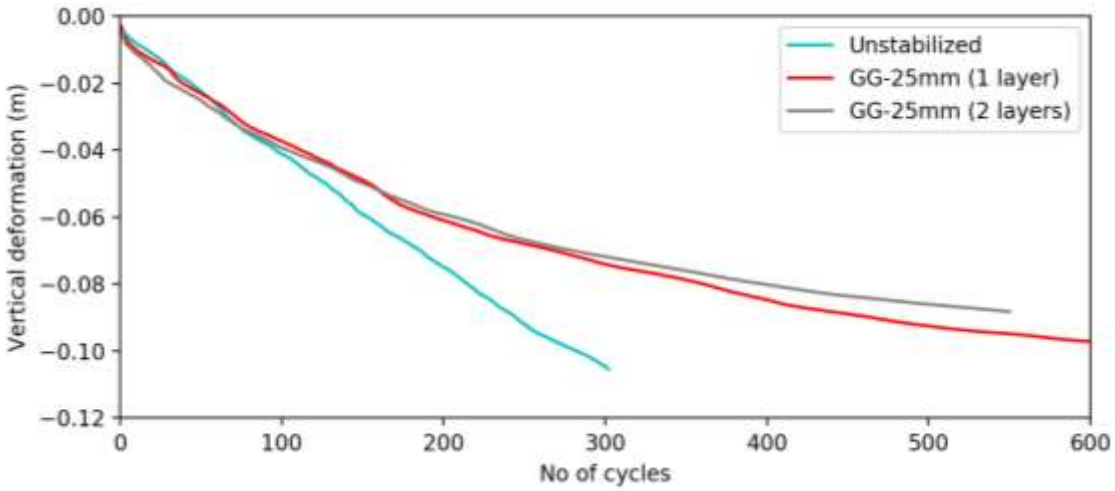

Figure 6-26 - Rutting with 1 layer geogrid at 0.5H versus 2 layers of geogrid at 0.5H and 0.75H

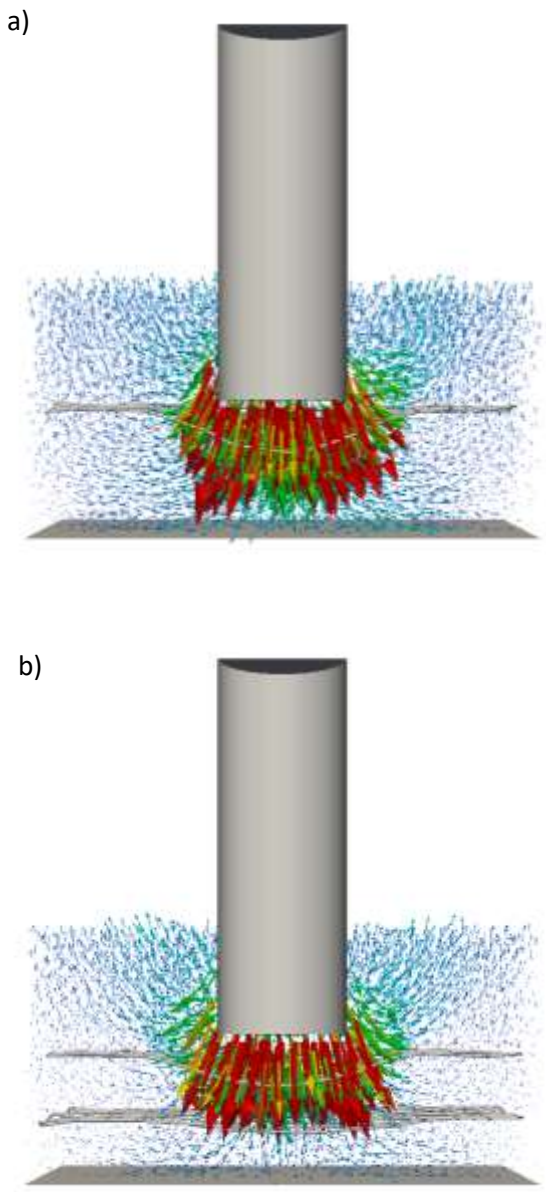

Figure 6-27 - Displacement diagram of specimen with (a) 1 geogrid and (b) 2 geogrid layers

6.5.7 Effect of morphology using rolling resistance

Incorporating rolling resistance in defining the particle characteristics provides a simple and effective way to simulate the interlocking behaviour between aggregates. This,

in turn is a measure of the quality of the aggregates, i.e., granular material without rolling resistance could represent more rounded particles which tend not to interlock, while material with an increased rolling resistance could represent angular aggregates which interlock amongst each other to a greater extent. The rolling resistance was defined using the following two parameters in the CohFrictMat material model: the dimensionless rolling stiffness, α_{kr} (alpha-kr) and the dimensionless rolling strength, η_{roll} (eta-roll). For all previous simulations, α_{kr} was set to 0 (no rolling resistance) and η_{roll} was set to -1, which represents elastic rolling moments.

To understand the effect of rolling resistance on rutting behaviour, Figure 6-28 presents the cross-section of two specimens at the end of 300 cycles. In Figure 6-28 (a), the rolling stiffness and rolling strength parameters both were set to 0.05, while in Figure 6-28 (b), these parameters were set to 0.05 and 0.1. There is a significant difference in the performance of the two specimens in terms of penetration depth of the loading cylinder and the particle rotations around the tip of the cylinder.

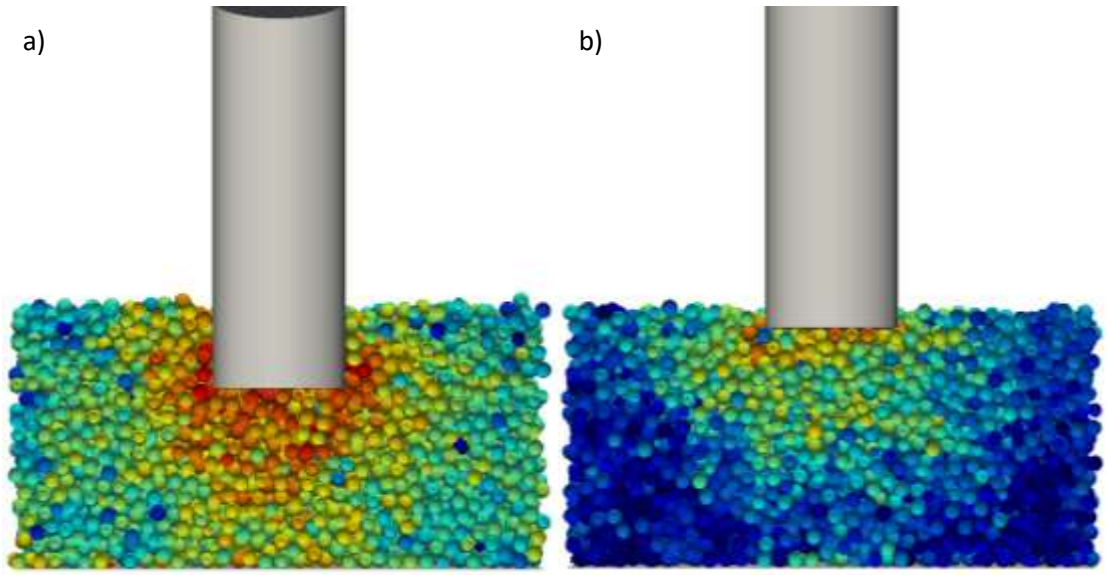

Figure 6-28 - Specimen profiles showing the effect of rolling strength with (a) η_{roll} = 0.05 and (b) η_{roll} = 0.1

As noted in Chapter 2, rutting can generally be categorized into three modes: base layer compaction caused by insufficient compaction (mode 0), local shearing and lateral flow caused by poor quality of aggregates (mode 1) and macro-pavement rutting generally with good quality base course over soft subgrades (mode 2). Mode 2 is characterized by wider displacement trough, with both base and subgrade layers rutting approximately equally. Applying this framework to the current simulations, all cases without rolling resistance are poor-quality aggregates and show mode 1 behavior, where there is lateral flow and extensive local particle rotations and displacements. The cases presented in Figure 6-28 are better quality aggregates, especially that shown in Figure 6-28 (b), which represents a combination of modes 1 and 2. Figure 6-29 below shows another specimen generated with rolling stiffness and strength parameters set to 0.005 and 0.8 respectively at the end of 500 loading cycles. A clear displacement trough can be observed that is wider

than the previous cases, especially ones without rolling resistance. The low value of rolling stiffness induced excessive rutting, in spite of the high rolling strength, while the rolling strength parameter seems to control the Mode 2 rutting behavior.

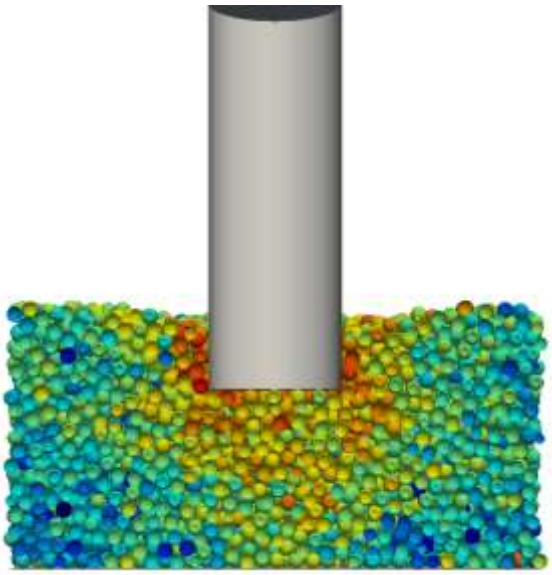

Figure 6-29 - Specimen showing mode-II rutting after 500 loading cycles

Figure 6-30 presents the rutting curves corresponding to a few tests with varying rolling resistance settings. The rolling strength parameter has a huge influence on the extent of rutting. A value of $\eta_{roll} = 0.05$ shows about half as much rutting as specimens without any rolling resistance. For $\eta_{roll} = 0.1$, the rutting is very low.

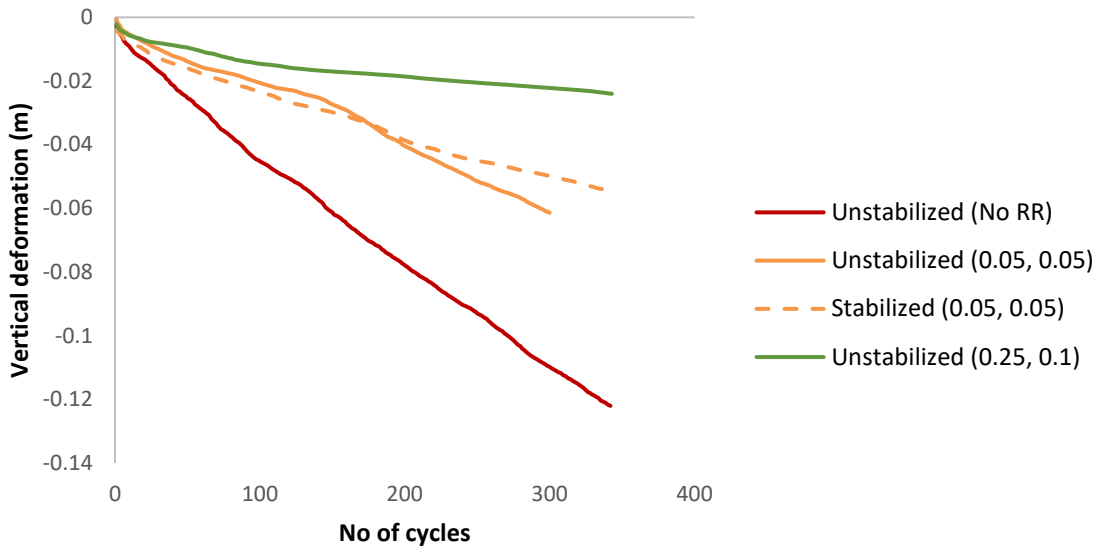

Figure 6-30 – Comparison of rutting curves for specimens with varying settings of rolling resistance (parenthesis represents values for rolling stiffness, α_{kr} and rolling strength, η_{roll})

It was noted in Chapter 5 that the angular QA material showed a bilinear shape to the rutting curves compared to RA material. In Figure 6-30, the high-quality specimen generated with $\eta_{roll} = 0.1$, also shows a bi-linear shape. Figure 6-31 shows another rutting curve generated with specimen with $\alpha_{kr} = 0.5$, $\eta_{roll} = 0.1$, which shows a similar shape. In addition, it is worth noting that all trajectories with specimens with rolling resistance are unique from the beginning, while the specimens without rolling resistance (Figure 6-16, 6-20) showed overlapping rutting curves in the initial stage of the test.

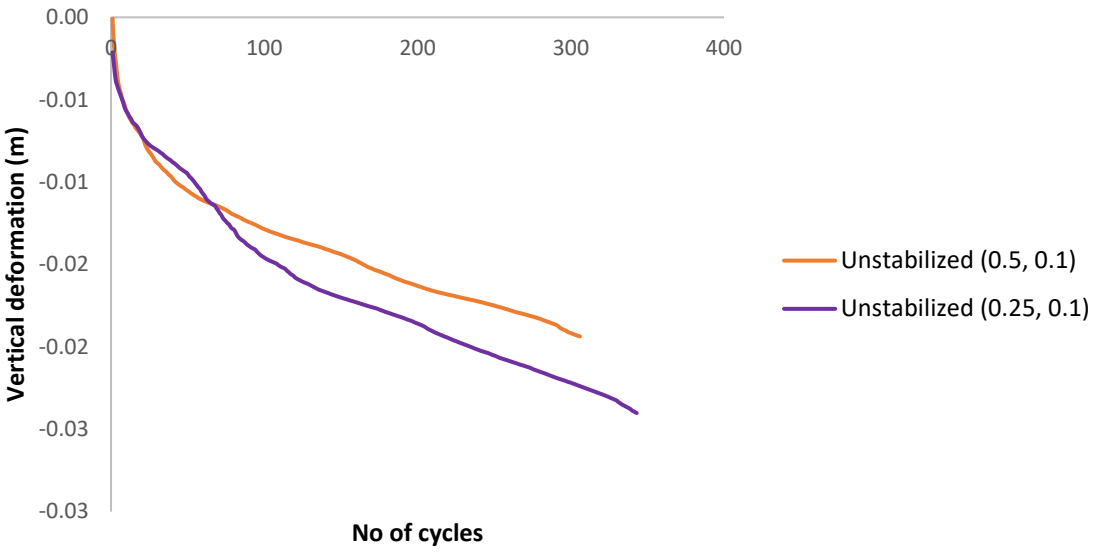

Figure 6-31 - Rutting curves for specimens with high rolling strength showing bilinear shape typical of angular aggregates (parenthesis represents values for rolling stiffness, α_{kr} and rolling strength, η_{roll})

As expected from the reduced surface rutting with introduction of rolling resistance, the lateral displacements of the particles will also be lower than the cases without rolling resistance. A comparison of the mean lateral displacements for unstabilized and stabilized specimens (with a 25-mm geogrid) with and without rolling resistance is shown in Figures 6-32 and 6-33. An interesting observation can be made from the stabilized specimens in Figure 6-33, where both specimens are stabilized with a 25-mm geogrid. The peak lateral displacement without rolling resistance is at elevation 0.125 m, which is about 15 mm from the geogrid. With rolling resistance, the peak lateral displacement occurs at 0.15 m, which is 40 mm from the geogrid location. This indicates that the improved characteristics of the aggregate particles are now able to transmit the confinement effect of geogrid to a greater

distance above the geogrid. In other words, the particles with rolling resistance exhibit a greater influence zone with the geogrid.

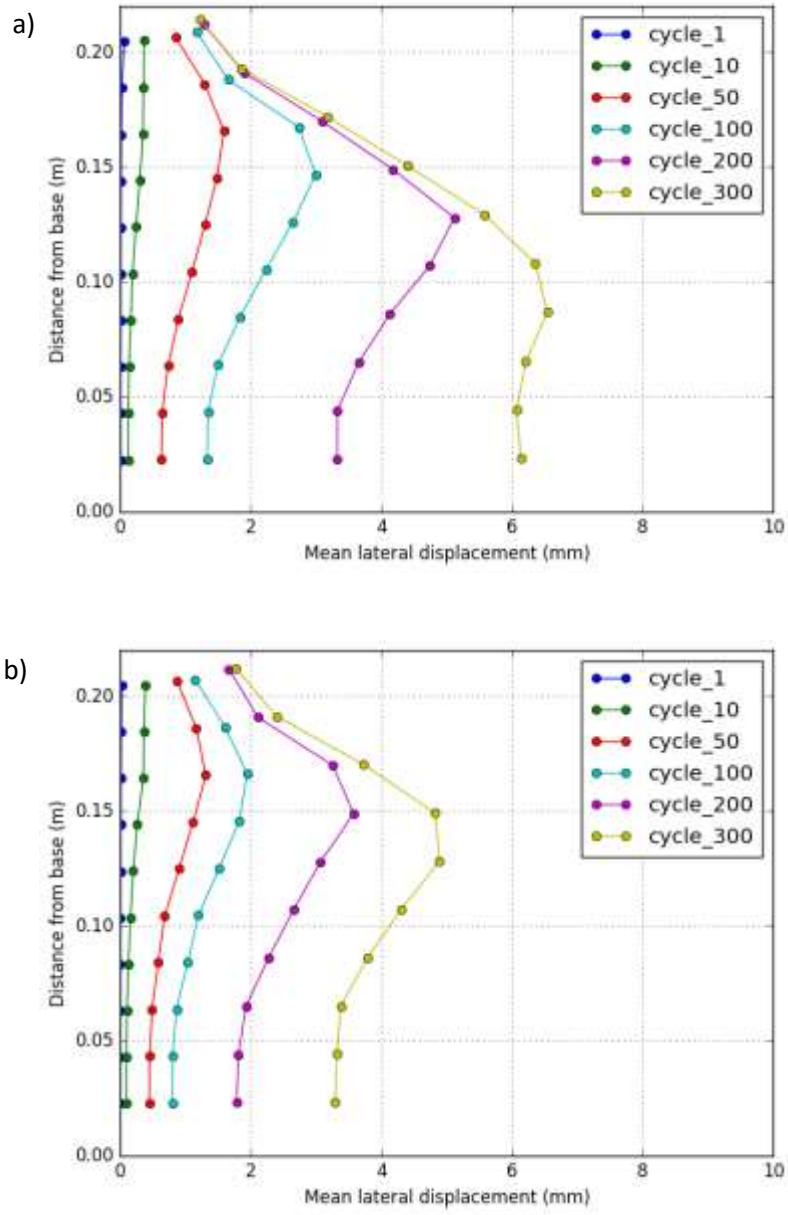

Figure 6-32 - Plots of mean lateral displacements across specimen thickness for unstabilized specimens (a) without rolling resistance and (b) with rolling resistance

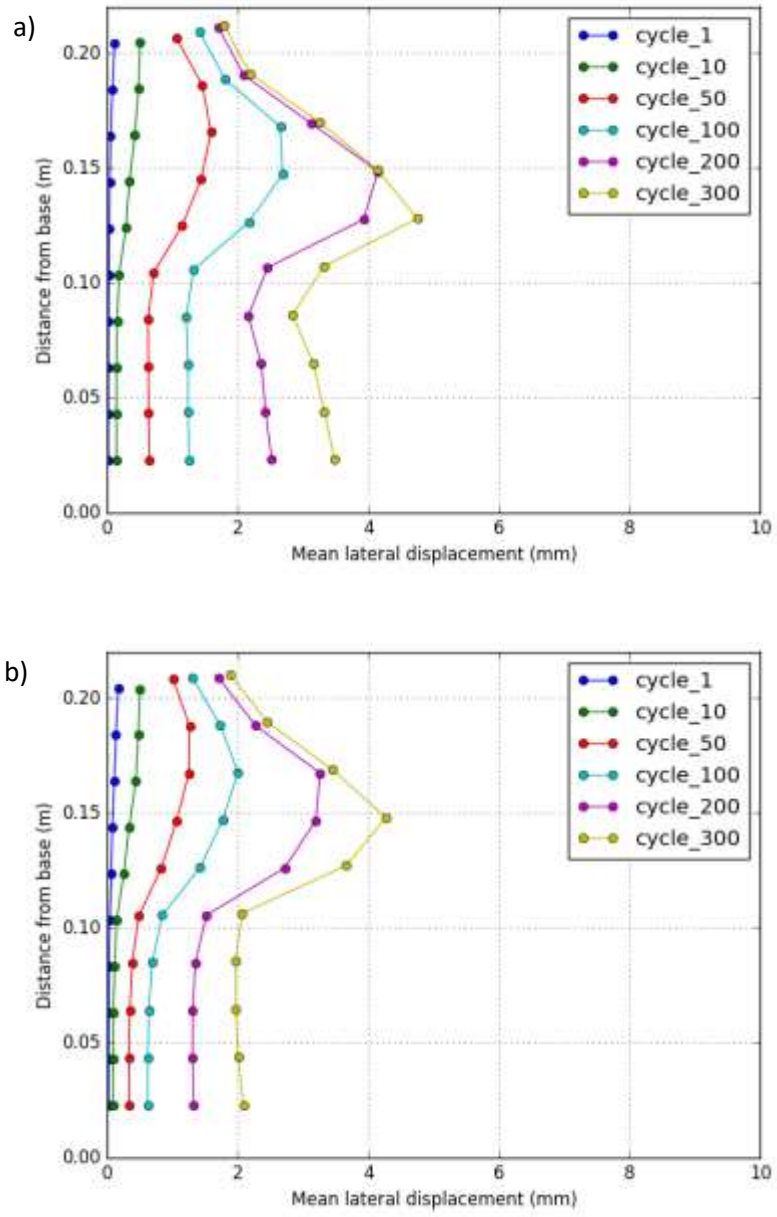

Figure 6-33 - Plots of mean lateral displacements across specimen thickness for stabilized specimens (a) without rolling resistance and (b) with rolling resistance

CHAPTER 7. CONCLUSIONS AND RECOMMENDATIONS FOR FURTHER STUDIES

In this research, various aspects relating to the mechanisms and behavior of unbound materials in flexible pavements were assessed and quantified. The ultimate objective is to assist in improving pavement design guidelines to ensure a high quality of road infrastructure across the county. To achieve this, a standardized test procedure for establishing benchmarks and formulation of performance metrics that capture internal mechanisms is required. While there are existing standardized test procedures for measuring resilient modulus, there has not been a standard methodology for measuring the permanent deformation in pavement materials. Moreover, the performance evaluation of a composite pavement system, that comprises of a base layer, subgrade as well as geosynthetic has been particularly challenging. Often, such evaluations have been conducted using full-scale tests, which are often time consuming and expensive.

7.1 Conclusions from research study

The bench-scale pavement simulation apparatus developed as part of this study facilitates measurement of permanent deformation induced by a cyclic rolling-wheel load on scaled-down pavement specimens. This test procedure facilitates rapid testing rates to assess the relative rutting behavior under various operational and design conditions, requires low quantities of materials and allows a high degree of control over specimen properties. Additionally, the system closely simulates field conditions like lateral restraint of geogrids and rotating wheel loads. Incorporation of stress sensors also allows monitoring

stresses from within specimen. These benefits can be concisely represented as shown in Figure 7-1, in relation to alternate modes of pavement simulation methodologies. Chapter 3 in this thesis presents the design and operational details of the equipment, which can easily be scaled as per requirements and replicated in other testing laboratories.

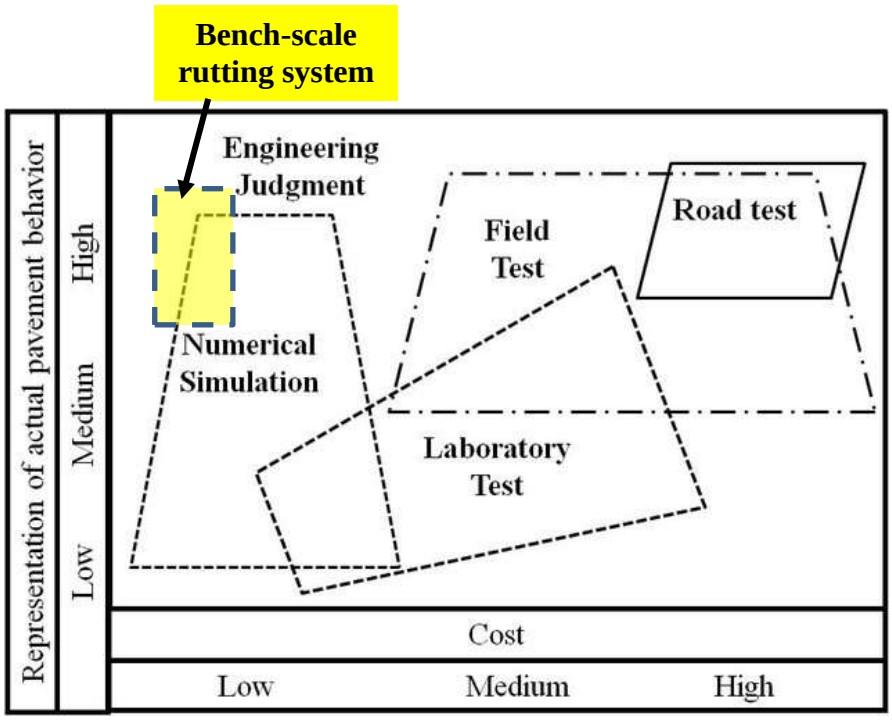

Figure 7-1 Comparison of bench-scale rutting system with various techniques used for pavement performance assessments (adapted from Hugo et al, 1991)

In Chapter 4, the effect of subgrade stiffness and geosynthetic stabilization on the pavement specimen performance was evaluated. Validation tests were conducted to establish repeatability of rutting results, absence of boundary stresses and standardize the testing procedure involving specimen preparation and data processing. Subgrade stiffness was characterized by its CBR value and moisture content.

- All rutting curves showed the expected exponential behavior, with a significant portion of the rutting occurring in the first 100 loading cycles followed by a plateau. The Lytton and Tseng rutting model was used to perfectly fit the rutting curves. The worst-performing tests were with the unstabilized specimen over subgrade CBR below 2.5.
- For all three soils, decreasing the subgrade CBR from 14 to 1.5 significantly increased the rutting deformations by at-least 3.5 times from approximately 0.1 inch to greater than 0.35 inches after 250 loading cycles. The base layer thickness was approximately 1.2 inches.
- Rutting over stiff subgrades in all test-cases and soft subgrades for stabilized (geotextile and all four geogrids) cases were within the allowable 30% axial permanent strain for the 1-inch base layer, which is considered acceptable rutting.

The effect of geosynthetic stabilization was negligible at high subgrade-stiffness conditions, but clearly evident at low-stiffness conditions. For all geogrid-stabilized cases, the observed rutting was at-least 28% lower than the unstabilized case, while the geotextile achieved a minimum rut reduction of 14 %.

- The three soils were similar in their properties, and generally showed similar rutting characteristics. Gordon Co soil performed slightly better than the other two soils at low stiffness conditions, showing an unstabilized rutting of 0.35 inches compared to 0.48 and 0.44 inches with Coweta and Hall Co soils respectively, after 250 loading cycles.

- Stress measurements were very beneficial in gaining more insights to supplement surface rutting measurements. In high stiffness conditions, stresses measured 1-inch into the subgrade was significantly lower (about 5 psi) than the top of the subgrade, irrespective of the stabilization condition. However, at lower subgrade stiffness's, the unstabilized tests showed a reduction of less than 1psi (more than 4 psi in subgrade), while the stabilized continued to showed significant reductions that reduced the stress to below 2 psi. GG125 was an exception to this pattern but can be reasoned based on its very low stiffness.

In summary, the test results clearly established the benefits of geosynthetics in soft subgrade conditions. Moreover, by running rutting tests with geogrids of different opening sizes and stiffnesses, a comparison of the influence of these factors could be made. The importance of stiffness was illustrated by the lack of stress redistribution by GG125, which had the smallest opening size and least stiffness. The other geogrids performed comparably well and established the advantage of good interlocking towards stabilization. On the other hand, while the geotextile showed slightly increased rutting, it was efficient in stress redistribution and performed extremely well as a separator.

The above study had a wide range of interplaying variables like subgrade stiffness, aggregate material water content and gradation and geometric and strength characteristics of geogrids etc. Therefore, in Chapter 5, the goal was to enhance the understanding of the behaviour of geogrid-stabilized aggregate systems in a controlled manner and focussing only on the influence of particle shape, grid geometry and grid location on the rutting behaviour of the aggregate base layer. Rutting tests were conducted the rough-angular quarry-aggregate (QA) and the smooth-rounded river-aggregate (RA) materials showed

interesting behaviour providing insights into particle-level mechanisms. Two sets of biaxial grids, i.e. steel grids and geogrids were used to asses any potential effects of stiffness and/or establish repeatability of effects of opening size, placement location etc.

The following conclusions were drawn from the results of the experiments.

- The degree of rutting was observed to reduce when the grids were placed closer to the surface of the base layer. This trend was consistent through all the aggregate-steel grid combinations. This observation matches with several other studies that recommend placement of geogrid closer to surface for poor quality aggregates. Since these aggregates tend to shear locally, the grid is effective in arresting excessive deformations before the shear displacements take place.
- Further, the smooth-rounded particles of the RA consistently showed higher rutting tendencies as compared to the rough-angular particles of the QA. With increasing particle roundness and sphericity, rutting depths were observed to increase.
- Among the four steel grids used in the study, the steel grid with opening size 0.75 inches (19.1 mm) offered the highest interlocking potential and lowest rutting with the aggregate particles, whose size ranged between 0.25 inch-0.375 inch (9.35 mm- 9.5 mm). The steel grid with 0.25-inch (6.35 mm) opening showed high rutting depths owing to its small opening size relative to particle diameters.
- By stabilizing the base layer with grid (SG3), the RA material showed rut reductions between 12% and 65% compared to the unstabilized case for various

grid locations, while the QA material showed reductions between 32% and 75%. These observations prove that the efficiency of grid stabilization and overall rutting behaviour is affected by particle morphology. Both aggregate materials showed the most improvement in rutting with the 0.75-inch steel grid, indicating particle size, and not shape, should determine the choice of grid to be used.

- Tests with geogrids reiterated the optimal opening size range of 0.50-0.75 inches, similar to results with steel grids. Interestingly, geogrids did not show any influence on surface rutting when placed at the bottom of the aggregate layer. However, at depth of 2H/3 the rutting performance was improved, even surpassing steel grids with the 0.25 inch grid.

Ultimately, while the test results obtained from the bench scale apparatus may not provide absolute values for practical design applications, this study showed that it can be very useful to understand the mechanisms at the particle-scale, which is difficult with larger specimens.

In Chapter 6, an extensive suite of DEM simulations was conducted to quantify the influence of the previously mentioned variables, by focussing on the particles. The goal of this study was to visualize internal mechanisms between particles and geogrid, to tie back into the findings from the previous chapters. Simulations were run with aggregate particles without any rolling resistance that approximately represented the rounded aggregate mix used in Chapter 5. Further, by incorporating rolling resistance, the resulting behaviour was observed to match the angular quarry aggregate. The following general observations were made from the simulations.

- For specimens that were stabilized with a geogrid, the rutting curve initially coincided with the unstabilized rutting curve. Once the particles which were under the confinement effects of the geogrid were beginning to get affected from the rearrangements under the applied loads, the rutting curve diverged at various stages of the test. At lower applied stresses like 70 kPa, this divergence happened much later than with higher stresses like 190 kPa. This behaviour resembles the RA material.
- By observing the lateral displacement plots at different stages of the test, the extent of influence of the geogrid could be deduced. For a stabilized specimen, the lateral displacement at a certain distance from the geogrid was observed to be lower than that for the unstabilized specimen at the same distance. This reduction represents the primary influence of the geogrid resulting from interlocking, and subsequently alters the surface rutting behaviour. Moreover, by comparing the lateral displacement plots of 25-mm and 37-mm geogrid, the superior performance of the 25-mm geogrid could be inferred.
- The rut depths for both, stabilized and unstabilized specimens were linearly dependent on the applied loading stress. The ratio of unstabilized to stabilized depths increases from 1.0 at 70 kPa to 1.17, 1.36 and 1.45 at 100, 140 and 190 kPa respectively.
- Among the combinations of geogrid opening sizes and aggregate particle sizes considered, the ratio of 1:1 showed the least rutting. However, for graded aggregate mixes, this geogrid opening size to aggregate mean

diameter is likely closer to 2:1, as observed with rutting experiments. More simulations with graded aggregate material would shed light on this aspect.

- Geogrid placed closer to surface at a depth of one-third the layer thickness showed significantly lesser surface rutting, but more geogrid deformation compared to lower placement locations. However, this poses challenges in the field regarding inadequate aggregate cover during construction. Specimens with two layers of geogrids tend to show benefits over longer term. Also, stiff grid showed slightly better rutting performance than a geogrid. All these design scenarios are best tested in should be considered in conjunction with real-world implications like constructability, durability and performance.
- Incorporating rolling resistance into particle interactions had significant implications on the behaviour of the specimens. Rutting tendency drastically reduced with introduction of bending stiffness and strength. Moreover, the improved interlocking showed indications of increased confinement zone over the geogrid based on the lateral displacement plots. Also, the rutting curves were observed to match the rutting curves obtained with the QA material in Chapter 5, with regards to the shape and trajectories.

This study, ultimately, enables a better-informed design process for incorporating geogrids into pavements, leading to more economical and sustainable use of geo-materials.

7.2 Recommendations for further studies

This section presents a collection of topics that were either briefly investigated or hold promise as topics for consideration for future studies. Individually and collectively, they could produce interesting findings ranging from improved pavement design guidelines to investigating the mechanisms behind the counter-intuitive slushing process in inverted-base pavement construction.

Firstly, the pavement specimens that were investigated in this study were unpaved specimens focusing on the behavior of the unbound granular base layer and subgrade. The stress applied over the top of the base layer was equal to a value that is typically transmitted through the asphalt layer in full-scale pavements. However, an asphalt layer could be included in bench-scale specimens (or an equivalent layer in terms of stiffness) to investigate any other auxiliary benefits of the layer. For example, the area of stress bulb at the bottom of the asphalt layer would be larger which could cause lateral spreading over a wider area in the base layer.

Secondly, the experiments conducted in the study utilized geogrids (steel and polymer) that are produced using different manufacturing processes. For example, steel grids are wires welded over each other in a biaxial pattern, which polymer geogrids involve a punching and stretching sequence of polymer sheets to obtain the desired geometry. The effect that these manufacturing processes could have on the performance of the products at the stress levels that they typically experience in full-scale pavement systems, could be useful in designing the stiffness and geometry of the grids. 3D printed geogrids also represent a novel mode of manufacturing geosynthetics that will be studied.

Additionally, the behavior of graded aggregate base material at different stress states could be investigated using a greater layer thickness (4-6 inches). This thicker-layer specimen could also be used to study the behavior with one and two layers of geosynthetics. Two layers of geosynthetics could further help reduce the required aggregate layer thickness or increase service life of pavements.

The DEM study presented in this study employed spherical particles, which is not observed in the real world. However, the spherical particle do closely represent rounded particles like the RA aggregates used in Chapter 5, which can be validated based on the closeness of rutting results of the two sets. Therefore, the DEM simulations do capture the fundamental frictional interactions between real aggregate particles, to further enable studying the pattern of lateral displacements and surface rutting. Further, there are multiple potential topics that could be investigated to augment the current study. These could include advanced material formulations for aggregate and subgrade layers to study layered systems or analyzing the system behavior in terms of forces rather than displacements as done in this study. For example, the study of angularity with more rigor in terms of rolling resistance or particle clumps could be conducted. This would also make the results more directly comparable with experimental results.

Additionally, the following sections enlists some additional topics that hold relevance and will be investigated in the near future.

7.2.1 Sub-layering of base layer for accurate design procedure

Many M-E based design software (AASHTOWARE) currently do not accommodate the inclusion of geogrids in the design workflow. However, the

incorporation of both, geogrids and the ME design procedure is increasing, giving rise to the need for a methodology that cohesively integrates both aspects. The underlying principle of these procedures is the Layered Elastic Theory, where the inputs for each layer include the thickness, stiffness and Poisson's ratio. Conventionally, designers have had to adjust the modulus or thickness of the stabilized-layer to account for the influence of the geosynthetic, which is often subjective or unclear. Additionally, it is now clear that the stiffness of mechanically-stabilized layer (MSL) is not the same through its cross-section.

One approach to tackle this problem is by using the DEM model like the one used in this study. By calibrating the soil and geogrid product into the model, and running a few iterations for the unstabilized stabilized cases, the influence zone for the geogrid can be determined. This enables us to sub-divide the MSL into sub-layers representing the confined zone with a higher stiffness than the unconfined-zone. This framework, as depicted in Figure 7-1, represents a more reasoned and accurate procedure to incorporate the MSL in the ME design software.

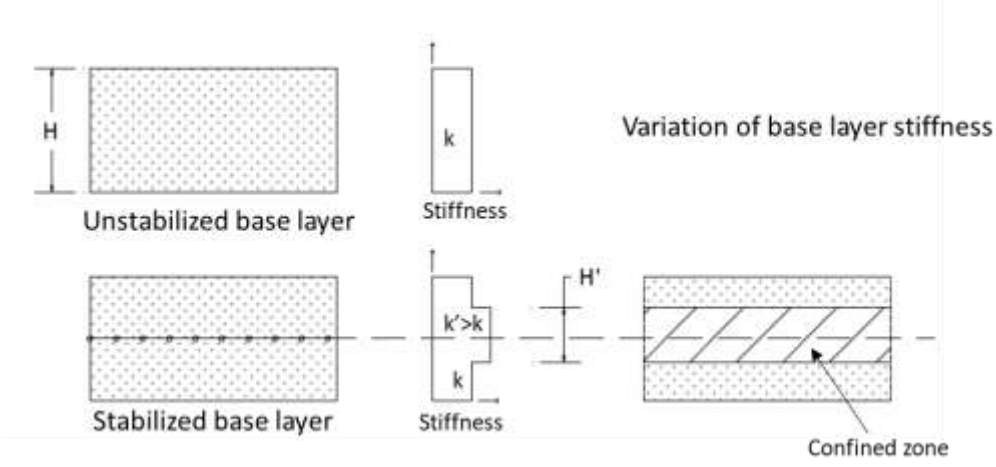

Figure 7-2 - Sub-layering of MSL based on confinement zones

This process can be potentially further refined and expedited by running a suite of simulations beforehand and building predictive models for sub-division of the MSL.

7.2.2 Assessment of performance of novel geomaterials like recycled-aggregates and geogrids of different shapes and sizes

There is increasing research being conducted targeted towards incorporating lower-quality aggregate, recycled glass or plastic or construction debris into pavements. This would lower construction costs as well as provide an avenue for disposing these waste products. In this regard, the experiments conducted in the current research study included graded aggregate base, piedmont residual subgrade soils, quarry stone, rounded pebble stone, steel and geogrids. Therefore, there is a swath of opportunities pertaining to the use of new materials in pavement construction that can be studied with the rutting apparatus. Another perspective is for innovation of geogrids, where 3D printed geogrids or prototype-scale specimens can be evaluated for their performance prior to full-scale testing.

7.2.3 Laboratory Investigation of Slushing in Inverted base pavements

The need for better utilization of unbound granular material in pavement applications is especially important considering the increased interest in new and alternate pavement technologies such as geosynthetic reinforced pavements and inverted-base pavements. This section of the study presented in Chapter 3 was aimed to supplement the field-observations made at two test sections located in Lagrange and Morgan counties in Georgia. In each of these locations, test pavement sections were constructed between 2001-2009 using a conventional flexible/rigid design methodology as well as an inverted-base design methodology. One inverted-base section in Morgan County was also constructed using the 'slushing' technique, which has been reported to further enhance the density of the packed granular base. Following multiple years of operation under heavy traffic loading and periodic pavement assessment surveys, the inverted-base sections showed superior performance relative to the conventional design sections over multiple distress metrics like cracking and rutting. Therefore, a modification of the rutting apparatus presented in Chapter 3 was used to replicate the slushing process, to quantify the changes in engineering behavior during the various stages. To this end, the work conducted in this study could serve to lay the groundwork for an extensive study on inverted base pavements in the future.

In summary, the bench-scale pavement testing system can not only be used to assess the rutting performance of a multi-layered pavement specimens but also for the simulation of construction processes for new technologies like inverted-base pavements.

REFERENCES

ASTM D1140 Standard Test Methods for Determining the Amount of Material Finer than 75-µm (No. 200) Sieve in Soils by Washing, ASTM International, West Conshohocken, PA, 2017

ASTM D1557 Standard Test Methods for Laboratory Compaction of Soil using Modified Effort (56,000 ft-lbf/ft3 (2,700 kN-m/m3)), ASTM International, West Conshohocken, PA, 2012

ASTM D1883 Standard Test Method for California Bearing Ratio (CBR) of Laboratory-Compacted Soils, ASTM International, West Conshohocken, PA, 2016

ASTM D4318-17e1 Standard Test Methods for Liquid Limit, Plastic Limit, and Plasticity Index of Soils, ASTM International, West Conshohocken, PA, 2017, https://doi.org/10.1520/D4318-17E01.

ASTM 4439-18 Standard Terminology for Geosynthetics, ASTM International, West Conshohocken, PA, 2018

ASTM D4643-17 Standard Test Method for Determination of Water Content of Soil and Rock by Microwave Oven Heating, ASTM International, West Conshohocken, PA, 2017, https://doi.org/10.1520/D4643-17.

ASTM D6637 Standard Test Method for Determining Tensile Properties of Geogrids by the Single or Multi-Rib Tensile Method, ASTM International, West Conshohocken, PA, 2015

ASTM D6913 Standard Test Methods for Particle-Size Distribution (Gradation) of Soils Using Sieve Analysis, ASTM International, West Conshohocken, PA, 2017

Abu-Farsakh, M.Y. 2009. Evaluation of the Base/Subgrade Soil under Repeated Loading: Phase 1 – Laboratory Testing and Numerical Modeling of Geogrid Reinforced Bases in Flexible Pavement, Interim Reportm LRTC Number: 736-99-1312

Al-Qadi, I.L. 2006. Pavement interlayer system mechanisms: separation reinforcement and reflective cracking control. Lecture, Chinese Society of Pavement Engineering, Taipei, Taiwan.

Al-Qadi, I.L., Dessouky, S.H., Kwon, J. and Tutumluer, E. 2008. Geogrid in Flexible Pavements: Validated Mechanism, *Transportation Research Record: Journal of the Transportation Research Board*. No 2045, 102-109.

Al-Qadi, L. L., Dessouky, S. H., & Tutumluer, E. 2008. Geogrid-reinforced low-volume flexible pavement response to loadings by various tire configurations. In *Efficient Transportation and Pavement Systems: Characterization, Mechanisms, Simulation, and Modeling - Proceedings of the 4th International Gulf Conference on Roads.* pp. 741-751.

Anderson, P. and Killeavy, M. 1989. Geotextiles and Geogrids: cost effective alternate materials for pavement design and construction. *Proceedings of Geosynthetics '89*, IFAI, Vol. 2, Sand Diego, California, USA, February 1989, pp. 353-360. (Shukla, 2002)

Applied Research Associates. 2017. Recommended Practice for Incorporating Geogrids in ME Pavement Design, Final Report Prepared for Tensar Corporation

Archer, S. and Wayne. M.H. 2012. Relevancy of Material Properties in Predicting the Performance of Geogrid-Reinforced Roadways, ASCE Geo-Congress. 1320-1329.

Bagshaw, S. A., Herrington, P. R., Kathirgamanathan, P., & Cook-Opus International Consultants LTD, S. R. 2015. Research Report 574 Geosynthetics in base course stabilization (Rep. No. 574). Wellington, NZ: NZ Transportation Agency.

Barksdale, R. D. 1972. Laboratory evaluation of rutting in base course materials. In the *Third International Conference on the Structural Design of Asphalt Pavements*, Grosvenor House, Park Lane, London, England, Sept. 11-15, 1972. (Vol. 1, No. Proceeding).

Barksdale, R.D. and Itani, S.Y. 1989. Influence of aggregate shape on base behavior, *Transportation Research Record: Journal of the Transportation Research Board*. No 1227, 173-182.

Barksdale, R.D., Brown, S.F. and Chan, F. 1989. Potential Benefits of Geosynthetics in Flexible Pavement Systems, *NCHRP Report 315*, Transportation Research Board.

Berg, R. R., Christopher, B. R., & Perkins, S. 2000. Geosynthetic reinforcement of the aggregate base/subbase courses of pavement structures (No. GMA White Paper II).

Boussinesq, J. 1885. Discussed in Theory of Elasticity

Brown, S.F., Chan, F.W.K. 1996. Reduced Rutting in Unbound Granular Pavement Layers through Improved Grading Design. Proceedings of the *Institution of Civil Engineers – Transport*. 117:1, 40-49

Brown, S.F., Kwan, J. and Thom, N.H. 2007. Identifying the key parameters that influence geogrid reinforcement of railway ballast, *Geotextiles and Geomembranes*. 25, 326-335.

Burmister, D. M. 1945. The General Theory of Stresses and Displacements in Layered Systems. *I. Journal of Applied Physics*, 16(2), 89-94. doi:10.1063/1.1707558

Chan FWK, Barksdale RD & Brown SF, 1989, Aggregate base reinforcement of unsurfaced pavements, *Geotextiles & Geomembranes*, 8:3, pp 165-189.

Chen, C., McDowell, G.R., Thom, N.H., 2012. A study of geogrid-reinforced ballast using laboratory pull-out tests and discrete element modelling. *Geomechanics and Geoengineering: an International Journal*, Vol 8-4, pp 244-253

Cuelho, E. and Perkins, S. 2009. Field investigation of geosynthetics used for subgrade stabilization (No. FHWA/MT-09-003/8193). Montana Department of Transportation

Cundall, P.A. and Strack, O.D.L. 1979. A discrete numerical model for granular assemblies, *Géotechnique*, 29, 47–65

Dawson, A. 1997. Rutting in Unsurfaced Roads – Materials and Structure Interaction Effects. International Symposium on Thin Pavements, Surface Treatments, Unbound Roads.

Dawson AR, Little PH & Brown SF, 1994, Rutting behavior in geosynthetic-reinforced unsurfaced pavements, Proc. *5th Int. Conf. Geotextiles, Geomembranes & Related Products*, Singapore, 1, pp 143-146.

FHWA Geotechnical Aspects of Pavements Reference Manual, NCHRP 1-37A, 2004

GDOT Office of Materials and Research. 2013. Georgia Department of Transportation Pavement Design Manual. Atlanta, GA: GDOT.

Giroud, J. P., Ah-Line, C., and Bonaparte, R. 1985. Design of unpaved roads and trafficked areas with geogrids, *Polymer grid reinforcement*. 116–127.

Giroud, J.P. and Noiray, L. 1981. Geotextile-reinforced unpaved roads. *Journal of Geotechnical Engineering Division*, American Society of Civil Engineers, Vol. 107, No GT9, pp. 1233-1254.

Giroud, J.P., Ah-Line, C., and Bonaparte, R. 1985. Design of unpaved roads and trafficked areas with geogrids. *Polymer Grid Reinforcement*, London, England. pp. 116-127.

Giroud, J.P. and Han, J. 2004. Design Method for Geogrid-Reinforce Unpaved Roads: Development of Design Method, Journal of Geotechnical and Geoenvironmental Engineering. Vol. 130, 775-786

Gupta, R. 2009. A study of geosynthetic reinforced flexible pavement system. Ph.D. Dissertation, submitted to The University of Texas at Austin, Texas, USA.

Han, J., Zhang, Y., Parsons, R.L.2011. Quantifying the Influence of Geosynthetics on Performance of Reinforced Granular Bases in Laboratory. *Geotechnical Journal Engineering of the SEAGS & AGSSEA*, Vol 42. No 1.

Haas R., Walls, J. and Carroll, R.G. 1988. Geogrid reinforcement of granular bases in flexible pavements. Transportation Research Record 1188, Washington DC, pp. 19-27.

Holtz, R.D, Christopher, B.R. and Berg, R.R. 1998. Geosynthetic design and construction guidelines. U.S. Department of Transportation, Federal Highway Administration, Washington, DC, FHWA-HI-98-038, 460 p.

Holtz, R. D., Christopher, B. R., & Berg, R. R. 2008. Geosynthetic Design & Construction Guidelines: Reference Manual. US Department of Transportation, Federal Highway Administration, National Highway Institute

Hugo, F., McCullough B.F., and Vander Walt B. 1991. Fullscale accelerated pavement testing for the Texas State Department of Highways and Public Transportation. Transportation Research Record 1293, Transportation Research Board, Washington, D.C., 1991, pp. 52-60.

Indraratna, B., Nimbalkar, S. 2013. The role of geosynthetics in improving the behavior of ballasted rail tracks. *Geosynthetics in Railway Track*, India. pp 59-85.

Kim, S., Yang, J., and Kwon, J. 2017. Effects of using screening materials in the graded aggregate base layer of flexible pavements, *International Journal of Pavement Engineering*. Vol., 18, Issue 2, 97-107

Kim, T. and Tutumluer, E. 2005. Unbound Aggregate Rutting Models for Stress Rotations and Effects of Moving Wheel Loads, *Transportation Research Record: Journal of the Transportation Research Board*. No 1913, 41-49.

Kwon, J., Boudreau, R.L., Tutumluer, E. and Wayne, M.H. 2014. Evaluation and Characterization of Aggregates for Sustainable Use in Pavement Engineering, *ASCE Geo-Congress*. 3373-3382.

Kwon, J., Kim, S, Tutumluer, E. and Wayne, M.H. 2017. Characterization of Unbound Aggregate Materials considering physical and morphological properties, *International Journal of Pavement Engineering*. 18:4, 303-308.

Lacina, B. A. 2011. Functions of Geotextiles Used in Roadway Base Course Construction: The benefits of using geotextiles in roadway construction include separation and stabilization. *AATCC Review: the magazine of the textile dyeing, printing, and finishing industry*, 11(5), 37.

Lipomi, D., Wayne, M.H. 2014. Geosynthetic Solutions for Paved and Unpaved Applications. *Shale Energy Engineering*, ASCE, pp 565-575

Little PH, 1993, The design of unsurfaced roads using geosynthetics, PhD thesis, Dept. of Civ. Eng., Univ. Nottingham.

Lu, M., McDowell, G.R., 2007. The importance of modelling ballast particle shape in the discrete element method. *Granular Matter* 9 (112), 69-80.

Luo, R., Gu, F., Luo, X., Lytton, R. L., Hajj, E. Y., Siddharthan, R. V., & Pournoman, S. 2017. Quantifying the Influence of Geosynthetics on Pavement Performance (No. NCHRP Project 01-50).

Mahaffay, B. Robinson, J. Gagnon, J., Norwook, G. 2019. Using geosynthetics in flexible airport pavements. IFAI Feature,

https://geosyntheticsmagazine.com/2019/06/01/using-geosynthetics-in-flexible-airport-pavements

McDowell, G.R., Harireche, O., Konietzky, H., Brown, S.F. and Thom. 2006. N.H. Discrete element modelling of geogrid-reinforced aggregates. In: *Proceedings of the Institution of Civil Engineers: Geotechnical Engineering*. 159/GE1, pp. 35–48.

Milligan, G.W.E., Love. J.P. 1985. Model Testing of Geogrids under an aggregate layer on soft ground. *Polymer Grid Reinforcement*, London, England. pp. 128-138.

Mishra, D. and Tutumluer, E. 2012. Aggregate Physical Properties Affecting Modulus and Deformation Characteristics of Unsurfaced Pavements, *Journal of Materials in Civil Engineering*. 24(9), 1144-1152.

Monismith. C.L. 1993. Permanent Deformation Characteristics of Subgrade Soils due to Repeated Loading. Committee on Strength and Deformation Characteristics of Pavement Sections.

Muench, S. 2006. http://pavementinteractive.org/ (Accessed July 02, 2019)

NCHRP. 2004. Project 1-37A, Guide for Mechanistic-Empirical Design of new and rehabilitated pavement structure. Washington, D.C.

Peralta, A. Identification of Optimum Aggregate Gradation for Transportation Applications of Multiaxial Geogrids. MS Thesis, 2016. Georgia Institute of Technology.

Perkins, S.W. 1999. Mechanical Response of Geosynthetic-Reinforced Flexible pavements. *Geosynthetics International*, Vol. 6, No. 5, pp. 347-382.

Perkins, S.W. and Ismeik, M. 1997a. A Synthesis and Evaluation of Geosynthetic-reinforced Base Course Layers in Flexible Pavements: Part I Experimental Work. *Geosynthetics International*, Vol. 4, No. 6, pp. 549-604.

Perkins, S. W., Bowders, J. J., Christopher, B. R., and Berg, R. R. 2005. Geo-synthetic reinforcement for pavement systems: US perspectives. In *International Perspectives on Soil Reinforcement Applications*. pp. 1-13.

Pidwerbesky, B. 1996. Fundamental Behavior of Unbound Granular Pavements Subjected to Various Loading Conditions and Accelerated Trafficking. PhD Thesis, University of Canterbury, NZ.

Qian, Y., Han, J., Pokharel, S. K., and Parsons, R. L. 2011a. Determination of resilient modulus of subgrade using cyclic plate loading tests. Proc., *GeoFrontiers 2011: Advances in Geotechnical Engineering*, Geotechnical Special Publication No. 211.

Qian, Y., Han, J., Pokharel, S. K., and Parsons, R. L. 2011b. Stress analysis on triangular aperture geogrid-reinforced bases over weak subgrade under cyclic loading-an experimental study. Proc., *10th Int. Conf. on Low-Volume Roads*, Transportation Research Board, Washington, DC, 83–91.

Qian, Y., Tutumluer, E., and Huang, H. 2011c. A validated discrete element modeling approach for studying geogrid-aggregate reinforcement mechanisms. Proc., *GeoFrontiers 2011: Advances in Geotechnical Engineering*, Geotechnical Special Publication No. 211.

Reck, N.C. 2009. Mechanistic empirical design of geogrid reinforced paved flexible pavements. *Jubilee symposium on Polymer Grid Reinforcement*, Institute of Civil Engineers, London, England. AASHTO Guidelines 1972

Robinson, W. J., Tingle, J. S., & Norwood, G. J. (2017). Full-Scale Accelerated Testing of Multi-axial Geogrid Stabilized Flexible Pavements (No. ERDC/GSL TR-17-9). ERDC-GSL Vicksburg United States

Roadex Network. Permanent Deformation Rutting Classification. *http://www.roadex.org/e-learning/lessons/permanent-deformation/permanent-deformation-rutting-classification/ (Accessed August 15, 2019)*

Smilauer, V. 2015. Yade Documentation 2nd ed. The Yade Project. DOI 10.5281/zenodo.34073 (http://yade-dem.org/doc/)

Sun, X., Han, J., Crippen, L. and Corey, R. 2017. Back-calculation of resilient modulus and prediction of permanent deformation for fine-grained subgrade under cyclic loading. *Journal of Materials and Civil Engineering*, 29(5): 04016284

Sun, X., Han, J. and Corey, R. 2017. Equivalent Modulus of Geogrid-stabilized granular base back-calculated using permanent deformation. Technical Note. *Journal of Geotech. & Geoenvironmental Engineering*, 143(9): 06017012

Tao, M., Louay, M.N., Munir, N.D., Zhang, Z. and Wu, Z. 2010. Application of Shakedown Theory in Characterizing Traditional and Recycled Pavement Base Materials, *Journal of Transportation Engineering*. 136 (3), 214–222.

Technical Specification, MRTS58 Subgrade Reinforcement using Pavement Geosynthetics, NZ Department of Transport and Main Roads

TenCate Geo 2018. Product Specification for Mirafi HP-270. https://www.tencategeo.us/en-us/products/woven-geotextiles/mirafi-hp. (Accessed July 11, 2018).

Tensar, 2010. Performance-Based Specifications for Roadways. Tensar International Corporation White Paper.

Tensar Biaxial BX Geogrid Product Specification. Tensar International Corporation. http://www.tensarcorp.com/Systems-and-Products/Tensar-Biaxial-BX-geogrids. (Accessed July 11, 2018)

Tensar, Geogrids for Roadway Applications, NDLTAP Roundtable Meeting – Killdeer ND – February 24, 2015

Thompson, M.R. 1998. State-of-the-art: unbound base performance. Proceedings of the *6th annual symposium of International Center for Aggregate Research (ICAR)*. Austin, TX.

Tingle, J.S., Webster, S.L. 2003. Design of Geosynthetic-Reinforced Unpaved Roads. Transportation Research Record Journal of the Transportation Research Board 1849:193-201 DOI: 10.3141/1849-21

Tingle, J.S., Norwood, G.J., Robindon, W.J., Wayne, M.H., Kwon, J. 2017. Full-scale accelerated pavement testing of geogrid stabilized roads. *Bearing Capacity of Roads, Railways and Airfields*. pp 2255-2261

Tseng, K.H. and Lytton, R.L. 1989. Prediction of Permanent Deformation in Flexible Pavement Materials, *ASTM STP*. 1016, 154-172.

Tutumluer, E. and Pan, T. 2008. Aggregate Morphology Affecting Strength and Permanent Deformation Behavior of Unbound Aggregate Materials, *Journal of Materials in Civil Engineering*. 20(9), 617-627.

Vennapusa, P. K., White, D. J., Wayne, M. H., Kwon, J., Galindo, A., & García, L. (2018). In situ performance verification of geogrid-stabilized aggregate layer: Route-39 El Carbón–Bonito Oriental, Honduras case study. International Journal of Pavement Engineering, 1-12

White, D. J., & Vennapusa, P. K. (2017). In situ resilient modulus for geogrid-stabilized aggregate layer: A case study using automated plate load testing. Transportation Geotechnics, 11, 120-132.

Webster, S.L. 1993. Geogrid Reinforced Base Course for Flexible Pavements for Light Aircraft: Test Section Consutruction, Behavior Under Traffic, Laboratory Tests, and Design Critieria. Technical Report GL-93-6. US Army Corps of Engineers

Xiao, Y., Tutumluer, E., Qian, Y. and Siekmeier, J.A. 2012. Gradation Effects Influencing Mechanical Properties of Aggregate Base-Granular Subbase Materials in Minnesota, *Transportation Research Record: Journal of the Transportation Research Board*. No 2267, 14-26.

Zornberg, J.G. 2011. Advances in the Use of Geosynthetic in Pavement Design, Proceedings of the *Second National Conference on Geosynthetics*, Geosynthetics India '11. Vol 1, 3-21.

Zornberg, J.G., Gupta R.. 2010. Geosynthetics in Pavements: North American Contributions. In *9th International Conference on Geosynthetics*, Brazil. Vol 1, pp. 379-400.